UNIVERSITY OF CALIFORNIA

Los Angeles

Control of Coupling Phenomena in Magnetic Nanostructures

A dissertation submitted in partial satisfaction of the

requirements for the degree Doctor of Philosophy

in Mechanical Engineering

by

Wei-Yang Sun

2015

ABSTRACT OF THE DISSERTATION

Control of Coupling Phenomena in Magnetic Nanostructures

by

Wei-Yang Sun

Doctor of Philosophy in Mechanical Engineering

University of California, Los Angeles, 2015

Professor Gregory P. Carman, Chair

The search for non-volatile, non-dissipative computing devices (memory and logic) beyond current transistor technology has encouraged the scientific community to develop new nanoscale magnetic control mechanisms. In the present work, the control of magnets by magnetoelastic anisotropy is investigated within the context of nanoscale magnetoelectric composite systems. These magnetoelectric composites are artificial multiferroic materials which exhibit both a coexistence and coupling of ferromagnetic and ferroelectric ordering. This device architecture provides a route to control magnetism with electric fields via the application of mechanical stress. In the present work, magnetization behavior under mechanical stress of various magnetically coupled systems is investigated using both advanced computer simulations and experimental work. The application of voltage-controlled strain is shown to influence dipole coupled nanomagnet arrays and antiferromagnetic-ferromagnetic (AFM-FM) spontaneous exchange bias systems, which present pathways to engineered systems. Furthermore, the

repeatable nature of these experiments presents unambiguous deterministic voltage control for both dipole-coupled systems and spontaneous exchange bias systems. The experimental results are confirmed by multiple characterization techniques, including superconducting quantum interference device magnetometry (SQUID) and magneto optic Kerr effect magnetometry (MOKE). This work thus provides significant evidence of the viability of magnetoelastic anisotropy as a means to control magnetoelectric heterostructures in future computing devices.

The dissertation of Wei-Yang Sun is approved.

Christopher Lynch

Kang L. Wang

Gregory P. Carman, Committee Chair

University of California, Los Angeles

2015

For my family and friends;

My accomplishments are yours.

Table of Contents

List of Figures

List of Tables

VITA

Education

2012	M.S. – Mechanical Engineering *University of California, Los Angeles*
2011	S.B. – Mechanical Engineering Massachusetts Institute of Technology

Employment History

2012-2015	Graduate Student Researcher UCLA Active Materials Laboratory (Carman)
2012-2014	Teaching Assistant, MATLAB UCLA Henry Samueli School of Engineering and Applied Science
2012-2014	Graduate/Undergraduate Tutor UCLA Tau Beta Pi
2011-2012	Teaching Assistant, Manufacturing Processes UCLA Mechanical and Aerospace Engineering
2011-2012	Graduate Student Researcher UCLA Micromanufacturing Laboratory (Kim)
2010-2011	Undergraduate Student Researcher MIT Nanoengineered Surfaces Group (Varanasi)
2009	Undergraduate Student Researcher MIT Micro Power and Nanoengineering Group (Livermore)
2008	Research and Software Assistant LumArray Inc.

Publications and conference presentations

Wei-Yang Sun, Laura T. Schelhas, Gregory P. Carman. "Strain-Mediated Magnetoelectric Control of Spontaneous Exchange Bias in Ni-NiO Thin Films." In review, April 2015 (ACS Nano Letters).

M. Salehi Fashami, M. Mamun Al-Rashid, **Wei-Yang Sun**, Paul K. Nordeen, Supriyo Bandyopadhyay, Gregory P. Carman, and Jayasimha Atulasimha. "Ultra low power binary information propagation in circular magnetic nanodot arrays using strain induced anisotropy." In preparation.

Wei-Yang Sun, Greg P. Carman. "Strain-Mediated Voltage Control of a Ni/NiO Spontaneous Exchange Bias (SEB) System." Intermag 2015, May 11 – 15 2015, Beijing, China.

Wei-Yang Sun, Paul K. Nordeen, M. Salehi Fashami, M. Mamun Al-Rashid, Supriyo Bandyopadhyay, Jayasimha Atulasimha, Gregory P. Carman. "Voltage Control of Magnetic Anisotropy in Dipole-Coupled Single Domain Nanomagnet Arrays." XXIII International Materials Research Congress, August 17 – 21, 2014, Cancun, Mexico.

Wei-Yang Sun, Paul K. Nordeen, M. Salehi Fashami, M. Mamun Al-Rashid, Supriyo Bandyopadhyay, Jayasimha Atulasimha, Gregory P. Carman. "Voltage Control of Magnetic Anisotropy in Dipole-Coupled Single Domain Nanomagnet Arrays." 2014 IEEE Magnetics Society Summer School, August 11 – 17, 2014, Rio de Janeiro, Brazil.

Kyle P. Wetzlar, **Wei-Yang Sun**, Chin-Jui Hsu, Gregory P. Carman. "Nanoscale Based Thermal Energy Harvesting" 3rd Multifunctional Materials for Defense Workshop, Aug 18-22, 2014, Arlington, VA.

Liang, Cheng-Yen, Scott M. Keller, Abdon E. Sepulveda, Alexandre Bur, **Wei-Yang Sun**, Kyle Wetzlar, and Gregory P. Carman. "Modeling of magnetoelastic nanostructures with a fully coupled mechanical-micromagnetic model." Nanotechnology 25, no. 43 (2014): 435701.

Liang, Cheng-Yen, Scott M. Keller, Abdon E. Sepulveda, **Wei-Yang Sun**, Jizhai Cui, Christopher S. Lynch, and Gregory P. Carman. "Electrical control of a single magnetoelastic domain structure on a clamped piezoelectric thin film—analysis." Journal of Applied Physics 116, no. 12 (2014): 123909.

Wei-Yang Sun, Paul Nordeen, and Gregory P. Carman. "Voltage Control and Moment Propagation of Superparamagnetic / Ferromagnetic Single Domain Nanomagnet Arrays." ASME 2013 Conference on Smart Materials, Adaptive Structures and Intelligent Systems, Sept 16 – 18 2013, Salt Lake City, Utah, USA.

Kyle P. Wetzlar, Chin-Jui Hsu, **Wei-Yang Sun**, Gregory P. Carman "Harnessing the Spin Reorientation for Thermomagnetic Energy Harvesting" 2013 UCLA Henry Samueli School of Engineering and Applied Science Tech Forum, May 8 2013, Los Angeles CA.

Wei-Yang Sun and Chang-Jin Kim. "The role of dissolved gas in longevity of Cassie states for immersed superhydrophobic surfaces." 2013 IEEE 26th International Conference on Micro Electro Mechanical Systems (MEMS), Jan 20 – 24 2013, Taipei, Taiwan.

Wei-Yang Sun. "Design and construction of rigs for studying surface condensation and creating anodized metal oxide surfaces." Department of Mechanical Engineering Bachelor thesis, Massachusetts Institute of Technology, 2011.

1. Introduction

Researchers have become increasingly aware of how magnetic properties change as conditions are altered (mechanical, electrical, thermal, etc.) in recent years. Coupling phenomena in magnetic materials are becoming critical for next-generation micro- and nanoscale electronic devices, as is evident by the growing interdisciplinary nature of the engineering research landscape. Exploiting this coupling can result in composite materials with unique and complex properties inaccessible through conventional intrinsic materials [1].

There are many recent efforts to understand and apply knowledge of small scale magnetic phenomena. Two main reasons exist for the great interest in nanoscale magnetic structures. Firstly, it is already widely known that nanoscale magnetic properties can depart remarkably from that of bulk; magnetic transition temperatures, remnant magnetization, and shape dependence all change remarkably when we consider tiny magnetic structures [1]. Secondly, the continued miniaturization of electronics, whether through increased computing performance requirements or economic market pressure, forces the community to face head-on the realities of nanoscale magnetic behavior [2].

This dissertation consists of an introduction chapter and 5 independent chapters, followed by a conclusion and a list of references. The first chapter introduces the phenomenology of magnetic materials and magnetoelectric systems, along with the motivation for pursuing nanoscale strain-mediated voltage control, all while referring extensively to existing literature. The second and third chapters explores the development and use of a new fully coupled mechanical/micromagnetic modeling paradigm to predict the behavior of magnetoelastic nanostructures. The fourth chapter explores the interaction between dipole-dipole coupling and

magnetoelasticity in nanomagnet arrays, and the electrical control of such coupling using strain-mediated multiferroic systems. The fifth chapter reports studies involving the modification of exchange bias using voltage-controlled applied strain, including the first study of such control of spontaneous exchange bias. Finally, the sixth chapter outlines the fabrication of testbeds for additional related magnetic coupling studies, real time nanomagnet measurement systems using anisotropic magnetoresistance (AMR); strain control of spin wave buses; observation of pure phonon-magnon interactions; and studies of perpendicular magnetic anisotropy for eventual strain-controlled 180-degree magnetization switching. The work in this dissertation will then be summarized in a concluding chapter before listing the cited references. Altogether, this document will outline how magnetoelastic composite systems can lead to both advanced understanding of nanoscale magnetic phenomena and novel engineered magnetic computing devices.

1.1 Magnetic Materials

It is first necessary to appreciate the history of humanity's understanding of magnetic materials, which has been a curiosity for many millennia. According to Chinese writings, magnetite (loadstone, Fe_3O_4) was first mentioned at around 4000 BC. Aristotle attributes the first of what could be called a scientific discussion on magnetism to Thales, who lived from about 625 to about 545 BC. In the 1st century AD, the Greek writer Pliny wrote that magnetite was discovered by the shepherd Magnes, "the nails of whose shoes and the tip of whose staff stuck fast in a magnetick field he pastured his flocks." Magnetite was mined in the province of Magnesia and the word magnet comes from the Greek "magnítis líthos," meaning "magnesian stone" [3].

Although magnetite can be polarized to generate a permanent magnetic dipole, it is actually classified as a ferrimagnet rather than a ferromagnet; the distinction will be described in the following paragraphs. .

Table 1.1 lists the six general classifications of magnetic behavior in different materials.

Table 1.1: Classifications of material magnetic behavior.

Classification	**Examples**	**Critical Temperature**	**Structure**
Diamagnetic	Most materials	-	No permanent dipole moment
Paramagnetic	Al, W, Mg	-	No permanent dipole moment

Ferromagnetic	Fe, Co, Ni	Curie T_C	Parallel dipole moments
Antiferromagnetic	NiO, CoO	Néel T_N	Antiparallel equal dipole moments
Ferrimagnetic	CrO_2, Fe_3O_4	Curie T_C	Antiparallel unequal dipole moments
Superparamagnetic	Nanoparticles	Blocking T_B	Parallel dipole moments below T_B

Magnetic material behavior is almost exclusively dependent on the materials' electron configurations, since electrons contribute both net spin magnetic moment and net magnetic angular momentum. Most materials have paired electrons in each atomic orbital; these are typically termed *diamagnetic* materials, or "nonmagnetic" materials – magnetic fields have the least influence on these. On the other hand, *paramagnetism* occurs in materials with unpaired electrons in their atomic orbitals – these spins align in the presence of an applied magnetic field, but return to chaotic alignment due to random thermal fluctuations when this applied magnetic field is removed [4].

Certain special materials have an additional, far stronger effect that arises from quantum exchange interactions, which are described in more detail in Section 5. . Due to quantum indistinguishability and exchange coupling in certain materials with unpaired electrons, an atom's spin state becomes determined by its adjacent atoms' spin states. The material is described as *ferromagnetic* when the magnetic spin states in a material are aligned in parallel, and *antiferromagnetic* when they are antiparallel. When spin states are antiparallel but unequal, the material is termed *ferrimagnetic*, and the net effect is very similar to that of ferromagnetic materials. Permanent magnets must be constructed from either ferromagnets or ferrimagnets. The

spin states of these main magnetic material classifications (paramagnetism, ferromagnetism, antiferromagnetism, and ferrimagnetism) are shown in Figure 1.1.

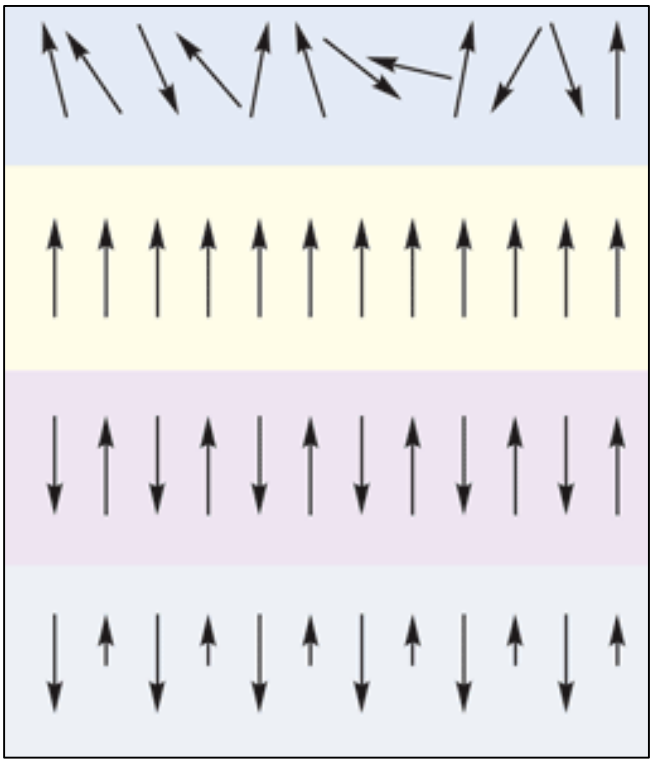

Figure 1.1: Diagram of classifications of magnetic materials (with effective spin states shown), in order vertically – paramagnetism, ferromagnetism, antiferromagnetism, and ferrimagnetism.

In bulk magnetic materials that exhibit exchange coupling, there exist *magnetic domains* of ordered material, which are independent of material grain boundaries. As shown in Figure 1.2, these domains, which are typically hundreds of nanometers in size, arise as energetically-favored configuration when compared to a perfectly ordered bulk. These magnetic domains are separated by domain walls, which are typically nanometers-thick. In a ferromagnetic material, for example, each domain contains atoms with spin states that are all pointing in the same direction. In a bulk magnetic material, each domain can be pointing in different directions, separated by domain walls containing spins that are in transition. When this material is magnetized by an applied

magnetic field, each domain's moment experiences a torque to align until saturation is reached at a sufficiently high field level.

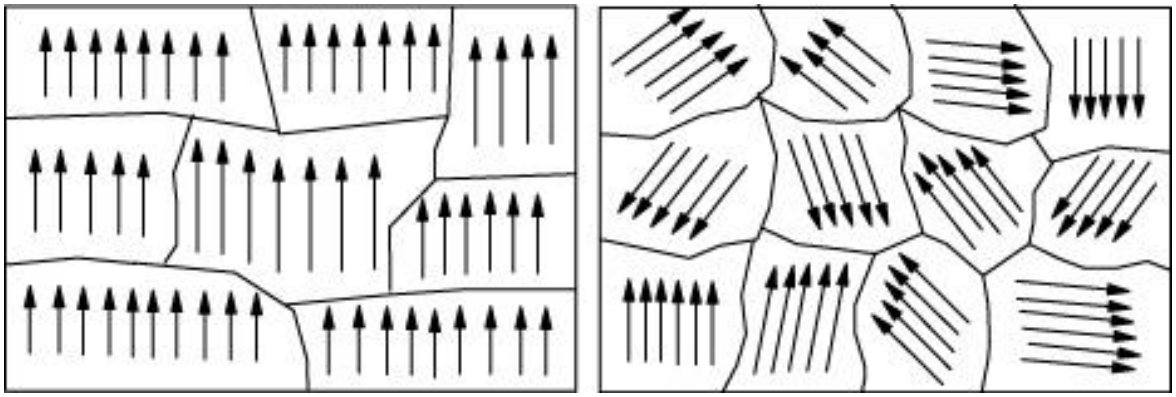

Figure 1.2: Highly magnetized domain state experiencing a high magnetic field applied vertically (left) and unmagnetized multi-domain state (right) of a bulk ferromagnet.

These magnetic materials have been instrumental in the development of technology throughout the industrial revolution, and the new information age. More recently, special attention has been given to micro- and nanoscale magnetic structures.

1.1.1 Phenomenology of Exchange Interactions

Both ferromagnetism (FM) and antiferromagnetism (AFM) arises from quantum mechanical exchange coupling of their atomic orbitals. To fully understand this coupling, one must turn to the quantum mechanical properties of the electrons that occupy these orbitals. One of the fundamental properties of an electron (besides that it carries charge) is that it has a magnetic dipole moment, i.e., it behaves itself as a tiny magnet. This dipole moment comes from the more fundamental property of the electron that it has quantum mechanical spin. The quantum mechanical nature of this spin causes the electron to only be able to be in two states, with the magnetic field either pointing "up" or "down" (for any choice of up and down). The spin of the electrons in atoms is the main source of ferromagnetism, although there is also a contribution from the orbital angular momentum of the electron about the nucleus. When these tiny magnetic dipoles are aligned in the same direction, their individual magnetic fields add together to create a measurable macroscopic field [5].

However, in materials with a filled electron shell, the total dipole moment of the electrons is zero because the spins are in up/down pairs. Only atoms with partially filled shells (i.e., unpaired spins) can have a net magnetic moment, so ferromagnetism only occurs in materials with partially filled shells. Because of Hund's rules, the first few electrons in a shell tend to have the same spin, thereby increasing the total dipole moment [3].

These unpaired dipoles (often called simply "spins" even though they also generally include angular momentum) tend to align in parallel to an external magnetic field, an effect called paramagnetism. Ferromagnetism involves an additional phenomenon, however: The

dipoles tend to align spontaneously, giving rise to a spontaneous magnetization, even when there is no applied field [4].

According to classical electromagnetism, two nearby magnetic dipoles will tend to align in opposite directions, so their magnetic fields will oppose one another and cancel out. However, this effect is very weak because the magnetic fields generated by individual spins are small and the resulting alignment is easily destroyed by thermal fluctuations. In a few materials, a much stronger interaction between spins arises because the change in the direction of the spin leads to a change in electrostatic repulsion between neighboring electrons, due to a particular quantum mechanical effect called the exchange interaction. At short distances, the exchange interaction is much stronger than the dipole-dipole magnetic interaction. As a result, in a few materials, the ferromagnetic ones, nearby spins tend to align in the same direction.

The exchange interaction is related to the Pauli exclusion principle, which says that two electrons with the same spin cannot also have the same "position". Therefore, under certain conditions, when the orbitals of the unpaired outer valence electrons from adjacent atoms overlap, the distributions of their electric charge in space are further apart when the electrons have parallel spins than when they have opposite spins. This reduces the electrostatic energy of the electrons when their spins are parallel compared to their energy when the spins are anti-parallel, so the parallel-spin state is more stable. In simple terms, the electrons, which repel one another, can move "further apart" by aligning their spins, so the spins of these electrons tend to line up. This difference in energy is called the exchange energy [4].

The materials in which the exchange interaction is much stronger than the competing dipole-dipole interaction are frequently called magnetic materials. For instance, in iron (Fe), the

exchange force is about 1000 times stronger than the dipole interaction. Therefore, below the Curie temperature virtually all of the dipoles in a ferromagnetic material will be aligned to their nearest neighboring ferromagnetic atoms. The exchange interaction is also responsible for the other types of spontaneous ordering of atomic magnetic moments occurring in magnetic solids – antiferromagnetism and ferrimagnetism. There are different exchange interaction mechanisms which create the magnetism in different ferromagnetic, ferrimagnetic, and antiferromagnetic materials, which include direct exchange, RKKY exchange, double exchange, and superexchange [4].

1.1.2 Anisotropy Through FM/AFM Interface Exchange

Certain unique phenomena can arise from the interface of antiferromagnetic and ferromagnetic materials, particularly for nanoscale thicknesses or geometries (on the order of the materials' exchange lengths). The essential physics underlying the phenomena is the previously explained exchange interaction between the antiferromagnet and ferromagnet at their interface.

Since antiferromagnets have a small or no net magnetization, their spin orientation is only weakly influenced by an externally applied magnetic field. A soft ferromagnetic film which is strongly exchange-coupled to the antiferromagnet will have its interfacial spins pinned. Reversal of the ferromagnet's moment will have an added energetic cost corresponding to the energy necessary to create a Néel domain wall within the antiferromagnetic film. The added energy term implies a shift in the switching field of the ferromagnet. Thus the magnetization curve of an exchange-biased ferromagnetic film looks like that of the normal ferromagnet except that is shifted away from the H=0 axis by an amount H_b.

In most well-studied ferromagnet/antiferromagnet bilayers, the Curie temperature of the ferromagnet is larger than the Néel temperature T_N of the antiferromagnet. This inequality means that the direction of the exchange bias can be set by cooling through T_N in the presence of an applied magnetic field. The moment of the magnetically ordered ferromagnet will apply an effective field to the antiferromagnet as it orders, breaking the symmetry and producing the exchange bias effect through influencing the formation of domains.

Exchange bias was first reported by Meiklejohn and Bean in 1957 in cobalt (Co) nanoparticles [6]. These particles, upon oxidation to form CoO shells surrounding a Co core, were found to have a significantly changed magnetic character – specifically, the M-H hysteresis

curve has shifted in the horizontal axis. This led Meiklejohn and Bean to theorize that the antiferromagnetic CoO was exerting a magnetic torque on the ferromagnetic Co's moment, causing a new type of exchange-based anisotropy. Depending upon the relative magnetic hardness of the ferromagnetic layer versus the antiferromagnetic layer, exchange bias can lead to either a coercivity enhancement or magnetic hysteresis loop shift, as illustrated in Figure 1.3.

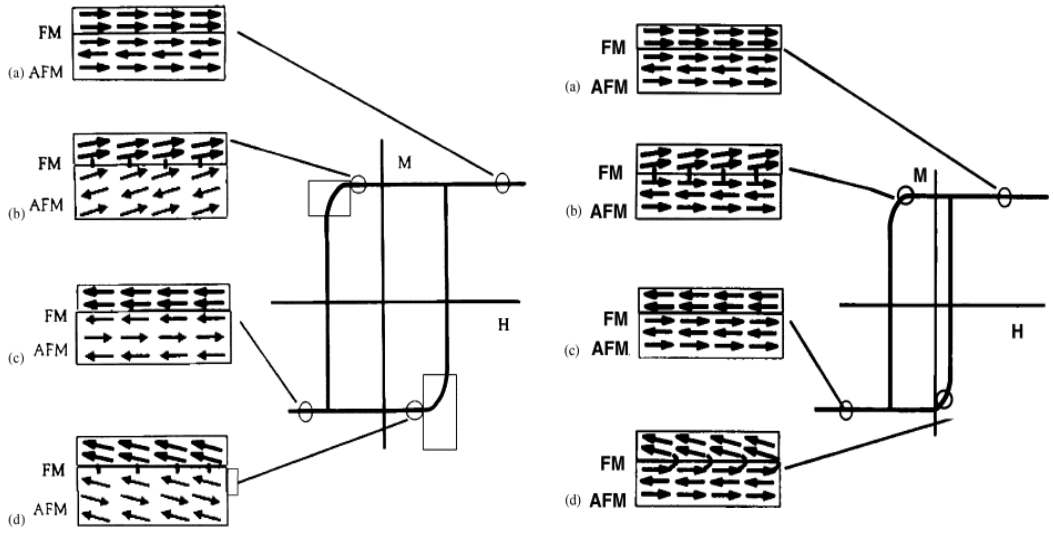

Figure 1.3: Diagrams illustrating coercivity enhancement (left) and loop shift (right) as a result of exchange bias. The insets show the corresponding diagrammatic spin states of the ferromagnetic (FM) and antiferromagnetic (AFM) materials near the interface.

To create an exchange bias system, typically the antiferromagnetic material is chosen to have a lower Néel temperature than the ferromagnetic material's Curie temperature, and the system must undergo a field cooling process, as illustrated in Figure 1.4. In this field cooling procedure, the ferromagnetic/antiferromagnetic system must be heated above the Néel temperature and cooled down in the presence of a strong applied magnetic field. This magnetic

field aligns the spins present in the ferromagnetic layer, and the antiferromagnetic spins immediately adjacent to the aligned spins are also induced to align via exchange coupling (outlined in blue).

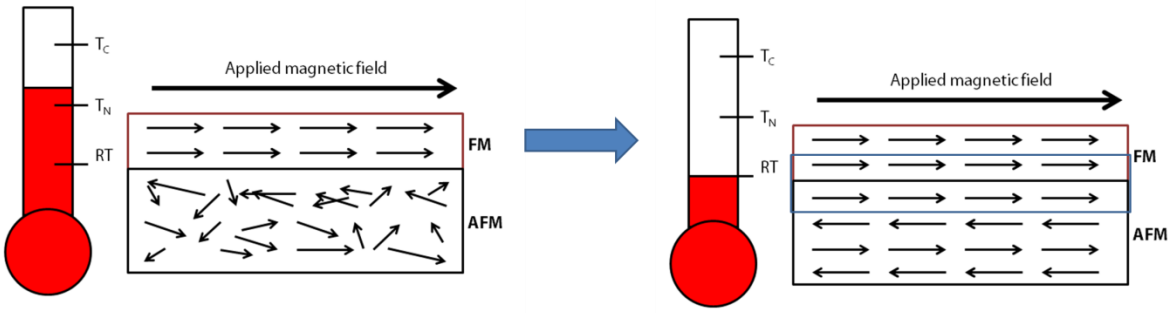

Figure 1.4: Schematic view of the field cooling process that produces an exchange bias system.

Many exciting developments, especially in recent years, have been put forth in the study of exchange bias. With regards to Meiklejohn's and Bean's initial discovery in Cu/CuO nanoparticles, these particles' behavior is now experimentally understood at all lengths scales between bulk and nanoscale [7]. Multiple physical exchange bias mechanisms have also been both theorized and identified, including the role of pinned interfacial spins and quantum exchange length [8][9][10]. Analytical and numerical models have attempted to quantify the exchange bias phenomenon, specifically in magnetic thin films, with a high degree of success [5][11][12]. It is important to note, however, that despite these great strides, the mechanisms for exchange bias is still not yet fully understood, and its study remains rich with discovery opportunities.

A popular upcoming application of exchange bias is in stabilizing the magnetization state of superparamagnetic particles, effectively shrinking the superparamagnetic limit, making possible smaller ferromagnetic single domain elements. This has important implications for the future of magnetic recording media, as the need grows for ever higher densities of magnetic memory storage [13].

In recent years, there have been efforts to deterministically control exchange bias phenomena. Wu et al. in 2010 demonstrated electrical control of exchange bias using a field-effect device with $BiFeO_3$ (ferroelectric/AFM) as the dielectric and ferromagnetic $La_{0.7}Sr_{0.3}MnO_3$ as the conducting channel, demonstrating controlled direct flipping of AFM spins in the single phase multiferroic $BiFeO_3$ [14]. Liu et al. in 2011 showed that the strength of the exchange bias (horizontal loop shift) can be modified through electrically controlling the applied strain [15]. More recently, Wu et al. in 2013 improved upon the 2010 work and reported bipolar electrical control of initiated CEB through direct flipping of the AFM spins in $BiFeO_3$. This later work demonstrated exchange bias reversibly switches between two 180-degree antiparallel stable states [16].

1.2 Magnetoelectricity

The magnetoelectric effect was first discovered by P. Curie in 1894 while the term "magnetoelectric" was coined by P. Debye in 1926. A more rigorous prediction of a linear coupling between electric polarization and magnetization was shortly formulated by L.D. Landau and E. Lifshitz in one book of their famous series on theoretical physics. Only in 1959, I. Dzyaloshinskii, using an elegant symmetry argument, derived the form of a linear magnetoelectric coupling in Cr_2O_3. The experimental confirmation came just a few months later when the effect was observed for the first time by D. Astrov. Between the prediction of I. Dzialoshinskii and the MEIPIC first edition (1973), more than 80 linear magnetoelectric compounds were found. Recently, technological and theoretical progress triggered a renaissance of these studies, and the magnetoelectric effect is still heavily investigated today [17].

Magnetoelectricity is critical for controlling magnetism at the micro- and nanoscales. The conventional method for controlling magnetism is with current loops with or without a ferromagnetic core (solenoids and electromagnets, respectively). This has been known since Danish scientist Hans Christian Oersted discovered in 1820 that electric currents create magnetic fields, and British scientist William Sturgeon invented the electromagnet in 1824. However, as these systems are created with vanishingly small wire diameters, significant obstacles in present themselves in the form of high resistances, heat production, and loss of efficiency. Systems using the magnetoelectric effect represent an attractive alternative; these current-based obstacles can often entirely circumvented.

For most magnetoelectric materials, the coupling coefficient between the electric and magnetic regimes is weak. To produce a stronger magnetoelectric effect, one can use composites

of multiple materials to achieve much higher magnetization changes. A popular strategy for engineering magnetoelectric effects is to introduce indirect coupling, such as through strain between a magnetoelastic ferromagnet and a ferroelectric material that exhibits high strain when undergoing polarization [18]. The materials comprising these strain-mediated multiferroic components will be reviewed in the following sections.

1.2.1 Magnetoelasticity

Magnetism occurs when atoms with unpaired spin orbitals are bound to a crystal lattice. Asymmetry in the spin-orbit coupling interacting with the local crystalline electric field results in magnetic anisotropy such as magnetocrystalline anisotropy. Certain directions within the material magnetize easier than others, and this preference is strongly correlated to the crystal lattice. From this viewpoint, a modification of the crystal lattice by mechanical stress necessitates a change in the magnetic easy axis. The magneto-mechanical coupling described in this manner is called *magnetoelasticity* or the *inverse Villari effect*. Described as energy, the directional variance in magnetic properties in response to a mechanical stress is called *magnetoelastic anisotropy* [4]. It should be noted that only a handful of magnetic materials express magnetoelasticity in useful magnitudes. This is because the magnitude of expressed magnetoelasticity is related to the asymmetry of the spin-orbit coupling and the relative strength of other magnetic anisotropies, such as magnetocrystalline anisotropy, which may lock the magnetization and hinder magnetoelastic coupling.

Describing or modeling the magnetoelastic response can be challenging, given the diversity of magnetic materials and the complexity of the spin-orbit-crystal lattice interactions. Furthermore, as was discussed earlier, at the macroscale magnetic materials are composed of many millions of magnetic domains, or regions of uniform magnetization – this further exacerbates the modeling complexity. Fortunately for magnetic researchers, relatively simple models have been developed to describe the cumulative behavior of these multi-domain materials under mechanical load.

The following multi-domain model predicts the average magnetization behavior of multiple domains under magnetoelastic anisotropy. This is useful for describing the general

magnetization preference of bulk or multidomain (MD) systems. More interestingly, the "rules of thumb" guiding magnetoelasticity which are illustrated here will make more complex systems easier to predict and visualize.

Let's consider a representative MD model of a negative magnetostrictive material (such as nickel) consisting of four domains arranged in head-to-tail flux closure, as shown in Figure 1.5. The magnetization behavior (magnetization (M) vs. applied field (H) response) of this MD system may appear similar to Figure 1.5A, with an initially high permeability which decreases toward saturation. If we then apply a compressive stress, the model takes on the form of Figure 1.5B. Now the M-H behavior may appear like Figure 1.5B, with a higher initial permeability in response to the applied mechanical load. Magnetoelastic anisotropy is added to the system, leading to increased magnetization tendency parallel to the applied strain. In this instance, magnetization is completed with less applied field than in the initial case, this is termed an *easy axis*. In this example, the material is called negatively magnetostrictive because a compressive (negative-sign) load causes magnetization increase along the applied direction. We observe the opposite effect in Figure 1.5C where a tensile stress is applied to the same negative magnetostrictive material. This time the M-H behavior shows a gradual magnetization response with initially lower permeability. This response is called hard because of the larger field required for magnetization. This simple interpretation of the magneto-mechanical interaction is useful for predicting average magnetization preference over large samples and can even provide a rough estimation of spin preference in nanostructures.

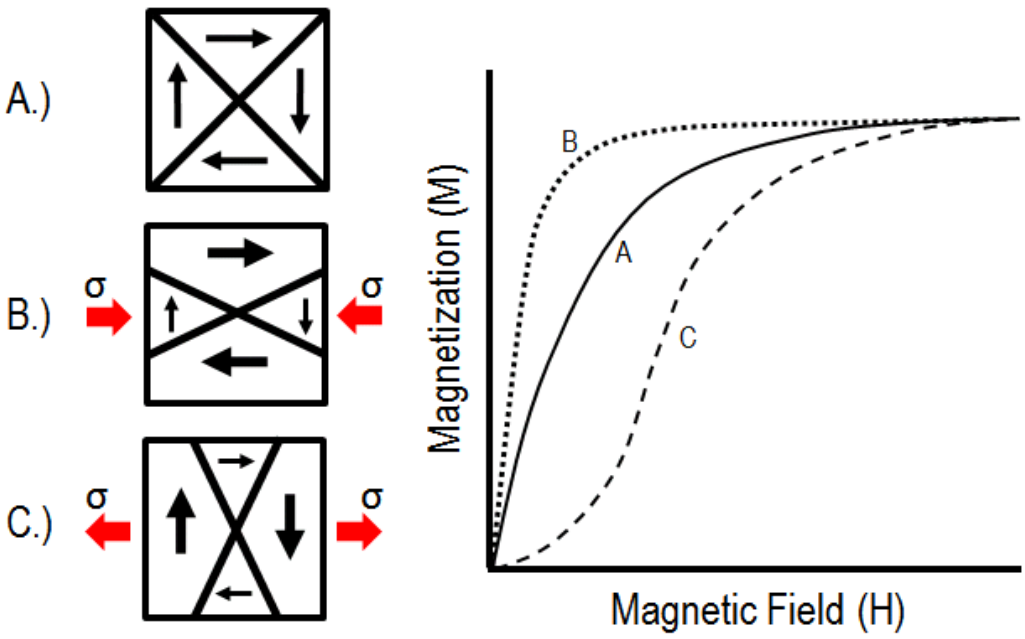

Figure 1.5: Magnetization behavior of a negative magnetostrictive material as a function of applied mechanical stress, σ. At left are the loading schemes and at right are the corresponding magnetization trends (M-H curves). A. No applied load. B. Applied compressive stress resulting in increased magnetization preference (easy). C. Applied tensile stress resulting in reduced magnetization preference (hard).

Just as magnetization can be manipulated by magnetoelastic anisotropy, so can magnetostriction behavior, denoted as λ. As stated earlier, magnetization and magnetostriction response are directly related, though the magnitude and sign of the lattice strain upon magnetization depends on the material. When a magnetic field is applied to a magnetic material, the magnetization will rotate to minimize the Zeeman potential. Interestingly, the crystal lattice of the material sometimes deforms from its normal state in an effort to minimize this Zeeman potential, an effect we observe as magnetostriction. We study magnetostriction ability because it provides information about the magneto-mechanical coupling efficiency. One measure of this coupling efficiency is the piezomagnetic coefficient, dλ/dH but also expressed in the inverse case

as dB/dε. In coupled magnetoelastic systems where the goal is to maximize magnetic or mechanical output a large piezomagnetic coefficient is desired. Since a material's ability to respond to strain or magnetic field is critical to the piezomagnetic coefficient, we must look closer at the origin of magnetostriction and how it can be maximized by magnetoelastic anisotropy.

Let us imagine that magnetic materials are made of elliptical magnetic domains, displayed in Figure 1.6 as ellipses with their magnetizations lying parallel to the long axis. A real magnetic material may be made up of millions of such domains, thus the total field-induced length change (i.e. magnetostriction) of the magnetic material is a function of domain rotation and alignment. A completely reversing 180 degree domain structure does not change the total length of the macro material because the total length of domains has not changed. If we then apply a stress, the domains may rotate 90 degrees in response to the magnetoelastic anisotropy and the total length of the domains is decreased. Now when a field is applied, the domains rotate 90 degrees to align with the field and the total length of the material increases significantly. These non-180 degree domain rotations increase the magnetostriction response of the material and are made possible by the magnetoelastic anisotropy. This magnetoelastic anisotropy-dependent magnetostriction behavior is important for strain-coupled magnetic systems such as the ME-RAM mentioned earlier. For these applications, Terfenol-D is a magnetostrictive material of significant research interest in recent years, especially in the context of strain-mediated multiferroic systems, due to its exceptionally high magnetoelastic properties [19]. Later, it will be shown that the transduction ability of a magnetoelectric laminate can be improved by magnetoelastic anisotropy and this is due to the non-180 degree domain rotations and improved strain response described here.

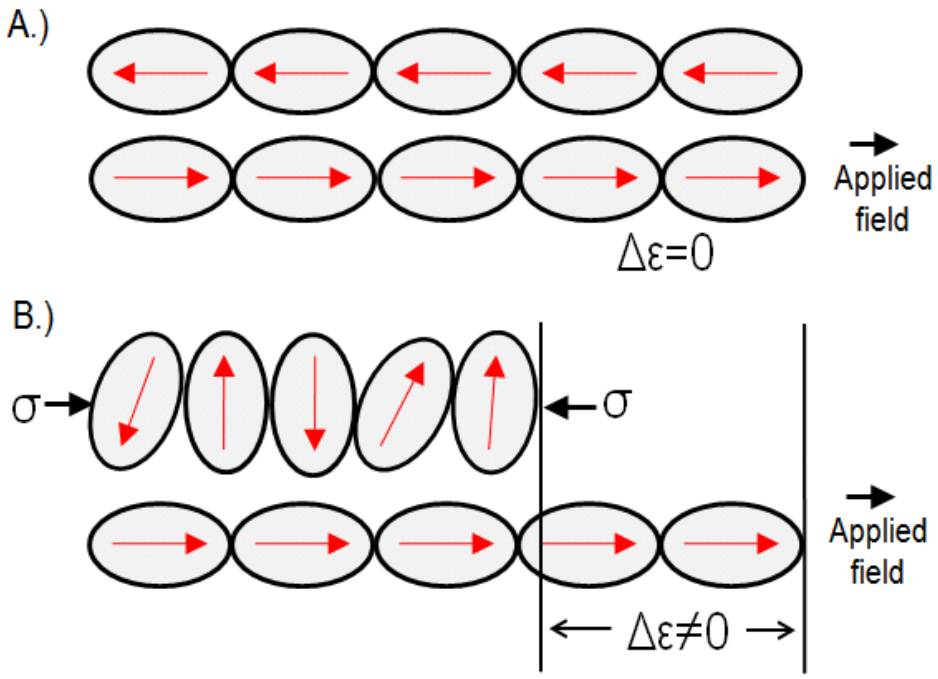

Figure 1.6: Magnetostriction behavior of a magnetostrictive material under applied compressive mechanical stress. A. 180 domain rotation results in zero net magnetostrictive strain. B. Applied load increases prevalence of non-180 degree domain rotation. When magnetic field is applied the net magnetostriction is non-zero.

1.2.2 Ferroelectricity

A *ferroelectric material* exhibits a nonzero and nonlinear reversible polarization as a response to an externally-applied electric field. This is analogous to ferromagnetic materials, which exhibit magnetization when in a magnetic field. Ferromagnetism was already known when ferroelectricity was discovered in 1920 in Rochelle salts by Valasek [20]. Thus, the prefix *ferro*, meaning iron, was used to describe the property, despite the fact that most ferroelectric materials do not contain iron.

The internal electric dipoles of a ferroelectric material are coupled to the material lattice; anything that changes the lattice will change the strength of the dipoles (in other words, a change in the spontaneous polarization). The change in the spontaneous polarization results in a change in the surface charge. This can cause current flow in the case of a ferroelectric capacitor even without the presence of an external voltage across the capacitor. Two stimuli that will change the lattice dimensions of a material are force and temperature. The generation of a surface charge in response to the application of an external stress to a material is called piezoelectricity. A change in the spontaneous polarization of a material in response to a change in temperature is called pyroelectricity [21].

Ferroelectric phase transitions are often characterized as either displacive (such as BaTiO3) or order-disorder (such as NaNO2), though often phase transitions will demonstrate elements of both behaviors. In barium titanate, a typical ferroelectric of the displacive type, the transition can be understood in terms of a polarization catastrophe, in which, if an ion is displaced from equilibrium slightly, the force from the local electric fields due to the ions in the crystal increases faster than the elastic-restoring forces. This leads to an asymmetrical shift in the

equilibrium ion positions and hence to a permanent dipole moment. The ionic displacement in barium titanate ($BaTiO_3$) concerns the relative position of the titanium ion within the oxygen octahedral cage. In lead titanate ($PbTiO_3$), another key ferroelectric material, although the structure is rather similar to barium titanate, the driving force for ferroelectricity is more complex with interactions between the lead and oxygen ions also playing an important role. In an order-disorder ferroelectric, there is a dipole moment in each unit cell, but at high temperatures they are pointing in random directions. Upon lowering the temperature and going through the phase transition, the dipoles order, all pointing in the same direction within a domain [21].

An important ferroelectric material for applications is lead zirconate titanate (PZT), which is part of the solid solution formed between ferroelectric lead titanate and anti-ferroelectric lead zirconate. Different compositions are used for different applications; for memory applications, PZT closer in composition to lead titanate is preferred, whereas piezoelectric applications make use of the diverging piezoelectric coefficients associated with the morphotropic phase boundary that is found close to the 50/50 composition [21].

Ferroelectric crystals often show several transition temperatures and domain structure hysteresis, much as do ferromagnetic crystals. The nature of the phase transition in some ferroelectric crystals is still not well understood.

Generally, there are 230 space groups among which 32 crystalline classes can be found in crystals. There are 21 non-centrosymmetric classes, within which 20 are piezoelectric. Among the piezoelectric classes, 10 have a spontaneous electric polarization that varies with the temperature, therefore they are pyroelectric. Among pyroelectric materials, some of them are ferroelectric. Examples of ferroelectric materials include the aforementioned Rochelle salts,

along with BaTiO3 and perovskite crystals. Certain ferroelectric materials exhibit giant strains, quantified via the piezoelectric coefficient *d*, related to polarization and stress as:

$$d = \frac{P}{\sigma}$$

A very popular ferroelectric material is Pb(Mg1/3Nb2/3)O3](1-x)-[PbTiO3]x , which is often simply referred to in the literature as PMN-PT. A PMN-PT crystal aligned to its 011-direction (depicted in Figure 1.7) can exhibit uniaxial strain changes as high as ~1700 microstrain [22]. This is the predominant material used in the proposed work for applying strain to magnetic nanostructures.

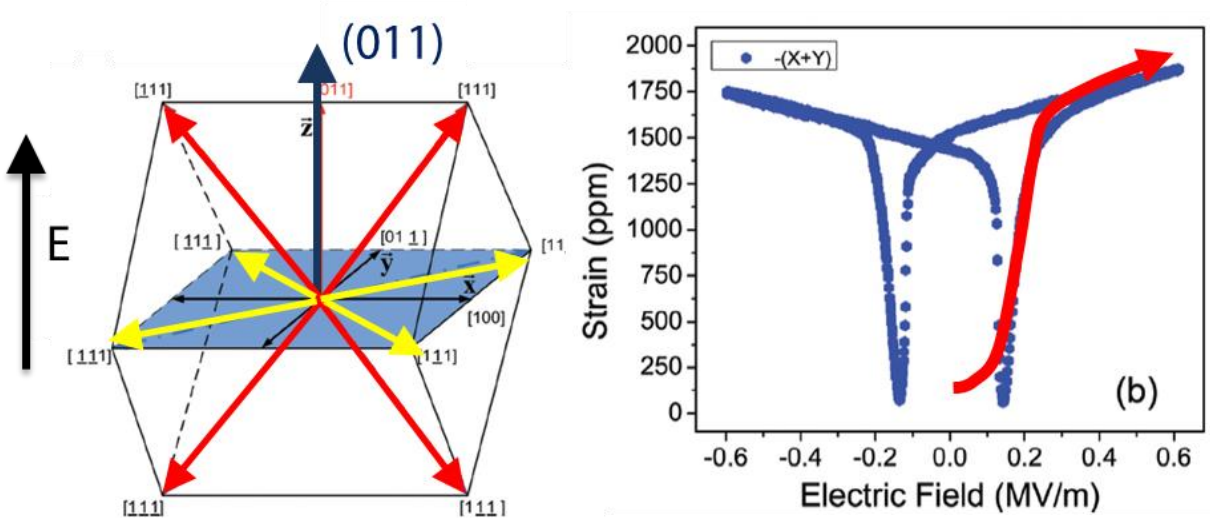

Figure 1.7: Schematic view of PMN-PT's crystallographic axes under the influence of an applied electric field (left), and a plot of resultant strain as a function of field strength (right).

1.2.3 Strain-Mediated Magnetoelectric Composites

The first strain-mediated magnetoelectric system was realized on the macroscale through physically-coupled bulk ferroelectric and magnetoelastic materials, in 2001 by Ryu et al. [23]. Since then, the field of strain-mediated multiferroics has flourished, and UCLA has been at the forefront of this research, along with researchers at Cornell, UC Berkeley, Stanford, and others [24].

UCLA has been very actively growing the area of strain-mediated magnetoelectric research, including both laying groundwork in characterizing PMN-PT, an important ferroelectric for engineered strain systems [22], and actual implementation of multiferroic systems with the intent of potential memory devices [25]. Notable additions to the literature include demonstration of magnetization rotation in patterned nickel (Ni) ring structures [26] and strain-mediated voltage control of domain wall configuration in Ni thin film [27].

Strain-mediated multiferroics is becoming increasingly implemented at the nanoscale. VCU and Notre Dame are at the forefront of modeling magnetic switching of ferromagnetic single domain structures using multiferroics [28][29][30]. The UCLA Active Materials Laboratory has recently demonstrated voltage-controlled switching between superparamagnetic and ferromagnetic single domain (SP/FSD) states in nickel nanospheres strain-coupled to a ferroelectric substrate [31].

2. Fully Coupled Mechanical/Micromagnetic Modeling

Micromagnetic simulations of magnetoelastic nanostructures traditionally rely on either the Stoner-Wohlfarth model or the LLG model assuming uniform strain (and/or assuming uniform magnetization). While the uniform strain assumption is reasonable when modeling magnetoelastic thin films, this constant strain approach becomes increasingly inaccurate for smaller in-plane nanoscale structures. This work presents analytical work to significantly improve simulation of finite structures by fully coupling LLG with elastodynamics, i.e. the partial differential equations are intrinsically coupled. The coupled equations developed in this manuscript along with Stoner-Wohlfarth model and LLG (constant strain) are compared to experimental data on nickel Ni nanostructures. Results reveal that this work's fully-coupled approach is significantly superior regarding agreement with experimental data. This more sophisticated modeling technique is critical for guiding the design process of future nanoscale strain-mediated multiferroic elements such as those needed in memory systems.

2.1 Introduction and Background

Electrical control of ferromagnetic elements represents an important and emerging area of study in multiferroics. Magnetic control has conventionally been accomplished using an applied magnetic field rather than an electric field. Recently a number of relatively newer methods for controlling magnetization have been studied including carrier-mediated ferromagnets [32][33], exchange coupled multiferroic interfaces [34][35], and spin-transfer torque effects [36]–[38]. While these areas represent important topics, electrically induced strain-mediated control of magnetic properties may represent a more promising approach in the near term. This statement is based on the relative maturity of both piezoelectric and magnetostrictive materials required for the strain mediated multiferroics approach, i.e. new materials are unnecessary. One application for strain-mediated multiferroics is in magnetic random access memory (MRAM) where substantial reduction in write energies are possible [39][40]. However, a robust modeling approach that accurately predicts the nanoscale structures magnetic response is presently unavailable.

The strain-mediated multiferroic approach consists of mechanically coupling magnetoelastic elements onto ferroelectric substrates [18], [41]–[43], e.g. sputter deposition of composite heterostructures. In these composites, an electric field applied to the ferroelectric/piezoelectric substrate induces an anisotropic strain in the magnetoelastic material. The anisotropic stain induces a magnetic anisotropy via the converse magnetoelastic effect [44]. There exist fairly extensive studies containing both theoretical and experimental work on strain-mediated magnetization changes, coercivity changes [45], and strain-induced anisotropy in continuous magnetic thin films [46]. In all of the continuous film studies the strain is

appropriately assumed to be fully-transferred from the ferroelectric to ferromagnetic layer by treating the magnetoelastic energy as a pure uniaxial anisotropy applied to the magnetic media. For example, T. Brintlinger et al. reported both experimental and analytical predictions using OOMMF and constant strain assumptions to show reversible switching in FeGa/BTO thin film [47]. In recent years several additional studies, such as ferroelectric/ferromagnetic film coupling by Lahtinen et al. [48] and magnetic thin film stress modeling by Bai et al. [49], has demonstrated that this constant strain methodology works reasonably well for continuous thin films [50].

A relatively less studied area is on the strain-mediated effect in multiferroic nanostructures [51]. For example, Bur et al. [52] reported strain-induced coercive field changes in patterned single-domain nickel nanostructures deposited on Si/SiO_2 substrate. Bur's study showed that the coercive field is a direct function of applied strain due to the magnetoelastic effect. In this work, experimental data was compared to micromagnetic simulations with uniform and non-uniform strain conditions. However, the strain states were calculated before performing the micromagnetic simulation, thus the governing equations were not fully coupled. A few studies also exist on uniform strain transfer and strain-induced change of magnetization in nanostructures [28][29][51]; however, as the thickness of the nanostructures increases or in-plane dimensions decrease, the validity of the fully-transferred strain assumption becomes increasingly compromised [53]. Therefore, more sophisticated modeling is required.

Recently, researchers have begun to investigate more sophisticated modeling techniques for coupling LLG with elastodynamics. These approaches include mathematical and numerical methods for the solutions of coupled micromagnetic and elastodynamic equations. The

mathematical approach includes showing the existence and convergence of the coupled solutions such as presented by Banas et al. [54] and Alouges et al. [55]. Numerical approaches have also been presented by Y.C.Shu et al. [56] using a numerical framework to explore stress effects on magnetoelastic thin film behavior. More recently, Zhang and Chen [57] used a phase-field method to combine micromagnetic and elastodynamic equations for predicting magnetic domain structures and their temporal evolution in magnetoelastic materials. Micromagnetic coupled models have also been previously used to analyze the magnetic domain switching behavior in ferromagnetic/ferroelectric heterostructures when an electric field is applied to the ferroelectric layer [51][57][58][59]. While a few sophisticated solutions have been presented, these presentations do not compare their data directly with experimental results and thus leaves the modeling approaches questionable.

In this study, we develop a numerical method based on finite elements to fully-couple micromagnetic simulations with elastodynamics in finite size 3D structures. The analytical results are compared to both conventional analytical methods and experimental results. The new coupled model provides an approach to simultaneously solve the full strain and micromagnetic spin distribution in the finite composite system as a function of position and time. In this study the strain-induced coercive changes in a nickel nanostructure elastically coupled to a Si/SiO_2 substrate is investigated. Displacements are applied to the substrate producing strain and magnetic spin variations in the nickel nanostructure. Magnetic hysteresis curves at constant strain are predicted and compared to the Stoner–Wohlfarth (SW) [60] and the LLG model assuming uniform strain. Comparing these analytical results with the experimental data by Bur et al. [52] revealed that the strain distribution significantly influences the magnetic hysteresis curves and the coercive fields. We demonstrate that the new coupled model results are in

significantly better agreement with the experimental data when contrasted with the Stoner Wohlfarth or LLG model assuming uniform strain.

2.2 Theory

In this section, we derive the theoretical magnetoelastic framework for a problem between micromagnetics and elastodynamics. The methodology, in differential form, reduces to seven coupled PDEs, which in turn are formulated in their weak form. Assumptions include small elastic deformations, linear elasticity, magnetostatics, and negligible electrical current contributions. In this work we have not included the piezoelectric relations which would be trivial to add into the formulations; the test data used by by Bur et al. [52] relied on mechanical loading rather than electric field loading.

The equilibrium for magnetic systems is characterized by local minima of the total free energy density E_{tot}, written as [57][61]

$$E_{tot} = E_{ext} + E_{ex} + E_{anis} + E_d + E_{el} \tag{1}$$

which consists of the external energy density E_{ext} in an applied external field, the exchange energy density E_{ex}, the magnetocrystalline anisotropy energy density E_{anis}, the demagnetization energy density E_d, and the elastic energy density E_{el}.

The E_{ext} is produced by the applied magnetic field $\underline{H}_{ext}$ and is expressed as

$$E_{ext} = -\mu_0 M_s \left(\underline{m} \cdot \underline{H}_{ext} \right) \tag{2}$$

where $\underline{m}$ is the magnetization normalized by the saturation magnetization M_s, and μ_0 is the permeability of free space. E_{ex} is defined by the magnetization gradient and the exchange stiffness constant A_{ex} as [61]

$$E_{ex} = A_{ex}\left(\nabla \underline{m}\right)^2 \tag{3}$$

The anisotropy energy density E_{anis} for a cubic crystal is defined as [57][61]

$$E_{anis} = K_1\left(m_1^2 m_2^2 + m_2^2 m_3^2 + m_3^2 m_1^2\right) + K_2\left(m_1^2 m_2^2 m_3^2\right) \tag{4}$$

where K_1 and K_2 are cubic anisotropy constants. Equation (4) need to be modified to account for hexagonal or uniaxial crystals [4]. The demagnetization energy density E_d is given by

$$E_d = -\frac{1}{2}\mu_0\left(M_s \underline{m} \cdot \underline{H}_d\right) \tag{5}$$

where $\underline{H}_d$ is the demagnetization field. $\underline{H}_d$ is determined from Ampere's law ($\nabla \times \underline{H}_d = 0$), Gauss's law ($\nabla \cdot \underline{B} = 0$), and the relation between the magnetic induction $\underline{B}$ and magnetization $\underline{m}$ as [62]

$$\underline{B} = \underline{H}_d + M_s \underline{m} \tag{6}$$

$\underline{H}_d$ is related to the gradient of a magnetic potential ϕ by using Ampere's law,

$$\underline{H}_d = -\nabla\phi \tag{7}$$

The elastic energy density term (E_{el}) in Equation(1) can be written as

$$E_{el} = \frac{1}{2}\underline{\underline{\varepsilon}}^{el} : \underline{\underline{\underline{C}}} : (\underline{\underline{\varepsilon}}^{el}) \tag{8}$$

where $\underline{\underline{\underline{C}}}$ is the elastic stiffness tensor and $\underline{\underline{\varepsilon}}^{el}$ is the elastic strain tensor of the material.

In magnetostrictive materials, magnetic moments and displacements are coupled. Therefore, the total strain $\underline{\underline{\varepsilon}}$ in a ferromagnetic material is composed of magnetic ($\underline{\underline{\varepsilon}}^{m}\left(\underline{m}\right)$) and elastic ($\underline{\underline{\varepsilon}}^{el}$) contributions as [54][56][57]

$$\underline{\underline{\varepsilon}} = \underline{\underline{\varepsilon}}^{m}\left(\underline{m}\right) + \underline{\underline{\varepsilon}}^{el} \tag{9}$$

where $\underline{\underline{\varepsilon}}^{m} = \underline{\underline{\underline{\lambda}}}^{m}\,\underline{m}\underline{m}^{T}$ is the strain associated with local magnetization changes and $\underline{\underline{\underline{\lambda}}}^{m}$ is the magneto-mechanical coupling tensor. In the case of a cubic crystal, $\underline{\underline{\varepsilon}}^{m}$ is given by [57][4]

$$\varepsilon_{ij}^{m} = \begin{cases} \dfrac{3}{2}\lambda_{100}\left(m_i m_j - \dfrac{1}{3}\right) & i = j \\ \dfrac{3}{2}\lambda_{111} m_i m_j & i \neq j \end{cases} \tag{10}$$

where λ_{100} and λ_{111} are magnetostriction constants along $\langle 100 \rangle$ and $\langle 111 \rangle$ directions. For hexagonal or uniaxial crystals, equation (10) would need to be modified.

The total strain $\underline{\underline{\varepsilon}}$ is related to the displacement $\underline{u}$ by

$$\underline{\underline{\varepsilon}} = \frac{1}{2}\left(\nabla \underline{u} + \left(\nabla \underline{u}\right)^{T}\right) \tag{11}$$

and the stress tensor $\underline{\underline{\sigma}}$ is related to the strains as

$$\underline{\underline{\sigma}} = \underline{\underline{\underline{C}}}\,\underline{\underline{\varepsilon}}^{el} = \underline{\underline{\underline{C}}}\left[\underline{\underline{\varepsilon}} - \underline{\underline{\varepsilon}}^{m}\left(\underline{m}\right)\right] \tag{12}$$

where the stress distribution is governed by the elastodynamic equation

$$\rho \frac{\partial^2 \underline{u}}{\partial t^2} - \nabla \cdot \underline{\underline{\sigma}} = \underline{0}$$

(13)

and ρ is the mass density.

The effective magnetic field $\underline{H}_{eff}$ is obtained by differentiating the total energy density (equation1) with respect to magnetization

$$\underline{H}_{eff} = -\frac{1}{\mu_0 M_S} \frac{\partial E_{tot}}{\partial \underline{m}} = \underline{H}_{ext} + \underline{H}_{ex} + \underline{H}_{anis} + \underline{H}_{d} + \underline{H}_{me}\left(\underline{m}, \underline{u}\right) \qquad (14)$$

where $\underline{H}_{d}$ is defined in Equation (7), $\underline{H}_{ext}$ is the applied external field, and [54][56][57][61]

$$\underline{H}_{ex} = \frac{2A_{ex}}{\mu_0 M_s} \Delta \underline{m}$$

$$H^{i}_{anis} = -\frac{2m_i}{\mu_0 M_S}\left[K_1\left(m_j^2 + m_k^2\right) + K_2\left(m_j^2 m_k^2\right)\right] \qquad (15)$$

$$\underline{H}_{me} = -\frac{1}{\mu_0 M_S} \underline{\underline{\underline{C}}}\left(\underline{\underline{\varepsilon}} - \underline{\underline{\varepsilon}}^{m}\left(\underline{m}\right)\right) \cdot \frac{\partial \underline{\underline{\varepsilon}}^{m}\left(\underline{m}\right)}{\partial \underline{m}}$$

The effective field $\underline{H}_{eff}$ term is used in the phenomenological Landau-Lifshitz-Gilbert (LLG) micromagnetic relation

$$\frac{\partial \underline{m}}{\partial t} = -\mu_0 \gamma\left(\underline{m} \times \underline{H}_{eff}\right) + \alpha\left(\underline{m} \times \frac{\partial \underline{m}}{\partial t}\right) \qquad \textbf{(16)}$$

where γ is the Gilbert gyromagnetic ratio and α is the Gilbert damping constant.

Equations (1) - (16) represent a system of equations describing the magnetoelastic response of a coupled micromagnetic-mechanical system. This set of equations can be reduced further; using Gauss's law ($\nabla \cdot \underline{B} = 0$) and Equations (6) and (7), the magnetic potential ϕ satisfies the Poisson equation

$$\nabla^2 \phi = \nabla \cdot \left(M_s \underline{m} \right) \tag{17}$$

Substituting Equations (11) and (12) with the expression for $\underline{\underline{\varepsilon}}^m \left(\underline{m} \right)$ into Equation(13) which reduces to modified a partial differential equation relating to the displacements $\underline{u}$ and the magnetization $\underline{m}$:

$$\rho \frac{\partial^2 \underline{u}}{\partial t^2} - \nabla \cdot \underline{\underline{\underline{\underline{C}}}} \left[\frac{1}{2} \left(\nabla \underline{u} + \left(\nabla \underline{u} \right)^T \right) \right] + \nabla \cdot \underline{\underline{\underline{\underline{C}}}} \left(\underline{\underline{\underline{\lambda}}}^m \underline{m} \underline{m}^T \right) = \underline{0} \tag{18}$$

Combining Equations (14) and (16) produces the final three partial differential equations as a function of the displacement $\underline{u}$, the magnetic potential ϕ, and the magnetization $\underline{m}$:

$$\frac{\partial \underline{m}}{\partial t} = -\mu_0 \gamma \left(\underline{m} \times \left(\underline{H}_{ext} + \underline{H}_{ex}(\underline{m}) + \underline{H}_d(\phi) + \underline{H}_{anis}(\underline{m}) + \underline{H}_{me}(\underline{m}, \underline{u}) \right) \right) + \alpha \left(\underline{m} \times \frac{\partial \underline{m}}{\partial t} \right) \tag{19}$$

Equations (17), (18), and (19) are a system of the seven coupled partial differential equations for the seven unknown variables represented by $\underline{u}$, ϕ, and $\underline{m}$. To solve this system of coupled equations, the PDEs are formulated in their weak forms. The weak form of Equation(17) is

obtained by multiplying with a test functions ζ, which satisfies boundary conditions and the governing equation with this set integrated over the volume Ω. After integrating by parts and using the divergence theorem, we obtain [62]

$$-\int_{\Omega}(\nabla\phi)\frac{\partial\zeta}{\partial\underline{x}}d\Omega+\int_{\Omega}\left(M_s\underline{m}\right)\frac{\partial\zeta}{\partial\underline{x}}d\Omega=0 \qquad (20)$$

with prescribed magnetic potential boundary conditions [62],

$$\begin{cases}\phi_{in}=\phi_{out}\\ \dfrac{\partial\phi_{in}}{\partial n}-\dfrac{\partial\phi_{out}}{\partial n}=-\left(M_s\underline{m}\right)\cdot n\end{cases}\quad \textbf{on } S \qquad \textbf{(21)}$$

where ϕ_{in} and ϕ_{out} are the inner and outer magnetic potentials and $\hat{n}$ is the unit normal to the surface S.

Similarly, the weak formulation for Equation(18) is obtained by multiplying with a test vector function ($\underline{\eta}$) and integrating over the volume Ω. After integrating by parts and applying the divergence theorem, we obtain [56]

$$\int_{\Omega}\left(\rho\frac{\partial^2\underline{u}}{\partial t^2}\right)\cdot\underline{\eta}d\Omega+\int_{\Omega}\nabla\underline{\eta}\cdot\left(\underline{\underline{\underline{C}}}\left[\frac{1}{2}\left(\nabla\underline{u}+\left(\nabla\underline{u}\right)^T\right)\right]\right)d\Omega+\int_{\Omega}\nabla\cdot\underline{\underline{\underline{C}}}\left(\underline{\underline{\underline{\lambda}}}^m\underline{\underline{m}}\underline{\underline{m}}^T\right)\cdot\underline{\eta}d\Omega=\int_S\underline{\eta}\cdot\underline{\underline{\underline{C}}}\left[\frac{1}{2}\left(\nabla\underline{u}+\left(\nabla\underline{u}\right)^T\right)\right]\cdot ndS \quad (22)$$

with prescribed displacements and prescribed tractions on boundaries,

$$\underline{u}=\underline{u}^0 \qquad \text{on } S_1$$

$$\underline{\underline{\sigma}}\cdot\hat{n}=\underline{t} \qquad \text{on } S_2 \qquad (23)$$

where S_1 and S_2 are sub-boundaries on S ($S_1 \cup S_2 = S$).

Finally, to construct the weak form of Equation(19), we multiply the test vector functions $\underline{\psi}$ and integrate over the volume Ω. After integrating $\underline{H}_{ex}$ by parts, the weak form is [63]

$$\int_\Omega \left(\frac{\partial \underline{m}}{\partial t} - \alpha \left(\underline{m} \times \frac{\partial \underline{m}}{\partial t} \right) \right) \cdot \underline{\psi} d\Omega =$$

$$-\int_\Omega \mu_0 \gamma \left(\underline{m} \times \left(\underline{H}_{ext} + \underline{H}_d + \underline{H}_{anis} + \underline{H}_{me} \right) \right) \cdot \underline{\psi} d\Omega + \frac{2A_{ex}\gamma}{M_s} \sum_l \int_\Omega \left(\underline{m} \times \frac{\partial \underline{m}}{\partial x_l} \right) \cdot \frac{\partial \psi_l}{\partial x_l} d\Omega \qquad \textbf{(24)}$$

with the boundary condition

$$\frac{\partial \underline{m}}{\partial n} = 0 \qquad \text{on } S \qquad (25)$$

and subject to the constraint by definition

$$\left| \underline{m} \right| = 1 \qquad \text{on } \Omega \qquad (26)$$

Equations (20), (22), and (24) are subject to the boundary conditions given in Equations(21), (23), and (25), representing a well-posed problem that can be solved using finite element methods.

2.3 Simulation

The weak forms of Equations (20), (22), and (24) [62] are solved using finite element methods with an implicit time stepping scheme and the backward differentiation formula (BDF). In order to decrease solution time, the system of equations with ϕ, $\underline{m}$, $\underline{u}$ is solved using a segregated solution approach, which splits the solution process into substeps using a damped Newton's method. In this work, we have implemented the mathematical model (see the flowchart in Figure 2.1) in a commercially available partial differential equation solver in COMSOL. In general, as shown in Figure 2.1, initial conditions are first applied, followed by a Newton iteration approach that is used to converge for a given time step. Once converged, the time step is advanced and the process is repeated. The mathematical model described in this work can be similarly implemented in other finite element or numerical analysis packages, which provide platforms used to solve partial differential equations. For all of the numerical problems, convergent studies (i.e. mesh size and time steps) were conducted to ensure accuracy. The model was compared with experimental data for validation.

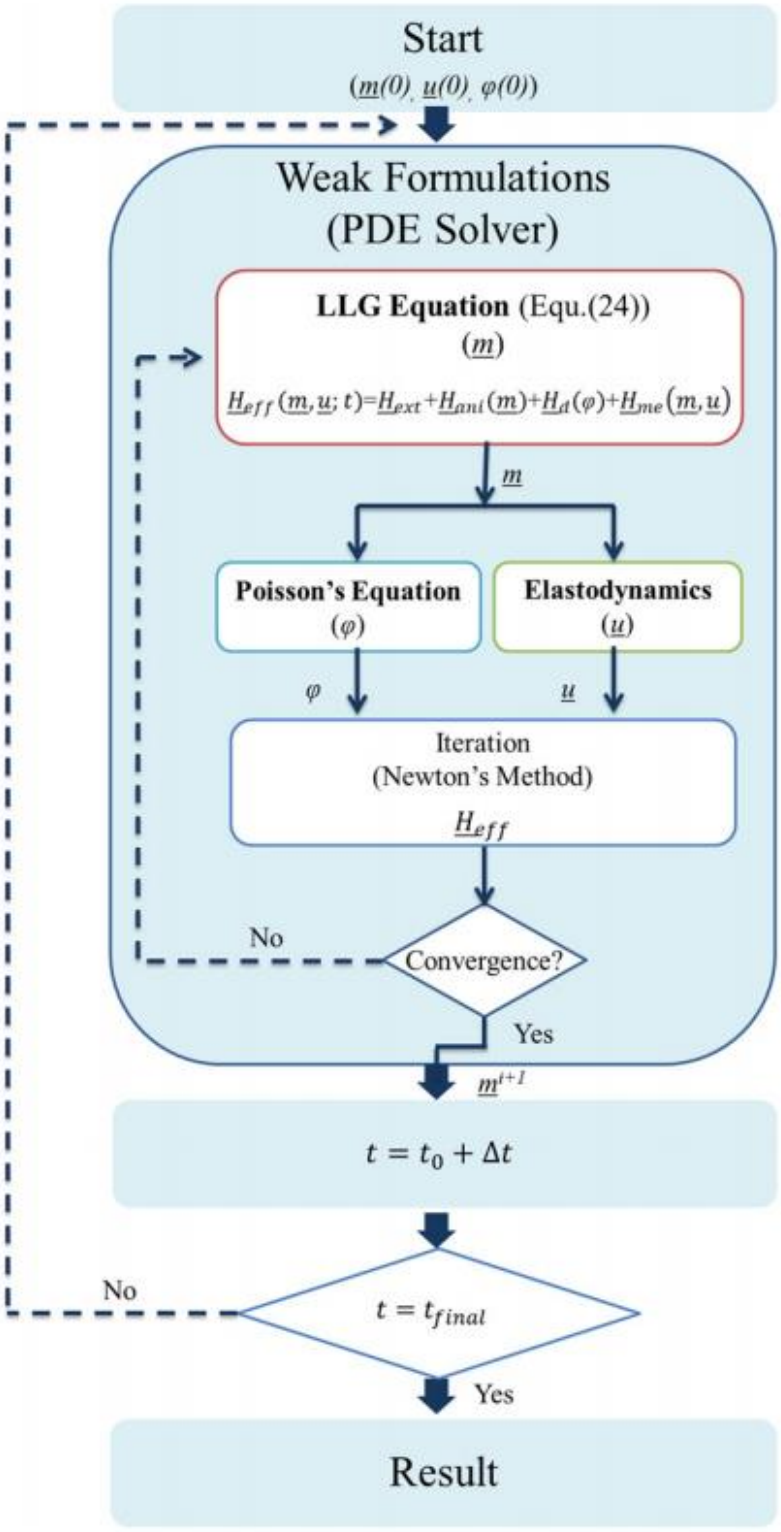

Figure 2.1: Flowchart of the fully-coupled FEM simulation.

Experimental tests have been previously conducted by Bur et al. [52] on 100 nm × 300 nm × 35 nm nickel nanostructures attached to a SiO_2 substrate subjected to mechanical loads. In their study, the change of the M vs. H curve as a response to applied mechanical loads was reported. An illustration of the finite element model used to analyze the experimental data is shown in Figure 2.2a. The nickel nanostructure was assumed to be perfectly bonded to the substrate. The structure shown in Figure 2.2b is discretized using tetrahedral elements with a size on the order of nickel's exchange length. The nickel properties [4] used were $M_s = 4.8\times10^5 (A/m)$; $A_{ex} = 1.05\times10^{-11} (J/m)$; $\lambda_{100} = -46\times10^{-6}$, $\lambda_{111} = -24\times10^{-6}$, $c_{11} = 2.5\times10^{11} (N/m^2)$, $c_{12} = 1.6\times10^{11} (N/m^2)$, and $c_{44} = 1.18\times10^{11} (N/m^2)$. The exchange length, defined as $\sqrt{\frac{2A}{\mu_0 M_s^2}}$, is 8.5 nm for nickel. The Gilbert damping constant was set as $\alpha = 0.5$ to improve stability and process time. The Young's modulus and Poisson's ratio of the isotropic substrate (SiO_2) used were $E_{SiO_2} = 70(Gpa)$ and $\upsilon = 0.2$, respectively.

Figure 2.2b illustrates the magnetic field direction and boundary conditions. The external magnetic field was applied along the y-direction. Displacements were applied on the SiO_2 boundaries at x=1000 nm and y=1000 nm to induce relative strains ($\varepsilon_{yy} - \varepsilon_{xx}$) of -1210, -671, 260, 0, 235, 645, and 1060 $\mu\varepsilon$, where $\varepsilon_{xx} = -\nu\varepsilon_{yy}$ in the effective substrate. Roller conditions were used along the planes at x=0 and y=0. The displacement conditions were initially applied and the magnetization states for all elements were allowed to reach equilibrium. Subsequently, an external magnetic field (H_{ext}) was first varied from 0 to 1250 Oe followed by a reduction to -1250 Oe and finally back to 0 Oe. In the applied field region of -750~-250 Oe and 250~750 Oe which represents values near the coercive field H_c, the field values were incremented by 15 Oe

while for all other field regions the increments were 250 Oe. The magnetization of the nickel nanostructure in the y direction at each applied field was determined by volume averaging the y-component of magnetization throughout the Ni nanostructure.

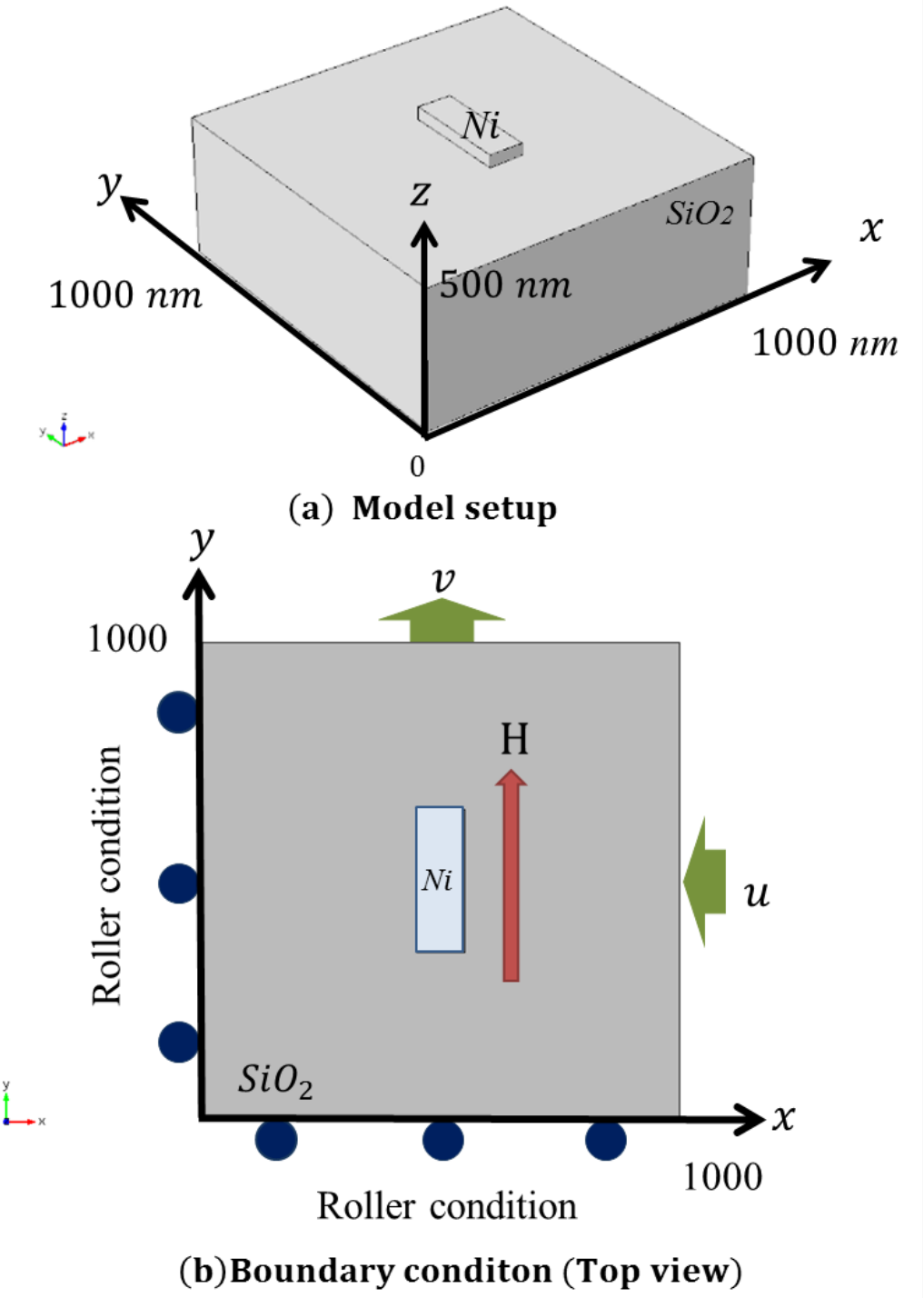

Figure 2.2: Schematic diagram of the model and boundary conditions.

2.4 Results and Discussion

In this section, experimental data [52] is compared to three different analytical models. The three models are 1) the SW model, assuming cooperative spin and constant strain [60], 2) the LLG micromagnetic model assuming spatially (homogeneous) uniform strain (ε=constant) [44][64][61], and 3) the proposed model of LLG with equations of elastodynamics (LLG/EQ) derived in the analytical section of this document. This section makes use of the term "magnetostrictive strain" to describe the local strain experienced by the magnetic nanostructure as a response to the applied displacement (i.e. effective $\varepsilon_{yy} - \varepsilon_{xx}$ in the substrate). The following paragraphs provide results for strain distribution, magnetic hysteresis curves, coercive field values, and magnetostrictive strains as a function of magnetic field.

In Figure 2.3, experimental results and analytical results for the volume-averaged normalized magnetization M vs. applied H in the nickel nanostructure are plotted for the SW model, the LLG model, and the LLG/EQ model. Each figure is evaluated for seven different applied displacements/strains ($\varepsilon_{yy} - \varepsilon_{xx}$). In general, the area of all three hysteresis predictions (including experiments) decreases as the applied strains ($\varepsilon_{yy} - \varepsilon_{xx}$) increase. This trend is expected since nickel is a negative magnetostrictive material. The SW model is a single-domain/spin model to approximate M vs. H hysteresis curves and describe basic micromagnetic phenomenon. As can be seen in Figure 2b the SW model does not accurately predict experimental results [52] (Figure 2.3a). The SW hysteresis area is much larger than the experimental data (i.e. over 50% larger than experimental results). In addition, SW predicts sharp coercive field changes while experiments are considerably smoother near coercive fields. The LLG model and the LLG/EQ model provide much closer approximations to experimental data

when compared to SW. The LLG hysteresis curves are different than those from the LLG/EQ model with non-uniform strains, as shown in Figure 2.3c and Figure 2.3d. This is because the LLG model assumes constant strains and increases the amount of magnetoelastic energy input to the Ni nanostructures. In general the SW model for coherent spin behavior and the LLG model have significant disagreement with the experimental results, which cannot be used to design more complicated magnetic nanostructures, while the LLG/EQ model curves provides more accurate predictive results.

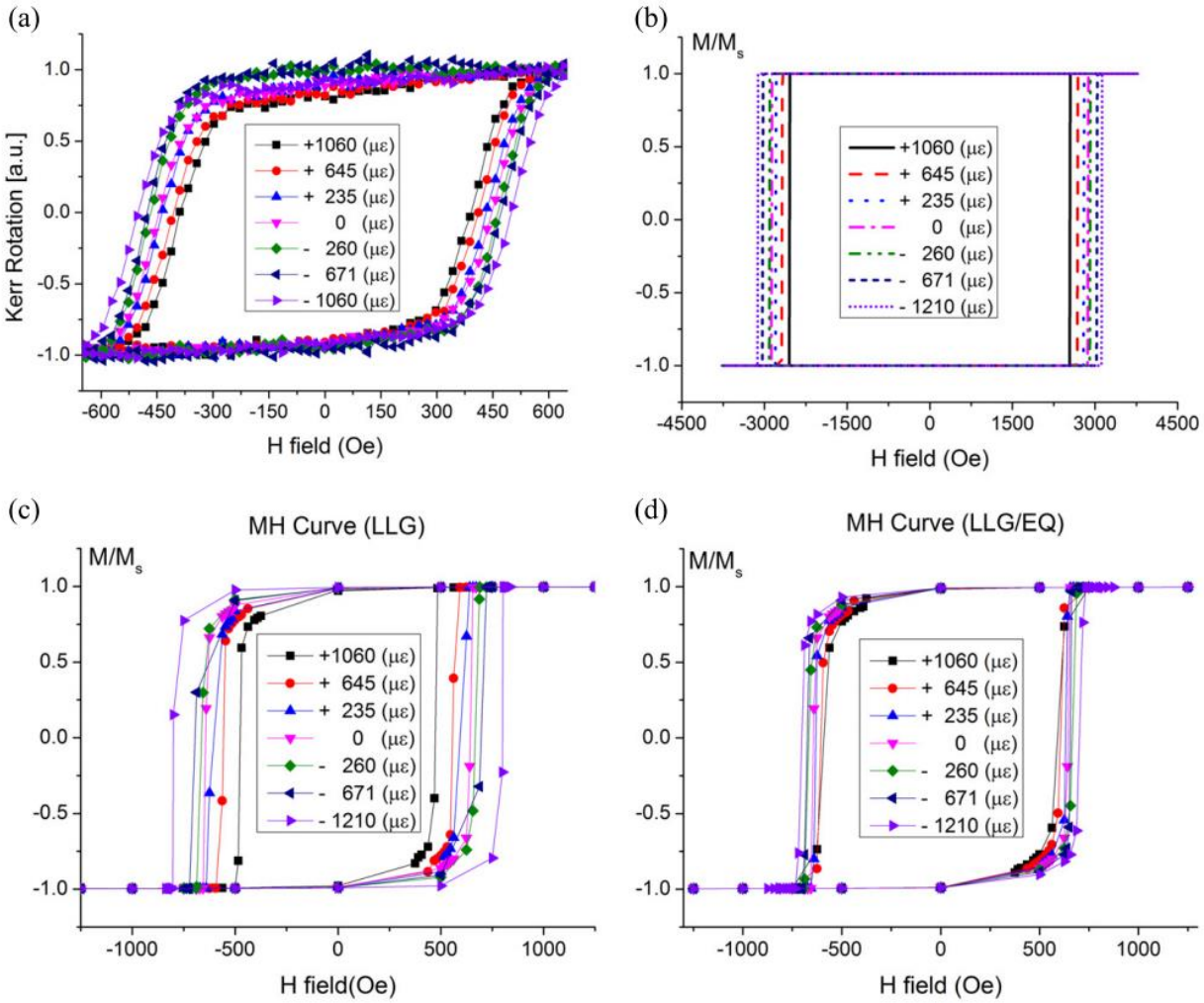

Figure 2.3: Hysteresis curves of external fields acting on the 100 nm × 300 nm × 35 nm Ni nanostructure generated using (a) experimental data (longitudinal MOKE) [52]**, (b) Stoner-Wolhfarth (SW) model, (c) LLG, and (d) LLG/EQ models for comparison, using volume-averaged values. The SW model displays impractically sharp hysteretic behavior due to its perfectly spin-oriented single domain assumption, and both the SW and traditional LLG models clearly show coercivity overestimation when compared to experimental data.**

Figure 2.4a compares the coercive fields H_c as a function of applied strain ($\varepsilon_{yy} - \varepsilon_{xx}$) for the SW model, the LLG model, the LLG/EQ model, and the experimental data. All curves show both a relatively linear relationship between H_c and the applied strains ($\varepsilon_{yy} - \varepsilon_{xx}$) with a decreasing H_c as the applied relative strain ($\varepsilon_{yy} - \varepsilon_{xx}$) increases. The SW model shows significant disagreement with the experimental data by as much as 2350 Oe, while the LLG model and LLG/EQ model results have relatively better agreement but differ as much as 200 Oe. Such inconsistencies in the analytical results are attributed to thermal issues, surface roughness, aspect ratio, or geometric smoothing in the nanostructure, which are not adequately represented in the simulations. In Figure 3b, the change in coercive field values (i.e., $\Delta H_c = H_c - H_c^0$) for the SW model ($\Delta H_c = 3\lambda_s E\left(\varepsilon_{yy} - \varepsilon_{xx}\right)/M_s$), the LLG model, the LLG/EQ model, and experiments are provided. The LLG/EQ model shows very good agreement with experiment data (less than 2% deviation) while the SW model and the LLG model both relatively poor agreement with errors as large as 60%. These set of comparisons clearly indicate that non-uniform strain distributions must be considered when predicting and understanding the strain-mediated magnetic anisotropic effect in nanostructures. Therefore, caution should be taken when using SW or LLG simulations in these finite size structures.

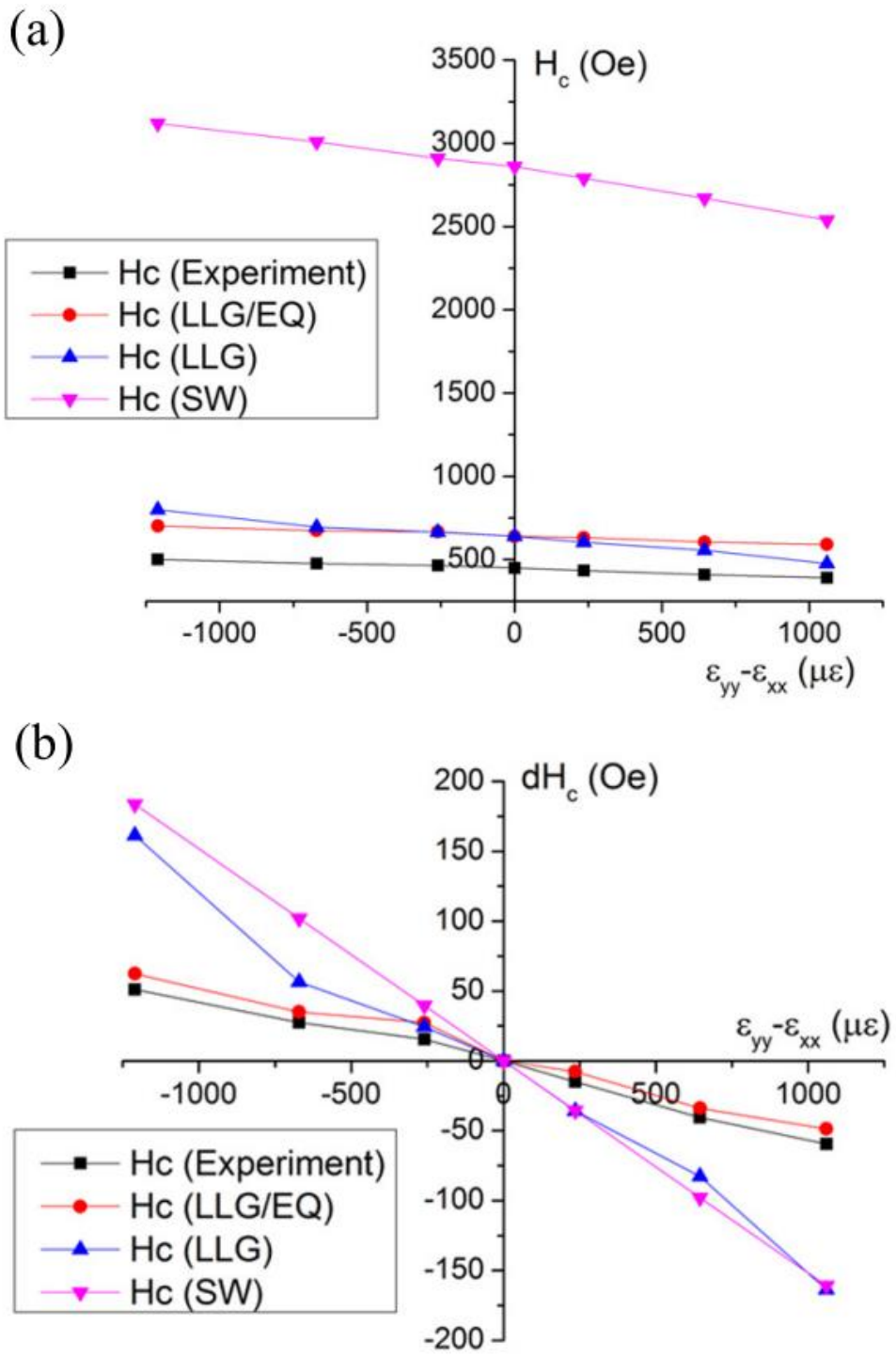

Figure 2.4: Comparison of experimental values [52] **with LLG/EQ, LLG, and Stoner-Wohlfarth models for (a) coercive field H_c and coercive difference ΔH_c, as a function of $\varepsilon_{yy} - \varepsilon_{xx}$ (b).**

Figure 2.5 shows analytical LLG/EQ results of the relative strain distribution in the Ni nanostructure with an effective applied strain $\varepsilon_{yy} - \varepsilon_{xx} = -671\mu\varepsilon$ and zero applied magnetic field. Figure 4a shows the surface plot for strains ($\varepsilon_{yy} - \varepsilon_{xx} = -671\mu\varepsilon$) in the nickel nanostructure. The simulation results clearly show that the strain distribution is non-uniform throughout the nanostructure. The relative strain values vary substantially between $-700\mu\varepsilon$ and $-80\mu\varepsilon$. Figure 4b plots the relative strain ($\varepsilon_{yy} - \varepsilon_{xx}$) as a function of *y* at *x* = 50nm for four different *z* values. Large strain variations are observed near the nanostructure ends (*y* = 0 nm and *y* = 300 nm), while the strain in the middle (*y* = 150 nm) is relatively uniform. The volume-averaged strain $\varepsilon_{yy} - \varepsilon_{xx}$ for the nickel nanostructure is $-322\mu\varepsilon$ and is 50% less than the applied strain. The strain variation as a function of position occurs due to a well-known phenomenon, classically referred to as shear lag in the mechanics community. Therefore, one can clearly see that the assumption of constant strain present in SW and LLG is inappropriate for this structure.

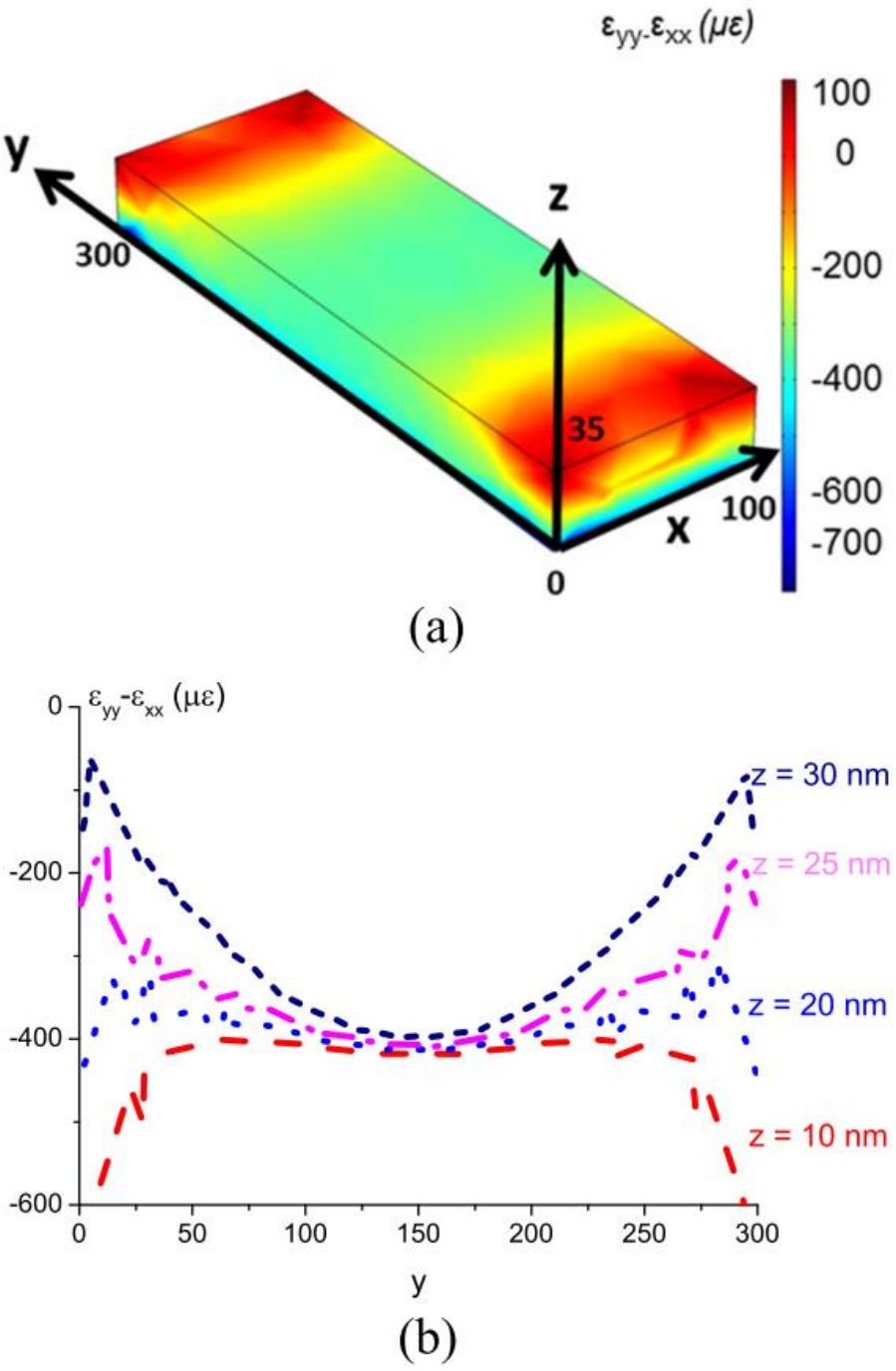

Figure 2.5: The non-uniform relative strain distributions in a 100 nm × 300 nm × 35 nm Ni nanostructure subjected to a strain of $\varepsilon_{yy} - \varepsilon_{xx} = -671\mu\varepsilon$, expressed as a surface plot of the non-uniform strain distribution in the nickel nanostructure (a) and relative strain $\varepsilon_{yy} - \varepsilon_{xx}$ as a function of *y* at different *z* values and *x* = 50 nm (b).

The LLG/EQ model is also able to predict the influence of magnetic field on magnetostrictive output strains which once again requires a fully coupled solution to accurately represent the response of a nanoscale structure. Figure 2.6 shows analytical results for the normalized magnetization M vs. applied H along the geometric hard y-axis (along the short width of the nanostructure) with an applied $\varepsilon_{yy} - \varepsilon_{xx} = -1210\mu\varepsilon$. Figure 2.7 shows the spin states and the surface strain plots for the magnetostrictive strain ($\varepsilon_{11}^{m} = \frac{3}{2}\lambda_{100}\left(m_1^2 - \frac{1}{3}\right)$) under different applied H in the *y*-axis. The complete hysteresis loop follows a chronological number sequence $(1 \rightarrow 5)$ as shown in Figure 2.6. The hysteresis loop begins at point 1 with zero applied field. When the applied field increases, the magnetization increases, saturating when the applied field is ~937 Oe (point 2). When the applied field is reversed, the normalized magnetization decreases to 0.1 at H = 0. The normalized magnetization is nonzero because remnant magnetic spins persist along the hard geometric axis of the nickel nanostructure. As the applied field becomes negative, the magnetization response asymmetrically mirrors the positive H as expected. Figure 2.7 plots magnetic spin states under the five applied fields (points 2 to 5) indicated in Figure 2.6. Without an applied field, the spins point along the geometric easy axis of the nanostructure. When a sufficiently large positive or negative field is applied along the *x*-axis, the spins form a flower state, fanning out along the *x*-axis to accommodate the demagnetization effect at the corners. Figure 6 shows the magnetostrictive strain (ε_{11}^{m}) distribution in the nickel nanostructure. When the applied field is zero, the magnetostrictive strain (ε_{11}^{m}) is fairly uniformly distributed through the nanostructure. When the applied field is large, the magnetostrictive strain (ε_{11}^{m}) is large in the middle of the nanostructure and is small at the corners, once again showing that constant strain assumptions are invalid.

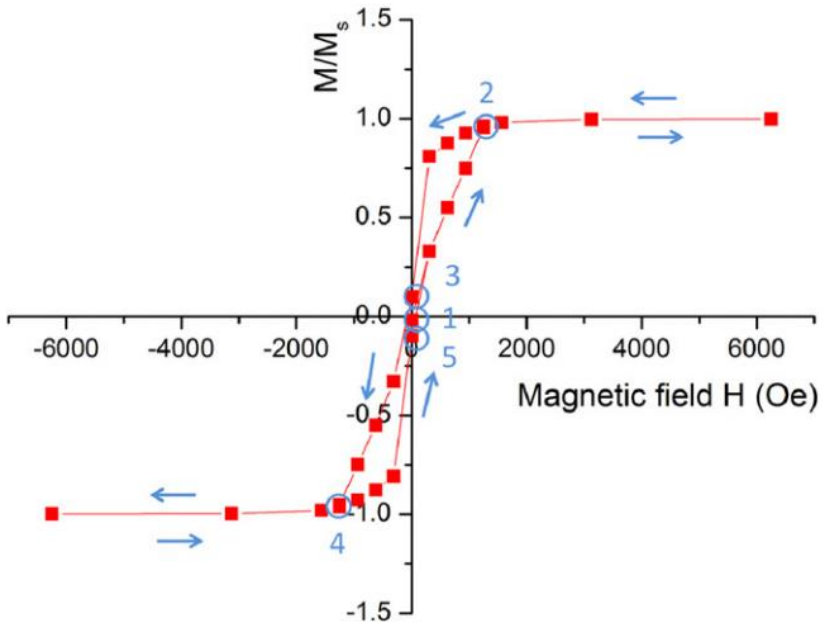

Figure 2.6: Hysteresis along the y-axis (y-axis) of the nanostructure under -1210 $\mu\varepsilon$.

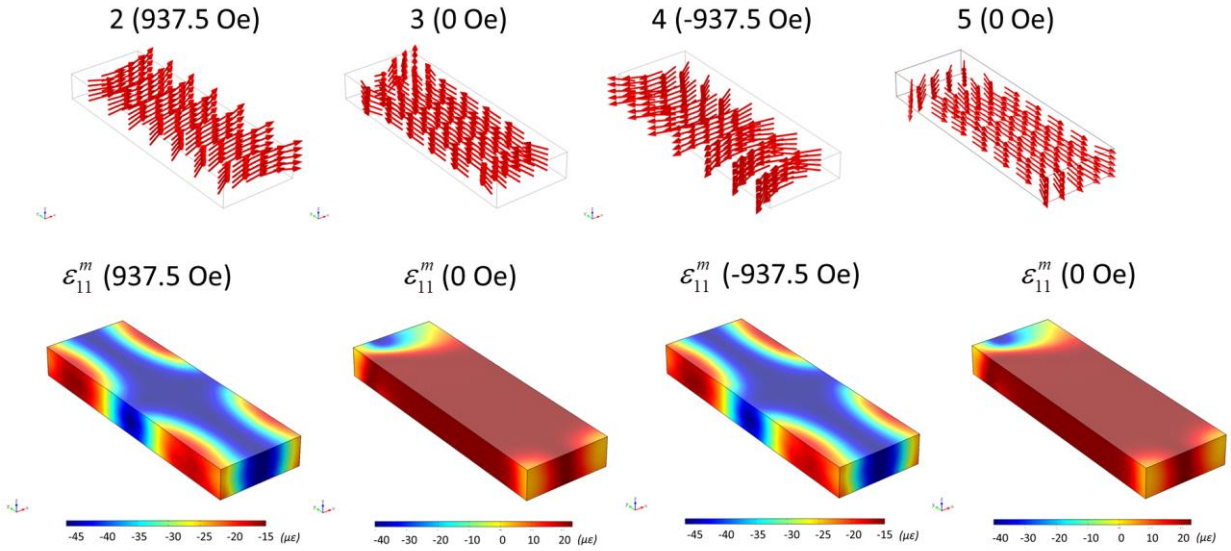

Figure 2.7: Spin states corresponding to hysteresis points in Figure 5 (top) and illustration of magnetostrictive strain (ε_{11}^m) in the nanostructure (bottom).

Figure 2.8 shows four ($\varepsilon_{22}^{m} = \frac{3}{2}\lambda_{100}\left(m_2^2 - \frac{1}{3}\right)$) magnetostrictive strain states and their corresponding applied field results for nickel nanostructure. As shown in Figure 2.7, the complete magnetization loop follows a chronological sequence ($1 \rightarrow 12$). Without the application of a magnetic field (point 1), the spin state is a single domain aligned along the long axis of the structure. The spins are uniformly pointing along the *y*-axis at the center of the nanostructure, which then fan outwards along the nanostructure toward the corners due to demagnetization effects. The magnetostrictive strain is $-44\mu\varepsilon$ in this initial state. When the magnetic field increases ($1 \rightarrow 3$), the spins at the corners are forced to saturate along the easy axis and the magnetostrictive strain decreases to $-46\mu\varepsilon$. When reversing the magnetic field ($3 \rightarrow 7$) to -560 Oe, there is a peak showing that the spin state forms an ordered 'S' shaped state within the structure. This is the critical field strength where the spins begin flipping to the opposite direction. The magnetostrictive strain is approximately $-10\mu\varepsilon$ in this state. As the field decreases ($7 \rightarrow 9$), the spins begin pointing along the negative *y*-axis. This presentation illustrates the complex states that the magnetic spins take and are strongly influenced by finite size or shear lag effects in the nanostructure, i.e. inhomogeneous strains.

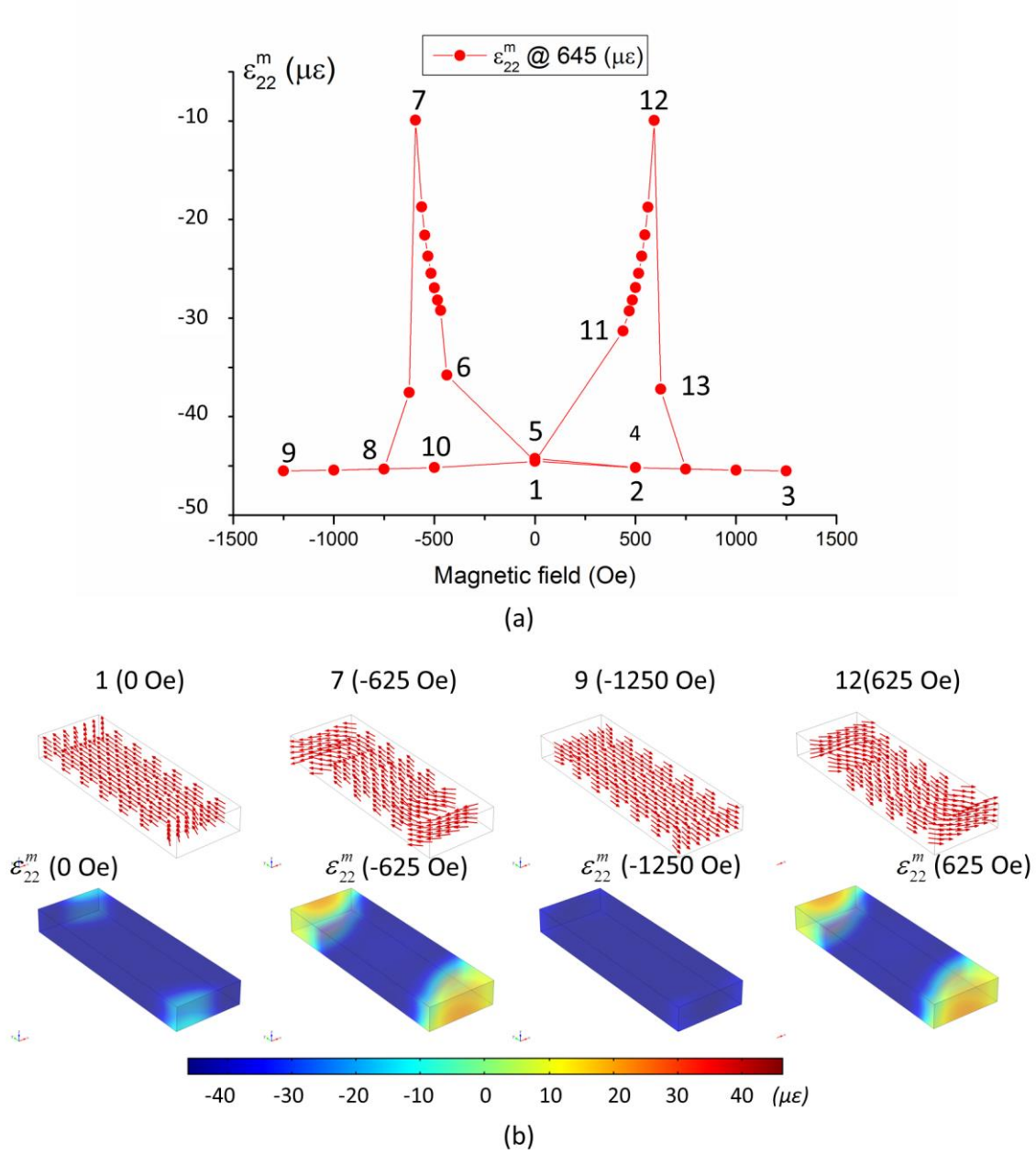

Figure 2.8: Magnetostrictive strain (vs.) applied magnetic fields (a), and nanostructure spin state at four distinct points of the graph (b, top) and their corresponding magnetostrictive strain states (b, bottom).

In conclusion, we have developed a numerical approach based on finite element for simulating magnetization states, magnetic hysteresis curves, and strain-induced coercive field changes in magnetic nanostructures by coupling the spatially-dependent strain state with micromagnetic simulation (LLG/EQ model) with elastodynamics. This model provides substantially better predictive results than the LLG model and the conventional Stoner-Wohlfarth (SW) model and in some cases must be used to accurately predict the response of a nanoscale structure. The LLG/EQ coupled model was verified with existing experimental data validating its predictive capabilities. In general this work strongly encourages researchers to use coupled solutions when modeling the magnetoelastic response of finite size structures to accurately predict the magnetoelastic response. This is important in a wide range of fields including memory, motors, and spin wave propagation.

3. Modeling of Magnetic Memory Device

This work presents an analytical model coupling Landau-Lifshitz-Gilbert micromagnetics with elastodynamics and electrostatics to model the response of a single domain magnetoelastic nano-element attached to a piezoelectric thin film (500 nm). The thin film piezoelectric is mounted on a Si substrate, globally clamping the film from in-plane extension or contraction. Local strain transfer to the magnetoelastic element is achieved using patterned electrodes. The system of equations is reduced to eight coupled partial differential equations as a function of voltage (V), magnetic potential ϕ, magnetic moments ($\underline{m}$), and displacements ($\underline{u}$), i.e. fully coupled material. The weak forms of the partial differential equations are solved using a finite element formulation. The problem of a Ni single domain structure (i.e. 150nm x 120nm x 10 nm) on a thin film (500nm) PZT-5H attached to an infinite substrate is studied. Discretization in the single domain structure is on the order of the exchange length (8.5nm), providing spatial and temporal information on the local mechanical and magnetic fields. A -0.5 V potential is applied to a pair of surface electrodes, producing out-of-plane deformation and in turn straining the magnetoelastic single domain nanostructure in-plane. This strain is sufficient to reorient a single domain structure representative of an idealized memory element.

3.1 Introduction and Background

For the past decade, researchers have focused on developing a magnetic memory element using a multiferroic material [65]. One approach uses a strain-mediated composite approach consisting of layered piezoelectric and magnetoelastic materials strain coupled together [48][66] [67]. Researchers have analytically shown that the energy required to reorient/write a single magnetic domain structure can be very small, i.e. considerably smaller than conventional approaches to writing bits of memory [29] [43][68][69]. However, the multiferroic composite memory element is typically fabricated on a fairly thick substrate system, e.g. silicon. This thick substrate clamps the piezoelectric/magnetoelastic material, limiting the amount of strain that can be generated, posing a significant challenge for the implementation of a strain-mediated memory element. In this analytical work we demonstrate a concept to overcome the substrate clamping issue and show reorientation of a magnetic single domain between two stable states by simply pulsing the voltage.

Previous researchers have demonstrated the control of the magnetization states in thin film magnetoelastic material deposited on a thick piezoelectric substrate [70]–[74]. This effect has been used to alter magnetic domains [48][66][71][72] and to shift the magnetic coercive field [73][74]. As an alternative to using in-plane polarized piezoelectric material, some researchers such as Wu used the auxetic piezoelectric strain produced by [011] cut PMN-PT, while others have used the same effect in PZN-PT single crystals [75][76]. These single crystal approaches resulted in a proposed design of a magnetoelectric memory system, but once again still required bulk piezoelectric material [41][68]. Moutis et al. in 2008 reported electric-field modulation of coercive field H_c using periodic arrays of ferromagnetic (FM) $Co_{50}Fe_{50}$ stripes [77]. Bur et al. in

2011 reported strain-induced coercive field changes in patterned single-domain nickel nanostructures deposited on a thick Si/SiO_2 substrate using external mechanical loads [52], while Nan et al. suggested single domain reorientation on bulk PMN-PT single crystal [68]. Regarding piezoelectric materials deposited onto a substrate, out-of-plane magnetic reorientation has been achieved with magnetic BFO/CFO vertical nanoscale structures embedded in a ferroelectric thin film, as described by Zavaliche et al. in 2005, but this approach is non-deterministic [78]. Chung et al. studied single domain elements on a thin film piezoelectric, but did not demonstrate reorientation of the magnetic domain [71][72]. None of these studies provides an acceptable approach to reorient a single domain structure deterministically using strain-mediated approach on a constrained substrate.

The development of a strain-mediated multiferroic memory device requires the magnetization of each element to be individually controllable using a ferroelectric thin film grown on a substrate (e.g. Si wafer). The problem with this concept it that the thin film piezoelectric is clamped by the thick substrate and prevents strain transfer. Cui et al. suggested the use of patterned electrodes to overcome substrate clamping and obtain highly localized strain in both the thin film piezoelectric and the magnetic material [79]. The general concept was demonstrated on a bulk piezoelectric ceramic, but did not include detailed analysis (or experiments) for a thin film piezoelectric.

The analysis of single domain switchable magnetoelectric heterostructures requires the use of the Landau-Lifshitz-Gilbert LLG micromagnetic approaches developed in the 1950s [61]. An important addition to micromagnetics was the inclusion of strain (or stress) for magnetostrictive materials by Zhu et al. in 2001 [44]. This was used by Hu in 2006 to model the

effect of stress on hysteresis curves and magnetization dynamics, showing the interaction of stress with coercivity and the easy axis of magnetoelastic materials [64]. Building on these advancements, Hu et al. used stability conditions and proposed an electric field read and write MERAM device [43]. A balance of both shape and strain anisotropy was used to describe an elliptical nanomagnet that could be switched under stress by Roy et al. [29]. In most of these studies, however, magnetization and strain were assumed to be spatially homogeneous and thus the clamping issues produced by the substrate were not addressed. D'Souza et al. in 2011 proposed and analyzed a low-power 4-state universal logic gate using a linear array of multiferroic nanomagnets, but did not consider the substrate clamping issue [80]. Tiercelin et al. described and analyzed a magnetoelectric memory cell that balanced strain anisotropy, shape anisotropy, and a bias field [69]. In this later work the elastic contribution was modeled separately and the piezoelectric film was not attached to a substrate.

In this work, a single domain magnetoelastic elliptical nanostructure deposited onto a thin film piezoelectric wafer attached to a thick substrate is modeled by coupling micromagnetics (LLG), elastodynamic, and electrostatics partial differential equations. The nickel magnetoelastic ellipse (150 nm x 120 nm x 10 nm) has shape anisotropy and an applied magnetic field along the minor axis to shift the energy wells, as described originally by Tiercelin in 2011 [69]. The thin film (500 nm) piezoelectric is attached to a thick substrate that clamps and prevents relative in-plane motion of the piezoelectric at the interface of the film with the substrate. Four electrodes are placed around the Ni magnetoelastic element similar to Tiercelin [69]; however, these electrodes produce out-of-plane electric fields rather than in-plane electric fields [79], and the thin film is mounted onto a substrate. The intrinsic coupling of the piezoelectric response with the magnetoelastic response through strain is modeled by coupled partial differential equations

(i.e. electrostatics tied to micromagnetics while solving elastodynamics). The numerical formulation uses tetrahedral finite elements with a maximum size equal to the exchange length of nickel (~8.5 nm), providing spatially varying strains, electric fields, and magnetic spins throughout the structure. Therefore, the model captures all the relevant physics required to accurately predict the response of this multiferroic nanoscale structure and demonstrates single domain magnetic reorientation in a strain-mediated structure attached to a thick clamped substrate.

3.2 Theory for Computational Model

Strain-mediated multiferroic composites consist of both piezoelectric and magnetoelastic materials. Thus, the fundamental governing equations for predicting the dynamic response are based on electrostatics, micromagnetics (LLG), and elastodynamics. In this work, the general governing equations for a strain-mediated electro-mechanical and magnetoelastic materials are derived, from which individual phases represent limiting cases. The following derivation presents a general approach for developing the governing equations in weak forms, which are then implemented into a finite element formulation. Assumptions include small elastic deformations, linear elasticity, linear piezoelectricity, electrostatics, and negligible electrical current contributions. The single general derivation presented can be subsequently decoupled to predict the response of an electro-mechanical or magnetoelastic material.

The strain for a multiferroic (magneto-electric-elastic) material is given by

$$\underline{\underline{\varepsilon}} = \underline{\underline{\varepsilon}}^{el} + \underline{\underline{\varepsilon}}^{PE} + \underline{\underline{\varepsilon}}^{m}\left(\underline{m}\right) \tag{27}$$

where $\underline{\underline{\varepsilon}}$ is the total strain with contributions from the elastic strain $\underline{\underline{\varepsilon}}^{el} = \underline{\underline{\underline{\underline{C}}}}^{-1}\underline{\underline{\sigma}}$, the piezoelectric strain $\underline{\underline{\varepsilon}}^{PE} = \underline{\underline{\underline{d}}}\,\underline{E}$, and the magnetostriction strain $\underline{\underline{\varepsilon}}^{m} = \underline{\underline{\underline{\underline{\lambda}}}}^{m}\,\underline{\boldsymbol{m}}\underline{\boldsymbol{m}}^{T}$. Here $\underline{\underline{\underline{\underline{C}}}}$ is the elastic stiffness tensor, $\underline{\underline{\sigma}}$ is the stress tensor, $\underline{\underline{\underline{d}}}$ is the piezoelectric strain tensor, $\underline{E}$ is the electric field vector, $\underline{\underline{\underline{\underline{\lambda}}}}$ is the magneto-mechanical coupling tensor, and $\underline{m} = \dfrac{M}{M_s}$ is the normalized local magnetization vector with M_s representing saturation magnetization. For a cubic crystal, the components of $\underline{\underline{\varepsilon}}^{m}$ in a cubic referenced coordinate system are given by

$$\varepsilon_{ij}^{m} = \begin{cases} \frac{3}{2}\lambda_{100}\left(m_i m_j - \frac{1}{3}\right) & i = j \\ \frac{3}{2}\lambda_{111} m_i m_j & i \neq j \end{cases} \tag{28}$$

where λ_{100} and λ_{111} are magnetostriction constants along the $\langle 100 \rangle$ and $\langle 111 \rangle$ directions [3][54][56][57][4]. For hexagonal or uniaxial crystals, equation (2) would have a different form that can easily be implemented in the approach [4], and for an isotropic polycrystalline the two coefficients have the same value.

The electrical portion of the constitutive equation, assuming negligible magnetic and electric field coupling, is given by

$$\underline{D} = \underline{\underline{d}}^{T} \underline{\underline{\sigma}} + \varepsilon_s \underline{E} \tag{29}$$

where $\underline{\underline{\varepsilon_s}}$ is the dielectric tensor and $\underline{D}$ is the electric displacement. For a general multiferroic material, an additional term would appear in equation (3) representing the coupling between magnetic and electric fields, but for this derivation we have assumed this component is negligible. The coupling between magnetic and electric fields in the material modeled in this work arises due to the stress term in equation (3) and its coupling to magnetic strain presented in equation (1). The electrostatic governing equations are

$$\begin{aligned} \nabla \cdot \underline{D} &= \rho_f \\ \underline{E} &= -\nabla V \end{aligned} \tag{30}$$

where V is the electric potential and ρ_f is density of free charges. The electric potential V is obtained by combining equations (3) and (4) for electrostatic behavior ($\rho_f = 0$):

$$\nabla \cdot \left[\underline{\underline{d}}^T \underline{\underline{\sigma}} + \varepsilon_s \left(-\nabla V \right) \right] = 0 \tag{31}$$

The magnetic response of the multiferroic media is governed by the phenomenological Landau-Lifshitz-Gilbert (LLG) micromagnetic relation

$$\frac{\partial \underline{m}}{\partial t} = -\mu_0 \gamma \left(\underline{m} \times \underline{H}_{eff} \right) + \alpha \left(\underline{m} \times \frac{\partial \underline{m}}{\partial t} \right) \tag{32}$$

where μ_0 is the permeability in the vacuum, γ is the Gilbert gyromagnetic ratio, and α is the Gilbert damping constant [61]. $\underline{H}^{eff}$ is the effective magnetic field, which is obtained from the total energy density and is given by

$$\underline{H}_{eff} = -\frac{1}{\mu_0 M_S} \frac{\partial E_{tot}}{\partial \underline{m}} = \underline{H}_{ext} + \underline{H}_{ex} + \underline{H}_{anis} + \underline{H}_d + \underline{H}_{me} \left(\underline{m}, \underline{u}(\underline{E}) \right) \tag{33}$$

where E_{tot} is the total energy density, which includes the Zeeman energy density due to an applied external field, the exchange energy density, the magnetocrystalline anisotropy energy density, the demagnetization energy density, and the elastic energy density [56][57][61]. $\underline{H}_{ext}$ is the applied external field, $\underline{H}_{ex}$ is the exchange field, $\underline{H}_{anis}$ is the anisotropic field, $\underline{H}_d$ is the demagnetization field and $\underline{H}_{me}$ is the magnetoelastic field. Expressions for these terms follow

$$\underline{H}_{ex} = \frac{2A_{ex}}{\mu_0 M_s} \nabla^2 \underline{m} \tag{8.1}$$

$$H^i{}_{anis} = -\frac{2m_i}{\mu_0 M_S} \left[K_1 \left(m_j^2 + m_k^2 \right) + K_2 \left(m_j^2 m_k^2 \right) \right] \tag{34.2}$$

where K_1 and K_2 are cubic anisotropy constants [54][56][57][61]. The equation for the anisotropy field H^{i}_{anis} will take a different form for other crystal symmetries. The demagnetization field $\underline{H}_d$ is determined from Ampere's law ($\nabla \times \underline{H}_d = 0$), Gauss's law ($\nabla \cdot \underline{B} = 0$), and the relation between the magnetic induction $\underline{B}$ and magnetization $\underline{m}$:

$$\underline{B} = \underline{H}_d + M_s \underline{m} \tag{35}$$

$\underline{H}_d$ is expressed as the gradient of a magnetic potential ϕ by using Ampere's law [62]:

$$\underline{H}_d = -\nabla \phi \tag{36}$$

Using Gauss's law with equations (9) and (10), the magnetic potential ϕ satisfies the Poisson equation [62]:

$$\nabla^2 \phi = \nabla \cdot \left(M_s \underline{m} \right) \tag{37}$$

The magnetoelastic field is obtained by differentiating the elastic energy density in equation (7) [54]:

$$\underline{H}_{me} = -\frac{1}{\mu_0 M_S} \underline{\underline{\underline{C}}} \left(\underline{\underline{\varepsilon}} - \underline{\underline{\varepsilon}}^{m} \left(\underline{m} \right) - \underline{\underline{\varepsilon}}^{PE} \left(\underline{E} \right) \right) \cdot \frac{\partial \underline{\underline{\varepsilon}}^{m} \left(\underline{m} \right)}{\partial \underline{m}} \tag{38}$$

The mechanical response of the is governed by the elastodynamic equation

$$\rho \frac{\partial^2 \underline{u}}{\partial t^2} - \nabla \cdot \underline{\underline{\sigma}} = \underline{0} \tag{39}$$

where ρ is the mass density. The total strain $\underline{\underline{\varepsilon}}$ from equation (1) is related to the displacement $\underline{u}$ vector [54] as

$$\underline{\underline{\varepsilon}} = \frac{1}{2}\left(\nabla \underline{u} + \left(\nabla \underline{u}\right)^T\right) \tag{40}$$

and the stress tensor $\underline{\underline{\sigma}}$ is related to the strains [54] as:

$$\underline{\underline{\sigma}} = \underline{\underline{\underline{\underline{C}}}}\,\underline{\underline{\varepsilon}}^{el} = \underline{\underline{\underline{\underline{C}}}}\left[\underline{\underline{\varepsilon}} - \underline{\underline{\varepsilon}}^{m}\left(\underline{m}\right) - \underline{\underline{\varepsilon}}^{PE}\left(\underline{E}\right)\right] \tag{41}$$

Equations (1) - (15) represent a system of equations describing the electro-magneto-mechanical response. Substituting equations (14) and (15) and the expression for $\underline{\underline{\varepsilon}}^{m}\left(\underline{m}\right)$ into equation (13) results in a modified elastodynamic partial differential equation in terms of displacements $\underline{u}$, electric field $\underline{E}$ and magnetization $\underline{m}$ [57]:

$$\rho\frac{\partial^2 \underline{u}}{\partial t^2} - \nabla\cdot\underline{\underline{\underline{\underline{C}}}}\left[\frac{1}{2}\left(\nabla \underline{u} + \left(\nabla \underline{u}\right)^T\right)\right] + \nabla\cdot\underline{\underline{\underline{\underline{C}}}}\left(\underline{\underline{\lambda}}^{m}\,\underline{m}\underline{m}^T\right) + \nabla\cdot\underline{\underline{\underline{\underline{C}}}}\left(\underline{\underline{d}}\,\underline{E}\right) = \underline{0} \tag{42}$$

where the electric field E is obtained from equation (4). Note that the partial differential equation is fully coupled with electric ($\underline{E}(V)$), magnetic ($\underline{m}$), and mechanical displacement fields ($\underline{u}$); thus a fully coupled multiferroic material is modeled. Combining equations (6) and (7) produces the modified LLG equation in terms of displacements ($\underline{u}$), electric field ($\underline{E}$) and magnetization ($\underline{m}$):

$$\frac{\partial \underline{m}}{\partial t} = -\mu_0\gamma\left(\underline{m}\times\left(\underline{H}_{ext} + \underline{H}_{ex}(\underline{m}) + \underline{H}_{d}(\phi) + \underline{H}_{anis}(\underline{m}) + \underline{H}_{me}(\underline{m},\underline{u}(\underline{E}))\right)\right) + \alpha\left(\underline{m}\times\frac{\partial \underline{m}}{\partial t}\right) \tag{43}$$

Equations (5), (11), (16) and (17) represent eight fully coupled partial differential equations for the eight unknown variables represented by V, $\underline{u}$, ϕ and $\underline{m}$. In this work, the coupled PDEs are formulated in their weak forms. The weak form of equation (5) is obtained by multiplying it by test functions β which satisfy boundary conditions, and then integrating over the volume Ω. Using the divergence theorem [62] gives

$$\begin{aligned}&\int_{\Omega}\left(\varepsilon_s-\underline{\underline{d}}\,\underline{\underline{\underline{\underline{C}}}}\,\underline{\underline{d}}^T\right)(-\nabla V)\frac{\partial\beta}{\partial\underline{x}}d\Omega+\int_{\Omega}\left(\underline{\underline{d}}^T\,\underline{\underline{\underline{\underline{C}}}}\left(\frac{1}{2}\left(\nabla\underline{u}+(\nabla\underline{u})^T\right)-\underline{\underline{\underline{\lambda}}}^m\,\underline{\underline{m}}\,\underline{\underline{m}}^T\right)\right)\frac{\partial\beta}{\partial\underline{x}}d\Omega=\\&\int_{S}\left(\varepsilon_s-\underline{\underline{d}}\,\underline{\underline{\underline{\underline{C}}}}\,\underline{\underline{d}}^T\right)(-\nabla V)\beta n dS+\int_{S}\left(\underline{\underline{d}}^T\,\underline{\underline{\underline{\underline{C}}}}\left(\frac{1}{2}\left(\nabla\underline{u}+(\nabla\underline{u})^T\right)-\underline{\underline{\underline{\lambda}}}^m\,\underline{\underline{m}}\,\underline{\underline{m}}^T\right)\right)\beta n dS\end{aligned} \tag{44}$$

with the following prescribed electric potential boundary conditions

$$V=V_0 \text{ on } S \tag{45}$$

where V_0 is the electric potential on the surface S. The weak form of equation (11) is obtained by using a test functions ζ [62] giving

$$-\int_{\Omega}(\nabla\phi)\frac{\partial\zeta}{\partial\underline{x}}d\Omega+\int_{\Omega}\left(M_s\underline{m}\right)\frac{\partial\zeta}{\partial\underline{x}}d\Omega+\int_{S}\left(-\nabla\phi+M_s\underline{m}\right)\zeta n dS=0 \tag{46}$$

With the following prescribed magnetic potential boundary conditions [62],

$$\begin{cases}\phi_{in}=\phi_{out}\\ \dfrac{\partial\phi_{in}}{\partial n}-\dfrac{\partial\phi_{out}}{\partial n}=-\left(M_s\underline{m}\right)\cdot n\end{cases} \text{ on } S \tag{47}$$

where ϕ_{in} and ϕ_{out} are the inner and outer magnetic potentials and $\hat{n}$ is the unit normal to the surface S. Similarly, the weak formulation for equation (16) is obtained by using test vector functions η [55], producing

$$\int_\Omega \left(\rho \frac{\partial^2 \underline{u}}{\partial t^2} \right) \cdot \underline{\eta} d\Omega + \int_\Omega \nabla \underline{\eta} \cdot \left(\underline{\underline{\underline{\underline{C}}}} \left[\frac{1}{2} \left(\nabla \underline{u} + (\nabla \underline{u})^T \right) \right] \right) d\Omega + \int_\Omega \left[\underline{\underline{\underline{\underline{C}}}} \left(\underline{\underline{\underline{\lambda}}}^m \underline{m}\underline{m}^T \right) + \underline{\underline{\underline{\underline{C}}}} \left(\underline{\underline{d}} (-\nabla V) \right) \right] \nabla \underline{\eta} d\Omega \quad (48)$$
$$= \int_S \underline{\eta} \cdot \underline{\underline{\underline{\underline{C}}}} \left[\frac{1}{2} \left(\nabla \underline{u} + (\nabla \underline{u})^T \right) - \left(\underline{\underline{\underline{\lambda}}}^m \underline{m}\underline{m}^T \right) - \left(\underline{\underline{d}} (-\nabla V) \right) \right] \cdot n dS$$

with prescribed displacements and prescribed tractions on the corresponding boundaries,

$$\underline{u} = \underline{u}^0 \qquad \text{on } S_1 \quad (23.1)$$

$$\underline{\underline{\sigma}} \cdot \hat{n} = \underline{t} \qquad \text{on } S_2 \quad (49.2)$$

where S_1 and S_2 are sub-boundaries on S ($S_1 \cup S_2 = S$). Finally, to construct the weak form of equation (17), the vector test function $\underline{\psi}$ is used to produce [55]

$$\int_\Omega \left(\frac{\partial \underline{m}}{\partial t} - \alpha \left(\underline{m} \times \frac{\partial \underline{m}}{\partial t} \right) \right) \cdot \underline{\psi} d\Omega =$$

$$-\int_\Omega \mu_0 \gamma \left(\underline{m} \times \left(\underline{H}_{ext} + \underline{H}_d + \underline{H}_{anis} + \underline{H}_{me} \right) \right) \cdot \underline{\psi} d\Omega + \frac{2A_{ex}\gamma}{M_s} \sum_l \int_\Omega \left(\underline{m} \times \frac{\partial \underline{m}}{\partial x_l} \right) \cdot \frac{\partial \psi_l}{\partial x_l} d\Omega \quad (50)$$

with the boundary condition [55][61]

$$\frac{\partial \underline{m}}{\partial n} = 0 \qquad \text{on } S \quad (51)$$

and subject to the constraint

$$|\underline{m}| = 1 \qquad \text{on } \Omega \tag{52}$$

which is a direct consequence of the LLG equation [55][61]. Finally, equations (18), (20), (22), and (24) in addition to the boundary conditions given in equations (19), (21), (23), and (25), represent a well-posed problem that can be solved using finite element methods.

The weak forms are solved using the finite element method with an implicit time stepping scheme and backward differentiation formula (BDF). To decrease solution time, the system of equations is solved using a segregated solution approach, which splits the solution process into substeps using a damped Newton's method. For all numerical problems, convergence studies (i.e., mesh size and time steps) were conducted to ensure accuracy. The time step is 5×10^{-11} s and duration is 2×10^{-12} s.

3.3 Results and Discussion

Prior to showing analytical results, we first describe the physical mechanism of deterministically reorienting the magnetization in a single domain element by 90 degrees using magnetoelastic properties [69]. Figure 3.1 shows the energy profiles as a function of the magnetization angle for two different nanoscale geometries (~100 nm, in-plane 10 nm thick), i.e. a circular Figure 3.1a or elliptical disk Figure 3.1b. For a circular disk, as shown in Figure 3.1a, there are no preferential magnetic energy wells, thus the in-plane magnetization direction is independent of angle. For an elliptical disk, as shown in Figure 3.1b, there are two energy minima aligned along the major axis at 0 and 180 degrees. By introducing a magnetic bias field (H_b) aligned along the ellipse's minor axis (see Figure 3.1c), the angle between the energy wells decreases, i.e. from 0/180 in Figure 3.1b to 45/135 in Figure 3.1c with H_b applied. The simultaneous application of a magnetic field and a mechanical strainto the magnetoelastic ellipse (e.g. negative magnetostriction), as shown in Figure 3.1d and Figure 3.1e, modifies the two energy wells magnitude relative to each other rather than substantially change the angle (i.e. 45/135). This approach, i.e. application of a constant magnetic bias field with the application and removal of a mechanical strain, allows deterministic strain-mediated switching between two stable states [69].

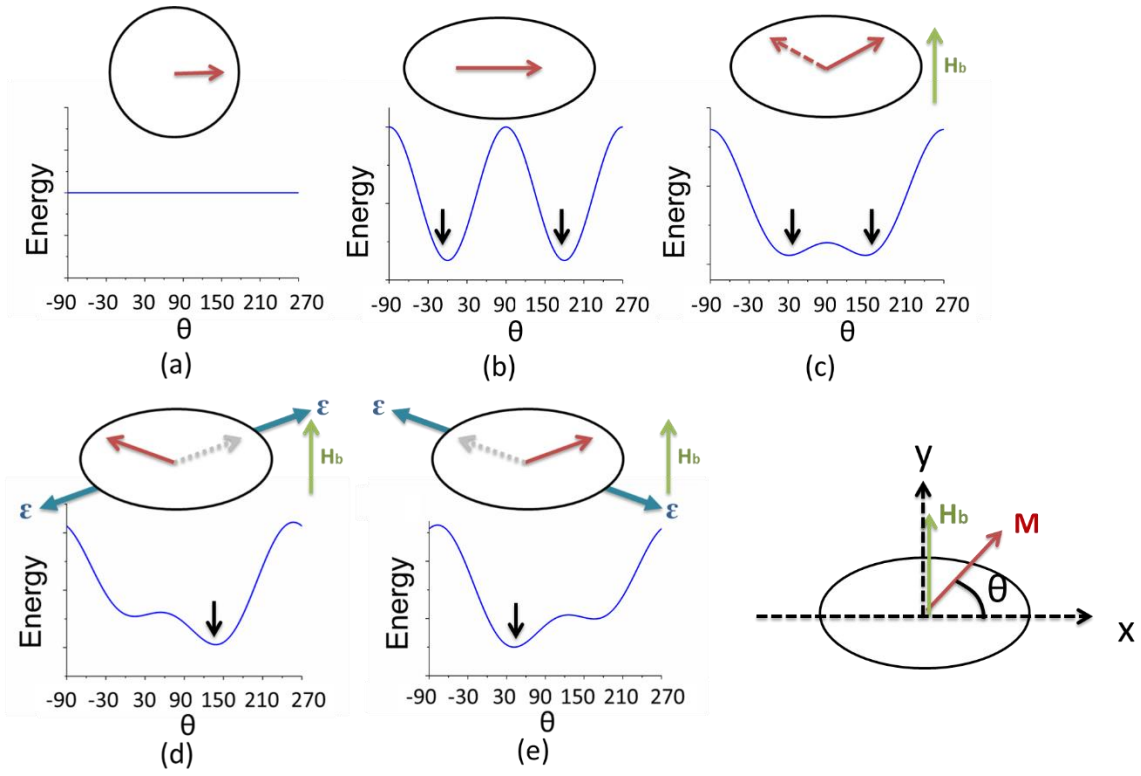

Figure 3.1: An energetic diagrammatic description of the proposed memory element. (a) Circular disk: Isotropic shape in-plane. (b) Elliptical disk: shape anisotropic induced easy direction along the major axis of the ellipse (0 or 180). (c) Bias field effect: two stable states are generated by a bias field H_b. Energy barrier between two states is lowered by bias field H_b. (d) and (e) Interaction of shape anisotropy, bias field, and applied tensile strain, changing the energy profile (+θ or –θ).

Figure 3.2 shows an illustration of the analytical model to demonstrate reorientation of a Ni magnetoelastic ellipse. The 500 nm PZT-5H thin film has a Pt bottom ground electrode deposited onto a 0.5mm thick Si substrate. The PZT-5H is represented with linear piezoelectric elements (i.e., subset of derived model) for this region. While not shown in Figure 3.2a, an exchange layer could be used between the Pt and Ni structures for applying the bias field in-situ (i.e. following the concept introduced in Figure 1d & 1e) [81]. Figure 3.2a shows the 150nm x 120 nm x 10 nm Ni ellipse surrounded by four 125 nm x 125 nm x 10 nm Au electrodes. The Ni

is represented with nonlinear magnetoelastic elements, while the Au is represented with linear mechanics elements (i.e. both subsets of the derived model). The two electrodes A-A are at a 45 degree angle, and the two electrodes B-B are at a 135 degree angle relative to the major axis of the ellipse (i.e. x-direction). The PZT-5H film is poled through the thickness in the z direction. The model presented in Figure 3.2 for the Ni ellipse, the electrodes, and the PZT-5H film thickness have not been optimized for a given objective function and are only presented to demonstrate the concept of single domain switching by 90 degrees on a thin film PZT mounted to a Si substrate. Rather than model the entire substrate, the interface of the PZT with the Pt/Si interface is clamped to prevent displacement. As shown in the cross-section of Figure 3.2b, the in-plane x-y dimensions have been reduced to 1000 x 1000 nm, and these boundaries along the x- and y-directions are also clamped to prevent displacements. In this model voltage is always applied to two top Au electrode sets (i.e. either A-A or B-B sets) with the bottom Pt electrode grounded; that is, the electric field is applied through the thickness of the PZT-5H. Figure 3.2c illustrates the deformation generated with the application of a voltage to produce a positive electric field. The d_{33} out-of-plane extension under the two sets of electrodes (e.g. A-A) generates an in-plane anisotropic tensile strain in the Ni nanodot, as illustrated with the dashed line. This local anisotropic strain switches the magnetic spin state of the Ni ellipse (or energy wells) between the two stable energy wells, as shown in Figure 3.1d and Figure 3.1e. The strain produced with this geometric configuration has been previously demonstrated on a bulk PZT sample, as described by Cui [79]. When the A-A electrodes are energized, the spins align along 45 degree direction; while if the B-B electrodes are energized, the spins align along 135 degree. Both angles represent stable equilibrium positions without a voltage/electric field applied.

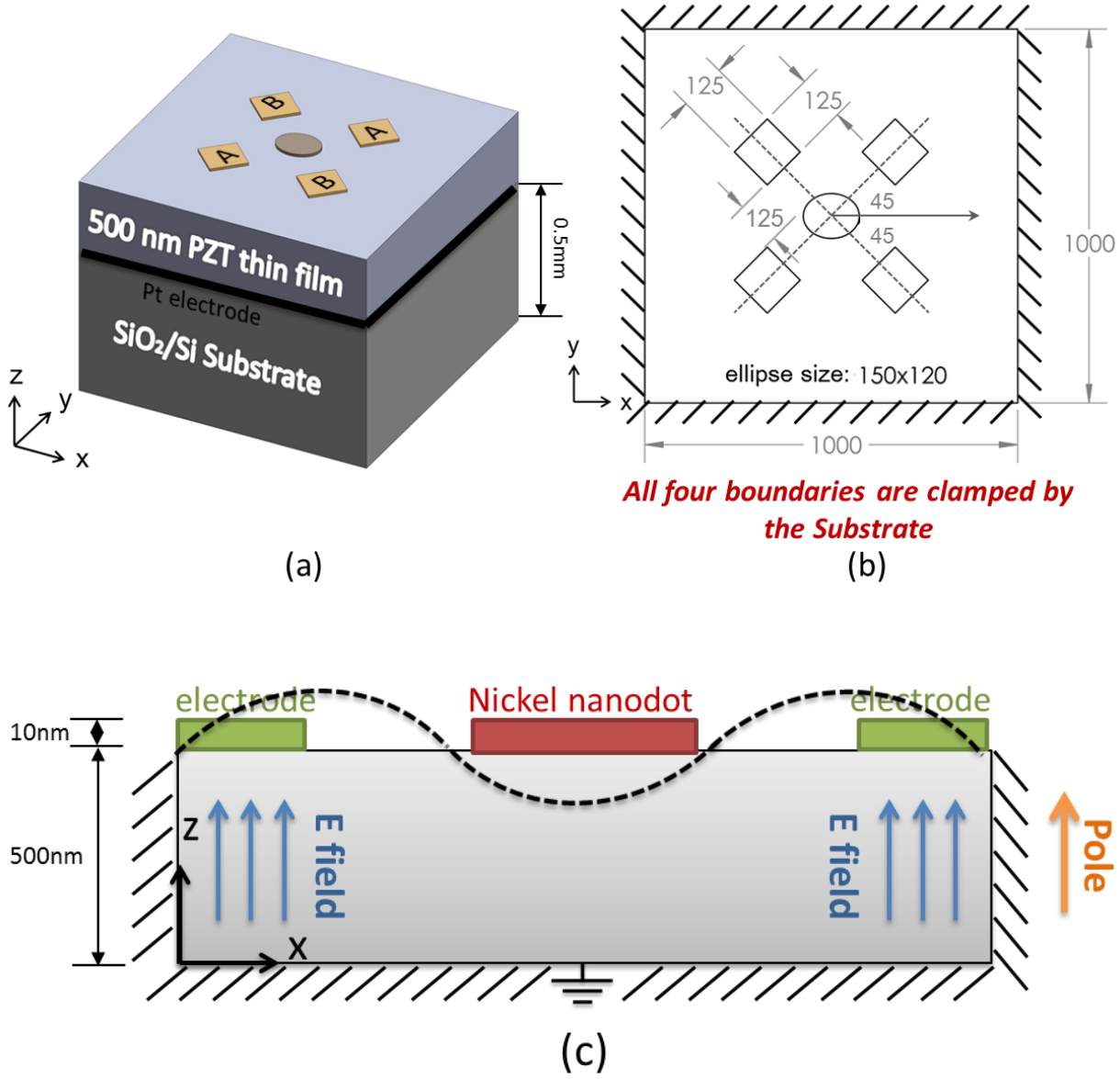

Figure 3.2: Schematic of the bi-stable memory bit. The memory bit consists of an elliptical ferromagnetic element deposited on a ferroelectric layer with patterned electrodes around the ferromagnetic element (a). Schematic of top view, showing all four boundaries of the PZT thin film clamped by the Si substrate (b). Cross-section view, showing mechanical response to applied electric field. By applying a positive voltage to the two electrode pairs (A-A), mechanical stretching is induced between the electrodes (c).

The finite element model for Figure 3.2a is constructed as follows. The nickel properties are $M_s = 4.8\times10^5 (A/m)$; $A_{ex} = 1.05\times10^{-11} (J/m)$; $\lambda_{100} = -46\times10^{-6}$, $\lambda_{111} = -24\times10^{-6}$, $c_{11} = 2.5\times10^{11} (N/m^2)$, $c_{12} = 1.6\times10^{11} (N/m^2)$, and $c_{44} = 1.18\times10^{11} (N/m^2)$ [4]. The magnetocrystalline anisotropy energy term is an order of magnitude smaller than the magnetoelastic energy (i.e. soft ferromagnetic material) and is assumed negligible. The Gilbert damping constant was set as $\alpha = 0.5$ to improve stability and process time. The PZT-5H material properties are $d_{33} = 5.93\times10^{-10} (C/N)$; $d_{31} = -2.74\times10^{-10} (C/N)$, $c_{11} = c_{22} = 1.27205\times10^{11} (Pa)$, $c_{12} = 8.02122\times10^{10} (Pa)$, $c_{13} = c_{23} = 8.46702\times10^{10} (Pa)$, $c_{33} = 1.17436\times10^{11} (Pa)$, $c_{44} = c_{55} = 2.29885\times10^{10} (Pa)$, and $\rho = 7500 (kg/m^3)$. The Young's modulus and Poisson's ratio for Au are $E^{Au} = 7\times10^{10} (N/m^2)$ and $\nu^{Au} = 0.44$, respectively. The exchange length, defined as $\sqrt{\frac{2A_{ex}}{\mu_0 M_s^2}}$, is 8.5 nm for nickel. The nickel nanoellipse is discretized using tetrahedral elements with a size on the order of nickel's exchange length. The remainder of the structure (i.e. PZT-5H thin film, Au electrodes) is discretized using tetrahedral elements with graded element sizes dependent upon local geometry. The voltage used during this study is -0.5 V applied as a step function for 6 x 10^{-11} s on either electrodes A-A or B-B (electrical field through the thickness is 1 MV/m). That is, a voltage is applied for a period of time sufficiently long to allow spin equilibrium to be obtained, and the voltage is then removed. All simulations include a magnetic bias field applied along the minor axis of the nano-ellipse. Prior to application of the bias magnetic field or voltage, all magnetic spins are uniformly canted out of the x-y plane at 45 degrees and allowed to precess toward an equilibrium state.

The first study determines the influence of magnitude bias field (Figure 3.1b-1c) on the location of the magnetic energy wells. In this study, the same boundary conditions as described above were used, but the applied voltage is zero. Figure 3.3 plots the magnetic energy well location (see insert for angle definition) as a function of applied bias magnetic field. Figure 3.3 also includes results from a Stoner-Wohlfarth model [60] with the finite element model. As the results show, as the magnetic field increases, the angle of the stable energy well increases and approaches 90 degrees. While the Stoner-Wohlfarth and the finite element model are in good agreement when determining the location of the energy wells, the Stoner-Wohlfarth model does a poor job of predicting the combined magnetic/elastic response of this structure. To approach the angle pictorially represented in Figure 3.1c, a constant bias field (H_b) of 9000 A/m is required to orient the magnetic energy wells at ~45 and ~135 degrees. This value can be achieved using an antiferromagnetic exchange coupling layer [81]. The following simulations incorporate an $H_{b=}$ 9000 A/m.

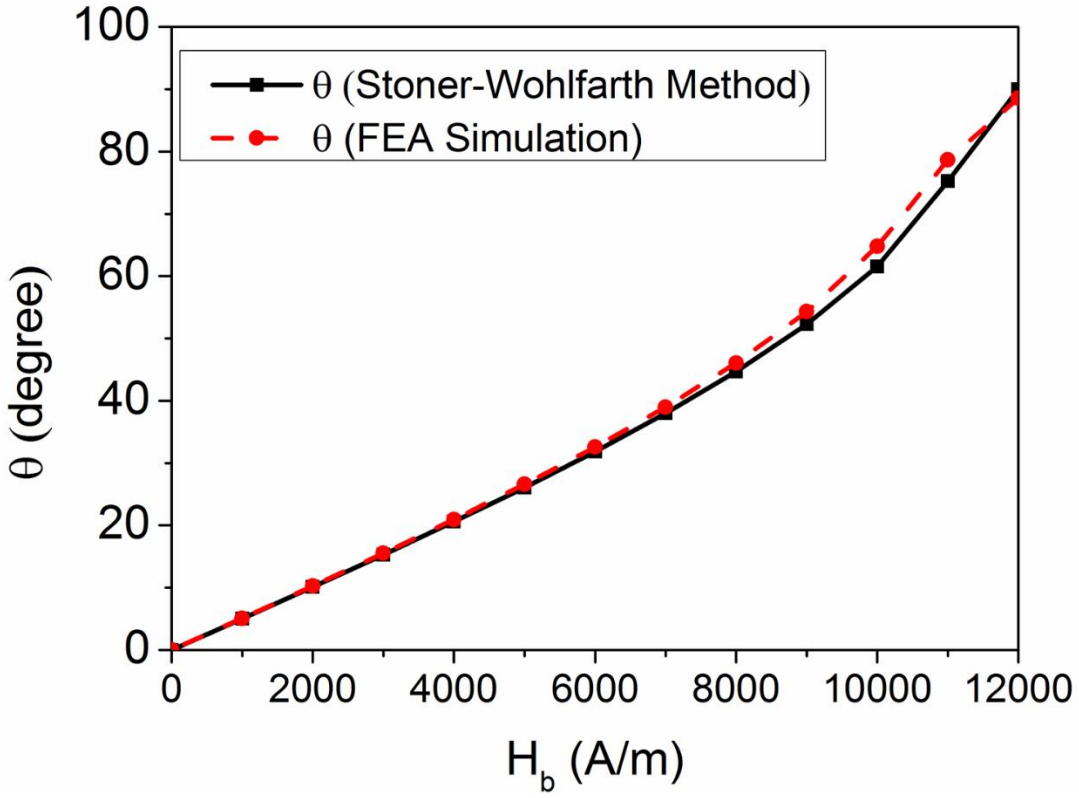

Figure 3.3: The angle of the energy minima and energy barrier, comparing values obtained from Stoner-Wohlfarth (SW) calculation and present FEA simulation work, as a function of applied bias field.

Figure 3.4 shows results for H_b= 9000 A/m and -0.5 V applied to the A-A electrode pair. In Figure 4a, a three-dimensional deformation plot along with relative strain contour plots ($\varepsilon'_{AA} - \varepsilon'_{BB}$) are presented. The terms ε'_{AA} and ε'_{BB} represent the normal strains along A-A and B-B axes, respectively. The contour plot indicates that the strain is limited to the region between electrodes A-A and does not significantly influence the surrounding region. Figure 4b provides a 2-D deformation plot along with relative strain contour plots for section A-A. The deformation is very similar to that presented in Figure 3.2c. That is, the PZT beneath the electrodes expands out-of-plane. This expansion, in turn, generates tensile strain in the center region along the A-A direction. The contour strain plot shows that the anisotropic strain ($\varepsilon'_{AA} - \varepsilon'_{BB}$) in the Ni nanoellipse is on the order of 450 με but is spatially distributed. To more closely examine the strain distribution, Figure 4c provides the anisotropic strain ($\varepsilon'_{AA} - \varepsilon'_{BB}$) as a function of position along the A-A direction (see insert). The five curves in the figure represent five different *z* locations through the thickness in the Ni nanoellipse. In general, the anisotropic strain decreases from the bottom (i.e. interface of PZT with Ni) to the top of the Ni nanoellipse. Also there is a significant reduction in strain near the edges of the Ni nanoellipse, *x* = 40 nm and 175 nm due to the shear lag effect. Shear lag effects become important and must be taken into account as the thickness of the magnetic layer increases relative to the minor axis dimension. At the top of the Ni (t = 10 nm), the strain near the edge (axis = 40nm and 175nm) is about 100 με, while the relative strain at the center (axis=100nm) is about 400 με. At the bottom of the Ni (t = 2 nm), the strain near the edge (*x* = 40nm and 175nm) is about 300 με while the relative strain at the center (*x* = 100nm) is about 500 με, which shows that the strain decreases through the thickness. The average strain transferred to the nanoellipse is approximately 450 με, representing a ~60%

decrease in strain magnitude compared to material near the electrodes (~1000με). The strain also decreases significantly in the Ni nanoellipse between two neighbors.

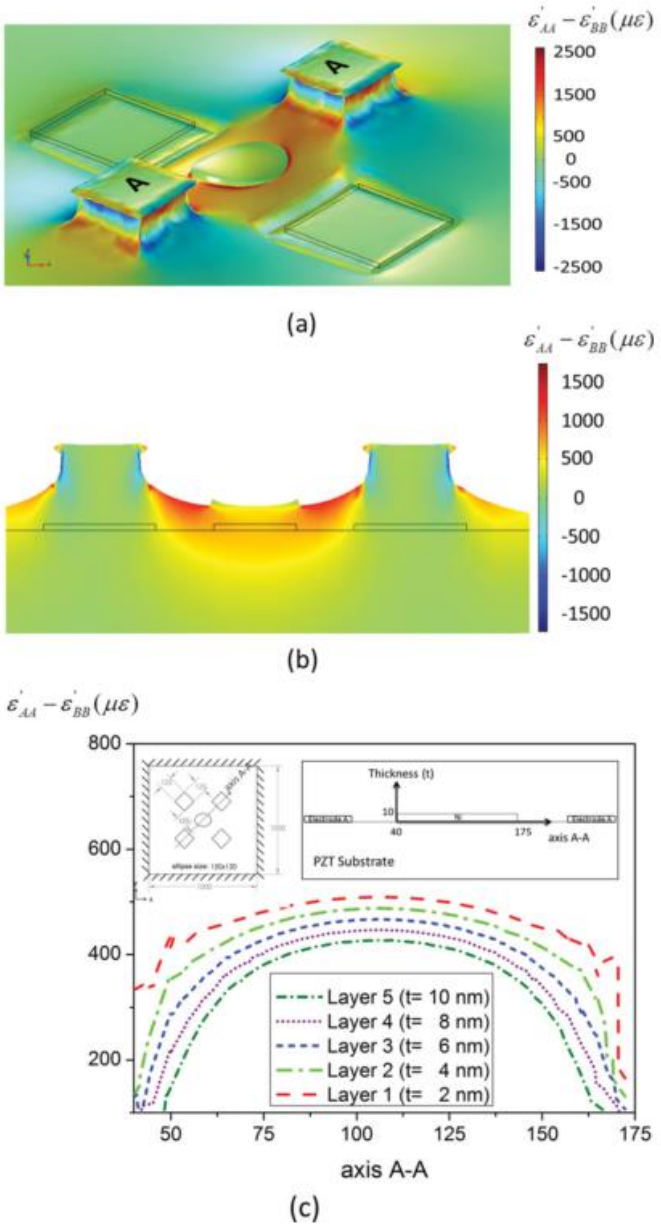

Figure 3.4: Simulation results (displacement scale exaggerated). (a) Voltage applied on A-A electrode pair. Two electrodes expand out-of-plane and tensile strain is induced in the middle region. (b) Cross-section 2D plot along A-A. Tensile strain is induced in the middle (~800 με). The strain transferred to the nano-ellipse is ~450 με. Non-uniform strain

distribution exists between the substrate and the nano-ellipse. (c) Strain for different layers in the nanoellipse along A-A.

Figure 3.5 shows the magnetic response of the structure when either electrodes A-A (Figure 3.5a) or B-B (Figure 3.5b) are energized. The magnetization is initially in an equilibrium state at ~45 degrees with respect to the x-axis. Electrodes A-A are initially energized as shown in Figure 3.5a. The top figure shows the voltage applied and the magnetic dipole orientations in the Ni nanoellipse after equilibrium is reached. The larger arrow on the Ni nanoellipse is used to inform the reader of the magnetic spin states of each element. The bottom Figure 3.5a shows an exaggerated in-plane (x-y plane) deformation plot along with a relative strain contour plot ($\varepsilon'_{AA} - \varepsilon'_{BB}$). The deformation plot in this figure illustrates the stretching of the ellipse along the A-A direction that is consistent with the results shown in Figure 3.4. This stretching causes the magnetic spins in a negative magnetic material like Ni to rotate toward the stable equilibrium position located at ~135 degrees (see figure 1d and 1e) as shown in Figure 3.5a. When the voltage is removed (not shown), the magnetic spins are stable at ~135 degree and do not return to ~45 degrees. Following this voltage loading sequence, electrodes B-B are energized with results shown in Figure 5b. As can be seen in the bottom of Figure 3.5b, the displacement of the Ni nanoellipse is now along the B-B axis rather than along the A-A axis as shown in Figure 3.5a. This stretching of the ellipse along B-B causes the magnetic spins to reorient along the A-A axis as shown in Figure 3.5b top with the large red arrow. Once the voltage is removed, the magnetic spins remain along the B-B axis since this is a stable equilibrium position (see Figure 3.1d).

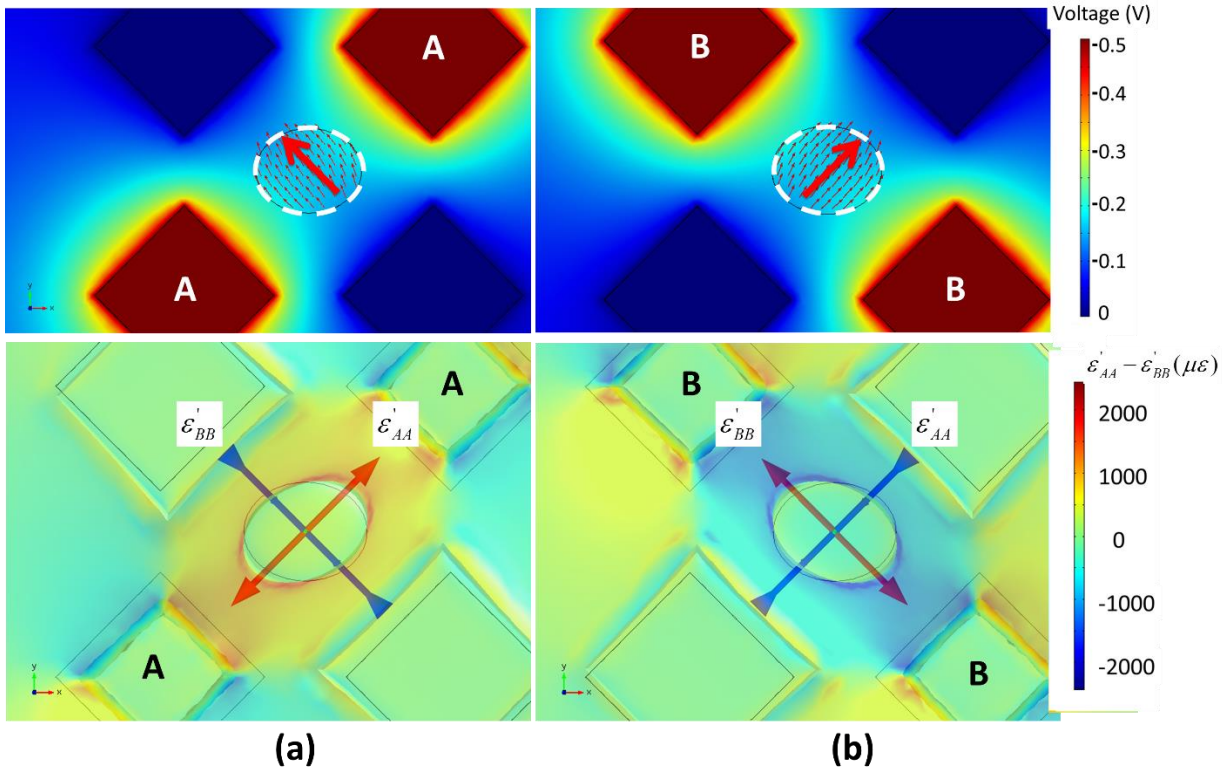

Figure 3.5: Top view of strain intensity plot from the fully-coupled simulation results. Magnetization rotates due to the application of strain from electrode pair (A-A) (top). Applied voltage on A-A creating 45-degree tensile principle strain (bottom). Magnetization rotates due to the application of strain from electrode pair (B-B) (top). Applied voltage to B-B creating 135-degree tensile principle strain (bottom).

Figure 3.6 shows magnetization and voltage applied as a function of time for the case presented in Figure 3.5. The blue dashed line is the voltage applied to A-A, the green dashed line is the voltage applied to B-B and the red line is the average magnetization state. The left vertical axis corresponds to the magnetization direction (i.e. angle measured from x-axis) while the right vertical axis represents voltage. Initially the stable magnetic equilibrium is at ~45 degree when a voltage is applied to A-A at time = 1.5 ns and held until 3.5 ns. The magnetization responds at approximately 2 ns and switches from 45 to ~135 at 3ns. The magnetization response time is approximately 1.5 ns. When the voltage (A-A) is removed, the magnetization remains in this new state, since it represents a stable equilibrium well. When the second pair (B-B) is energized at 4.5 ns, the magnetization rotates back to ~45 degrees, and remains there following removal of the voltage to B-B. The electrical energy required to "write" (switch) this magnetic single domain can be calculated from the surface charge on the electrodes and the applied voltage. For the mechanism shown in Figures 5 and 6, the switching energy is approximately 80 fJ. This energy is associated with deformation of the PZT, strain in the electrodes, and strain in the Ni structure. This value is considered a conservative value, given that the structure has not been optimized with respect to PZT thickness or electrode size.

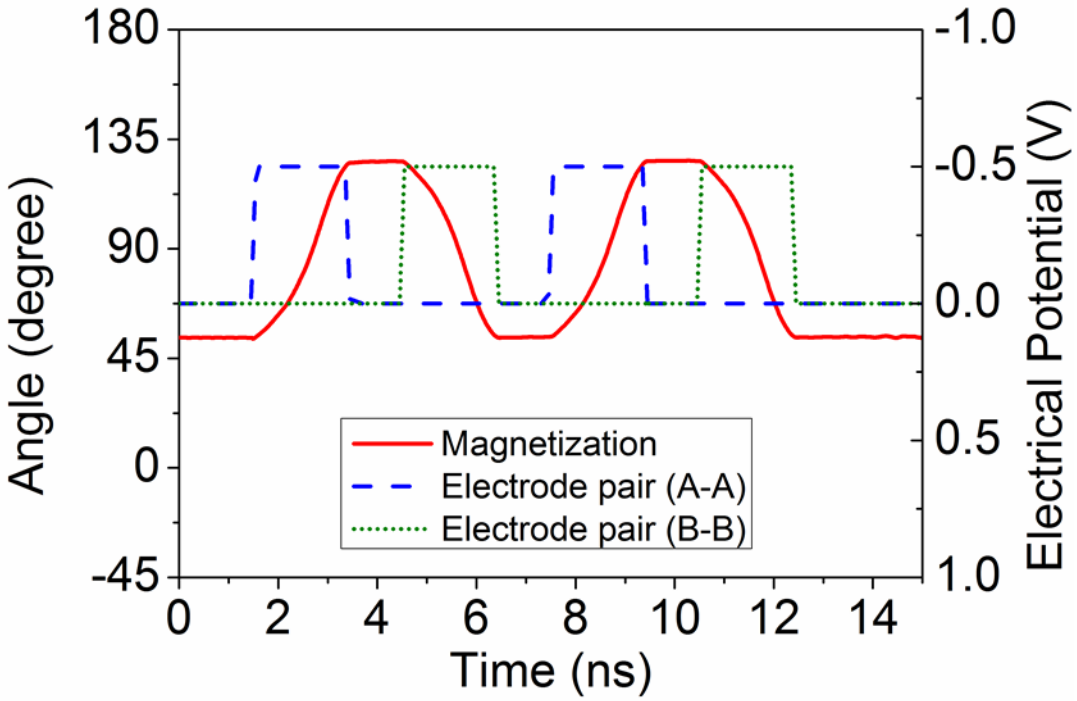

Figure 3.6: Time response of the memory bit. The magnetization starts at zero and voltage is applied to electrode pair A-A, switching M to the "1" state; voltage on B-B switches M to the "0" state. The magnetization is bi-stable. The dashed blue line represents voltage applied to A-A; the dash green line represents voltage applied to B-B; and the red line represents the response of the magnetization.

3.4 Conclusion

This work presented a robust analytical model combining micromagnetics with elastodynamics and electrostatics to solve a strain-mediated composite multiferroic problem. The solution was implemented in a finite element code providing both spatial and temporal information on the magnetic, electric, and mechanical fields. The problem of a single magnetic domain structure attached to a clamped piezoelectric thin film was studied. Analytical results demonstrate that out-of-plane deformations produce sufficient strainto reorient the magnetic structure, overcoming the classical substrate clamping problem. Work remains to be conducted on other magnetoelastic materials and optimizing the various structural geometries to minimize the required electrical energy to reorient or write this domain structure [82].

4. Interactions of Dipole Coupling Effects and Applied Strain

Nanomagnetic logic devices are more energy-efficient than conventional CMOS if they are clocked in an energy-efficient manner, such as with electrically generated strain. This work demonstrates the clocking of nanomagnetic logic in dipole-coupled circular magnetostrictive nanomagnets using strain, which is generated by applying an electrostatic potential to an underlying piezoelectric substrate. Normally, elliptical magnets with two stable orientations are used for nanomagnetic logic, but the use of circular magnets presents two distinct advantages. Firstly, stress anisotropy energy does not have to exceed a large shape anisotropy energy and that reduces the clocking voltage and energy dissipation. Secondly, this paradigm is potentially scalable to magnets of ~20 nm lateral dimension that would become superparamagnetic at room temperature, yet strain induced anisotropy could drive it to a ferromagnetic state in which its magnetization orientation is dependent on that of the neighboring magnet due to dipole coupling. This could lead to a new genre of nanomagnetic logic scalable to very small dimensions, thus eliminate nanomagnetic logic's major shortcoming of scalability.

4.1 Introduction and Background

Today's state-of-the-art charge-based computing technology is faced with major challenges, such as leakage current, standby power dissipation, and relatively low energy-efficiency. During the past decade, nanomagnet based computing devices have been studied as an alternative to charge-based computing devices [83]–[87]. The main advantage of using a single domain nanomagnet encoding the Boolean logic state in its magnetization orientation for computing is the extremely low energy dissipation in the nanomagnet during switching due to its correlated spin dynamics [88]. Despite the low internal energy dissipation for switching, the development of nanomagnetic logic devices has been stymied by the large energy dissipation due to I^2R losses in the clocking circuit when these devices are clocked with a current generated magnetic field or spin transfer torque [28][89][90][91].

In order to realize ultra-low power nanomagnetic clocking, "hybrid spintronics-straintronics," or clocking nanomagnets with strain in 2 phase multiferroics comprising an elastically coupled magnetostrictive and piezoelectric layer, has been proposed and theoretically modeled [28][90][91]. In addition, use of strain to control the magnetic state of magnetostrictive materials has been explored experimentally, though not at the nanoscale [71][72][76][92][93]. Recently, experimental demonstration of strain based clocking of elliptical nanomagnets has been reported [94]. Other energy efficient ways of clocking nanomagnets using Spin Hall Effect and Spin Orbit Torque have also been reported [95][96].

However, in these studies, the nanomagnets are designed to be ferromagnetic and possess high shape anisotropy energy barriers [$\Delta U \geq 50\ k_B T$, were k_B is the Boltzmann constant and T is the room temperature in Kelvin] for two reasons. Firstly, the shape anisotropy results in only two

stable magnetization orientations that encode the binary logic bits '0' and '1.' Secondly, the high barrier prevents the magnetization from randomly flipping between the two stable states in the presence of thermal noise (the probability of spontaneous flipping is ~ $e^{-\Delta U/k_B T}$). This latter requirement could potentially limit the scalability of such devices to lateral dimensions of ~50 nm, since ΔU is proportional to the magnet's volume.

On the other hand, there are studies where the superparamagnetic limit in nanomagnets has been controlled; nanomagnets with very small volume that are normally superparamagnetic at room temperature have been rendered ferromagnetic by introducing strong anisotropy using shape or exchange bias [13][97]. In addition, it was recently demonstrated that nickel nanoparticles can be switched between a superparamagnetic state and a single domain ferromagnetic state at room temperature by application of a biaxial strain that changes the stress anisotropy [31].

Thus, it appears that switching circular nanomagnets at the superparamagnetic limit to a ferromagnetic state by clocking it with strain in a phased manner may provide a path to the ultimate scaling of nanomagnetic devices to implement Boolean operation and propagate logic at the scale of ~20 nm nanomagnets. This work theoretically simulates the Boolean NOT operation and logic propagation in *circular* nanomagnets (with no intrinsic shape-anisotropy) whose lateral dimension is ~ 50 nm. Strain (not shape anisotropy) makes the magnetization orientation bistable and not only allows the encoding of binary bits in the two stable states, but also enables clocking and information processing. We also experimentally demonstrate evidence of logic propagation in circular nanomagnets of ~100 nm diameter. The diameter is chosen to be much larger than 20 nm due to our lithographic limitations. While these nanomagnets may not strictly be at the

superparamagnetic limit, the magnetization has no preferred orientation (in the absence of stress) and will rotate coherently under thermal noise that tends to randomize its orientation. When uniaxial stress is applied to these circular nanomagnets, the magnetization has a preferred (easy axis) orientation. Thus the modeling discussed in this work and the experimental results presented are, to a first approximation, expandable down to dimensions ~20 nm.

4.2 Magnetization dynamics in a dipole-coupled nanomagnet with stochastic LLG

Magnetization dynamics of multiferroic dipole-coupled nanomagnets shown in Figure 4.1 can be simulated in the presence of thermal noise by the stochastic LLG equation [98]–[100]. We model the magnetostrictive nanomagnets as Terfenol-D ($M_S = 800(\frac{kA}{m})$), and Gilbert damping coefficient [61], $\alpha = 0.1$, the magnetostriction, $3/2\lambda_s = 900$ ppm. We assume that for the geometric dimensions for which we perform the simulation (circular cross section with diameter, $\mathrm{D} = 50$ nm and thickness, $\mathrm{t} = 20$ nm), the magnetization $\vec{M}$ in the nanomagnet is spatially uniform and the nanomagnet behaves as a single domain magnet [101] due to the large exchange coupling penalty in forming multiple domains. The magnetization dynamics of such a nanomagnet under the influence of an effective field, $\vec{H}_{eff}$ is described by the stochastic Landau-Lifshitz-Gilbert (LLG) equation [100]:

$$\frac{d\vec{M}(t)}{dt} = -\gamma\vec{M}(t)\times\vec{H}_{eff}(t) - \frac{\alpha\gamma}{M_s}\left[\vec{M}(t)\times\left(\vec{M}(t)\times\vec{H}_{eff}(t)\right)\right] \tag{1}$$

Here, $\vec{H}_{eff}^{\,i}$ $\vec{H}_{eff}$ is the effective magnetic field on the nanomagnet and γ is the gyromagnetic ratio. The effective field $\vec{H}_{eff}^{\,i}$ is:

$$\vec{H}_{eff}^{\,i}(t) = -\frac{1}{\mu_0\Omega}\frac{\partial U_i(t)}{\partial\vec{M}_i(t)} = -\frac{1}{\mu_0 M_s\Omega}\nabla_{\vec{m}}U_i(t) + H_{thermal}(t) \tag{2}$$

where Ω is the volume of the nanomagnet and $U_i(t)$ is its total potential energy at the instant of time *t*.

In an array of dipole-coupled closely spaced circular nanomagnets in the x-y plane, the total energy of each nanomagnet can be defined as:

$$U_i(t) = \sum_{\substack{i \neq j \\ i=j-1 \text{ to } j+1}} E^{i-j}_{dipole-dipole}(t) + \Omega \left(\frac{M_S^2 \mu_o}{2}\right) \left[N_{d-xx} m^2_{x_i}(t) + N_{d-yy} m^2_{y_i}(t) + N_{d-zz} m^2_{z_i}(t)\right] - \Omega \left(\frac{3}{2} \lambda_S \sigma_i(t)\right) m^2_{y_i}(t) \quad (3)$$

where N_{d_kk} is the demagnetization factor in the k^{th} direction. The reduced magnetization can be defined as:

$$\vec{m} = \frac{\vec{M}}{M_S};\ m_x^2 + m_y^2 + m_z^2 = 1 \quad (4)$$

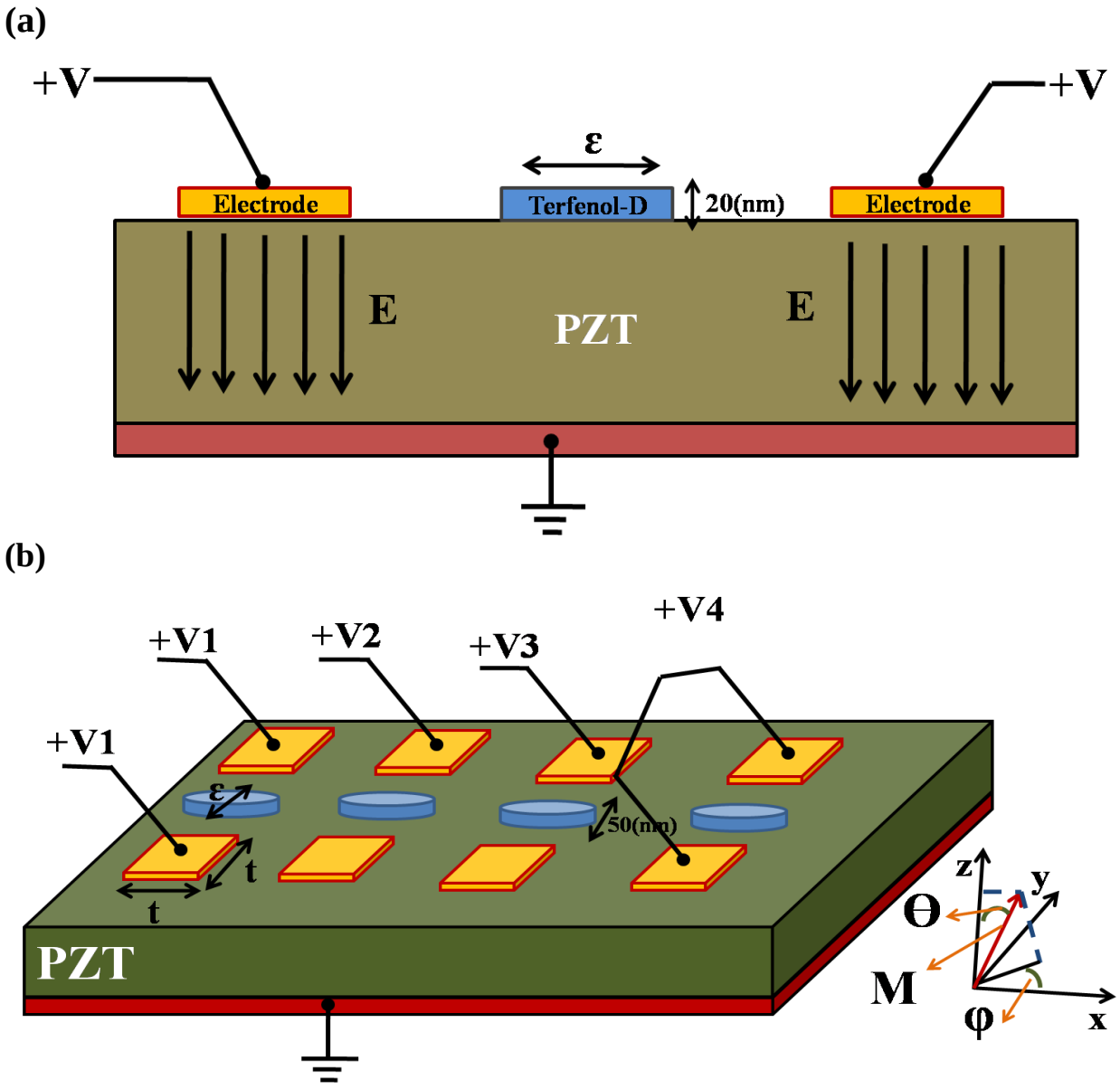

Figure 4.1: (a) A multiferroic circular nanomagnet with diameter of 50(nm) and thickness of 20(nm). (b) Chain of dipole coupled nanomagnets with separation of center to center equal to "d" that can be clocked sequentially using a local clocking scheme.

In equation (3), the first term represents the dipole-dipole energy ($E_{dipole\text{-}dipole}$) between nearest neighbor magnets. The second term, $E_{shape\text{-}anisotropy}$, denotes the shape anisotropy energy due to the circular cylinder shape (although $N_{d\_xx}=N_{d\_yy}$ because the magnets have circular cross-section, N_{d_zz} is different and the magnetization dynamics is significantly affected by out-of-plane excursions of the magnetization).The third term represents stress anisotropy energy caused by the stress σ that is developed in the magnetostrictive layer when strain is transferred to it from the piezoelectric layer. The piezoelectric layer is strained by applying an electrostatic potential across its thickness.

The effect of thermal fluctuation is modeled with a random field ($\vec{H}_{thermal}$) with statistical properties incorporated into the effective field ($\vec{H}_{eff}^{i}$) [102][103]. The quantity $\vec{H}_{thermal}$ is modeled as:

$$\vec{H}_{thermal}(t)=\sqrt{\frac{2K_B T\alpha}{\mu_0 M_s \gamma \Omega \Delta t}}(\vec{G}(t)) \tag{5}$$

where $\vec{G}(t)$ is a Gaussian random distribution with mean of 0 and variance of 1 in each Cartesian coordinate axis; $\Delta t = 1(ps)$ is the time step used in simulating the switching trajectories and it is inversely proportional to the attempt frequency with which thermal noise disrupts magnetization.

Calculating Demagnetization Factors:

The demagnetization factors N_{d-kk} for the circular cylinder nanomagnet used in this simulation in the x, y and z direction are denoted by N_{xx}, N_{yy} and N_{zz} . In general,

$$N_{xx} + N_{yy} + N_{zz} = 1 \quad (6)$$

and specifically for the cylindrical geometry (circular dots):

$$N_x = N_y \quad (7)$$

If the length of the cylinder is $2l$ and radius is a, the demagnetizing factor in the z direction can be expressed as [104]:

$$N_z = 1 - 2lL_s/(\mu_0 \pi a^2) \quad (8)$$

L_s is the self-inductance which can be calculated using the following equation:

$$L_s = \frac{2\mu_0}{3l^2}[\sqrt{a^2 + l^2}\{l^2 F(k_s) + (a^2 - l^2)E(k_s)\} - a^3] \quad (9)$$

where $F(k_s)$ and $E(k_s)$ are the complete elliptical integrals of the first and second kind with k_s defined as:

$$k_s = \frac{a^2}{a^2 + l^2} \quad (10)$$

4.3 Experimental Results and Discussion

In this section, we examine why dipole coupling alone does not suffice for transferring information in a chain of cylindrical nanomagnets with circular cross-section, how sequential stress application remedies the situation and achieves reliable information propagation, the manner in which the chain relaxes to the ground state upon stress withdrawal, and analyze the reliability of information transfer in such a system in the presence of thermal noise. We note that in this section the dimensions of all circular nanomagnets are consistently taken to be: diameter, $D = 50$ nm, thickness, $t = 20$ nm and pitch (center to center distance between two neighboring magnets, p = 150 nm).

Consider information transfer in a chain of dipole coupled circular nanomagnets as shown in Figure 4.2a at room temperature, with the stiff elliptical magnet at the left corner representing an input bit at the beginning of the chain. Under the dipole influence of this input bit pointing "up", the magnetization of the next circular magnet tends to point down. However, there is another competing effect: due to the dipole coupling, circular magnets prefer to collectively orient their magnetizations horizontally (along the axis of the chain of nanomagnets).Thus, as one moves along the chain, the antiparallel orientation ("up", "down", "up", "down"…) is lost and the magnetizations tend to point more to the right or left. Figure 4.2b, Figure 4.2c, and Figure 4.2d show the in-plane magnetization distribution of the second, third and fourth nanomagnet respectively in the presence of thermal noise. Figure 4.2e shows the in-plane magnetization of magnets versus time, which again demonstrates the same physics. The magnetization of the first nanomagnet oscillates (due to thermal fluctuations) around $\phi = 90^o$ while that of the second oscillates around $\phi = \sim -30^o$ (not -90^o), the third oscillates around $\phi =$

~10^{o} (not 90^{o}), and the fourth around ϕ = ~0. Thus, all information is lost before traversing the third or fourth magnet.

(a)

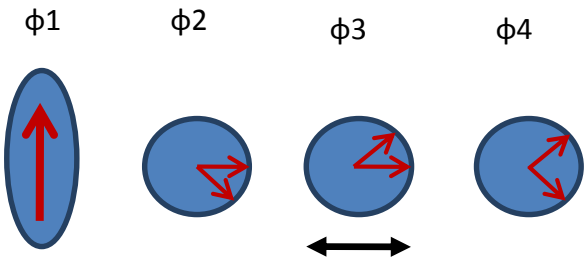

d=50(nm), pitch =150 nm
t=20(nm)

(b)

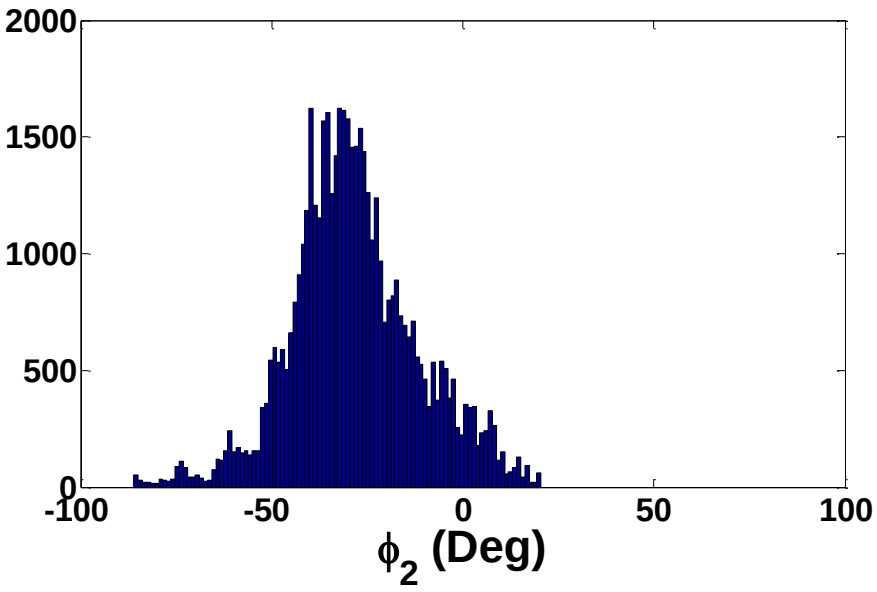

(c)

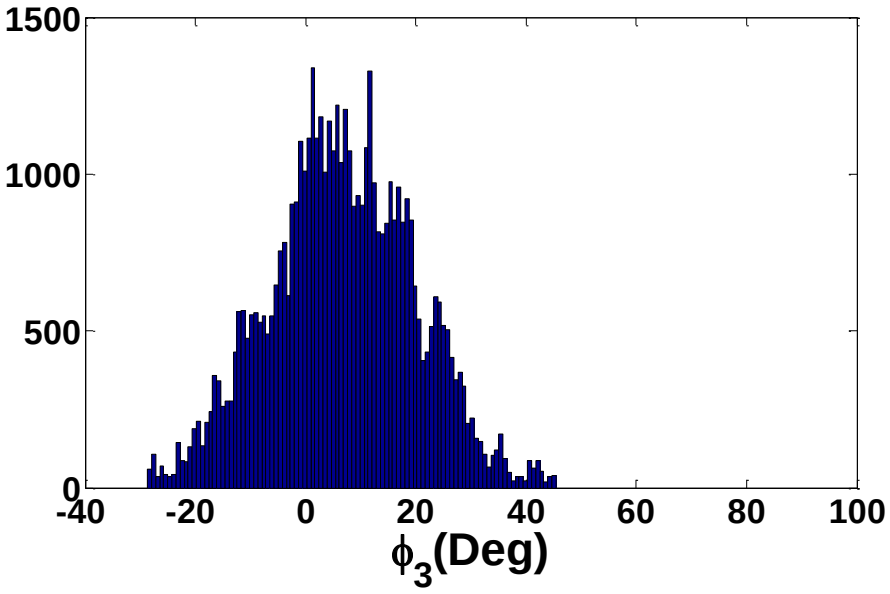
1500
1000
500
0
-40
-20
0
20
40
60
80
100
ϕ_3(Deg)

(d)

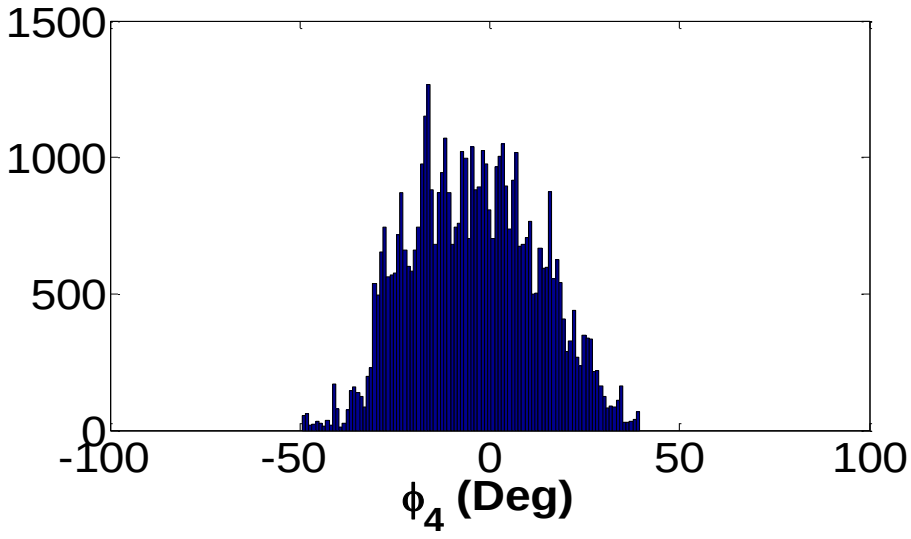
1500
1000
500
0
-100
-50
0
50
100
ϕ_4 (Deg)

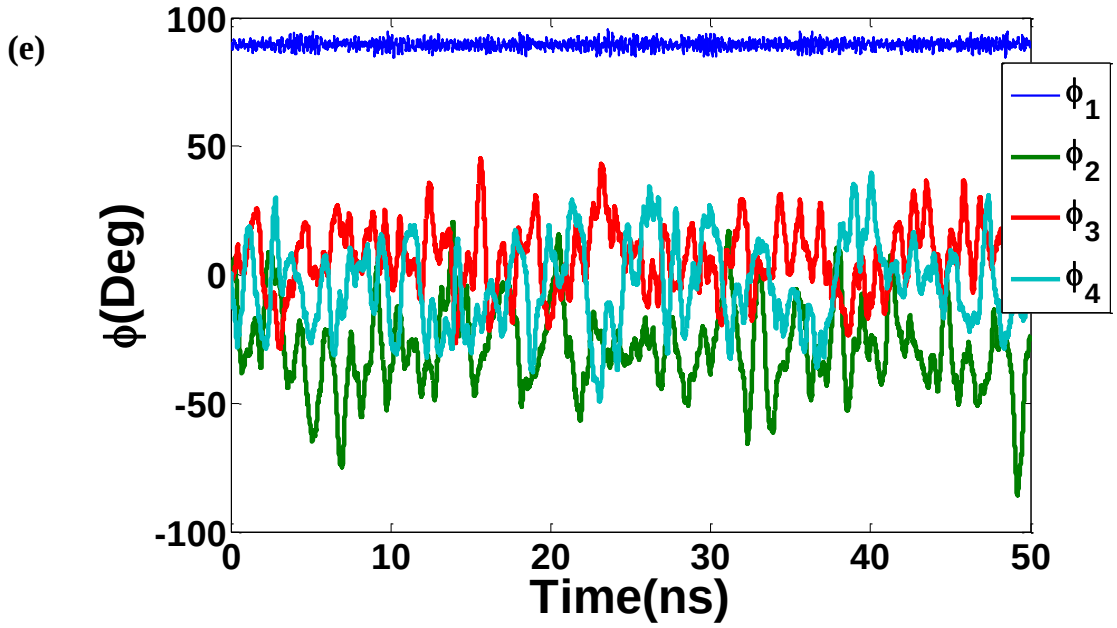

Figure 4.2: (a) Schematic view of dipole coupled nanomagnets with high shape anisotropy input, (b) in-plane magnetization distribution for second magnet under influence of dipole coupling from the first (hard or highly anisotropic) nanomagnet. (c) in-plane magnetization distribution of third magnet under influence of the second and forth magnets. (d) in-plane magnetization distribution of fourth. (e) Fluctuation of nanomagnet's in-plane magnetization orientation in the presence of thermal noise vs time.

In this section, simulations are performed to show that by applying mechanical stress sequentially to the nanomagnets, we can successfully transfer information. This is shown in Figure 4.3. Suppose a stress is applied to the first nanomagnet and simultaneously a specific bit is written so the first nanomagnet points "up". We note that stress alone cannot deterministically switch the first magnet to the "up" or "down", especially when applied along a single axis. Thus, the input bit should have additional spin-torque to break the symmetry, or a dipole coupling to an elliptical magnet whose state can be deterministically written by stress applied sequentially along multiple axes [105][106].

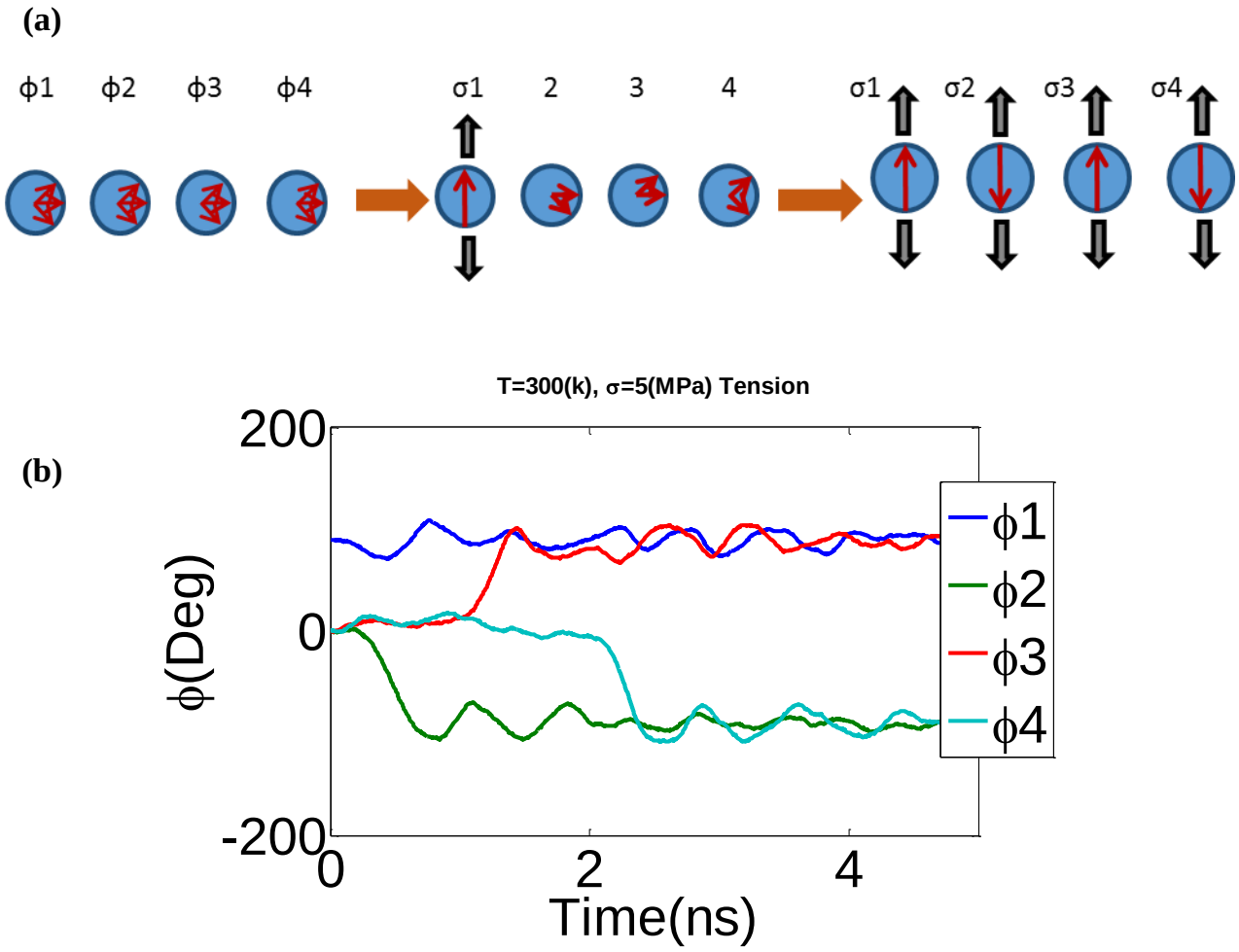

Figure 4.3: (a) Diagram showing clocking of the circular nanomagnets with tensile mechanical stress. (b) In-plane magnetization dynamics of dipole coupled nanomagnets versus time, showing that stress promotes "logic restoration" or near "up" or near "down" orientation.

We also note that for a material with positive magnetostriction (Terfenol-D simulated here), applying a tensile/compressive stress favors a magnetization alignment along/perpendicular to the direction of stress respectively. It is the opposite for materials with negative magnetostriction (for example Ni or Co used in the experiments in section 4). Thus, applying a tensile stress perpendicular to the axis of the circular chain of nanomagnets introduces a stress anisotropy that lowers the energy of the "up" and "down" states. When the stress anisotropy is sufficiently strong, an antiparallel orientation of magnetizations in the "up" and down" states is energetically more favorable than the magnetizations pointing horizontally and parallel to each other. Hence, it is seen that applying stress to the nanomagnets in a sequential manner ensures that the information encoded in the magnetic state of the first magnet is propagated in a unidirectional manner in the subsequent anti-parallel orientations of the magnetizations in the nanomagnetic chain. In this case the magnetizations of the nanomagnets 2, 3 and 4 rotate to -90^{o}, $+90^{o}$ and -90^{o} orientations and oscillates (due to thermal fluctuations) around these states. Thus, information is correctly propagated along the chain of nanomagnets.

i. Relaxing to ground state after stress withdrawal

It is also important to ensure that once the stress in withdrawn, the magnetizations of all the nanomagnets in the chain relax to the ground state where they are oriented horizontally and parallel to each other. Figure 4.4 shows that this is indeed the case and the magnetizations relax to the ground state within ~1 ns of withdrawal of stress.

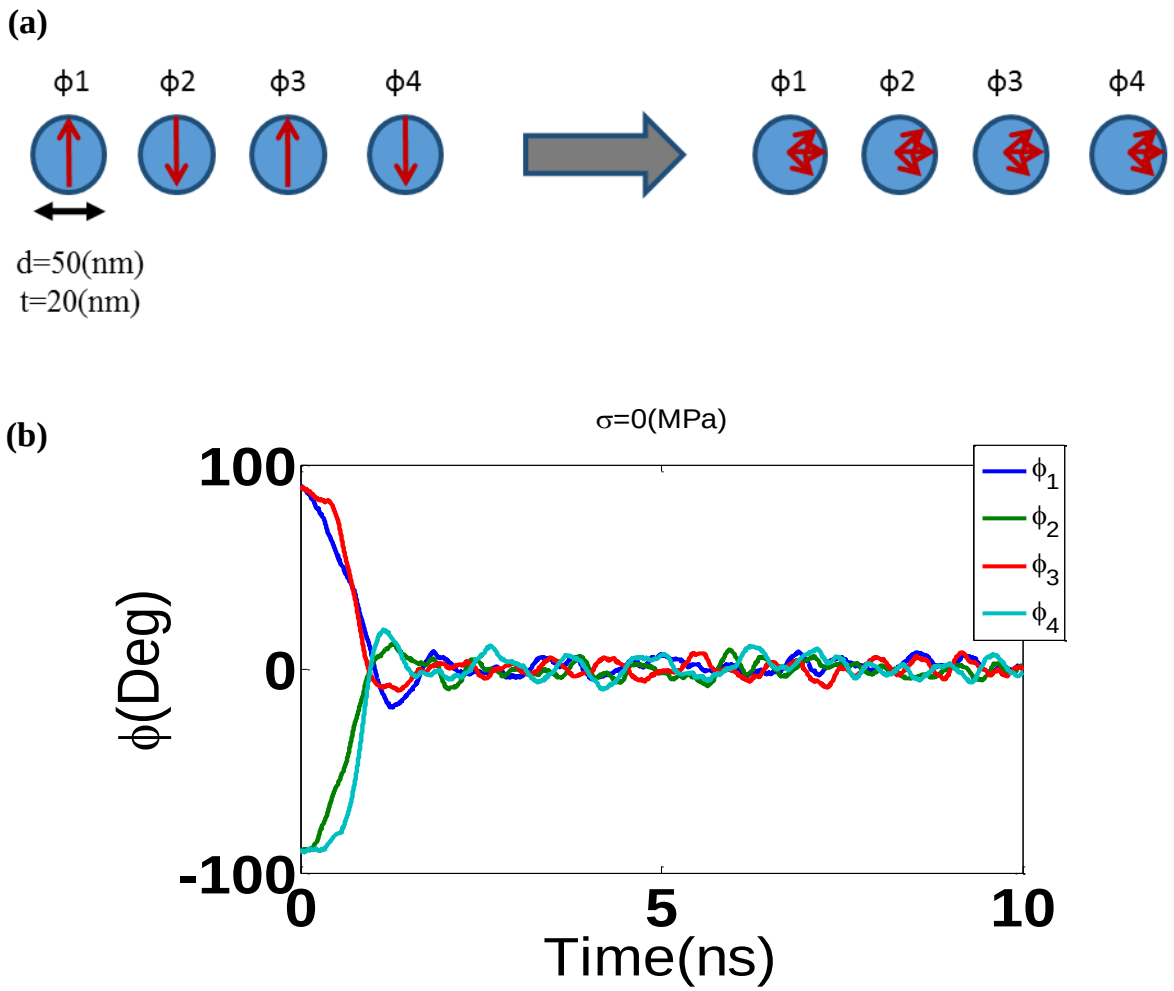

Figure 4.4: (a) When stress is withdrawn, the magnetizations return to their initial distribution. (b) Time history of anti-parallel to parallel transition of the magnetization orientation, upon stress withdrawal.

An important concern in nanomagnetic computing is the reliability with which information can be propagated in a chain of nanomagnets. Therefore, we run a large number of simulations (100,000 times) for each design and count the number of times there are errors in information propagation. Thus, errors due to thermal noise are simulated but other potential issues such a pinning of magnetization by defects or alignment issues are discarded in this first order analysis. The switching error in circular Terfenol-D nanomagnets (diameter $\mathrm{D} = 50$ nm, thickness $\mathrm{t} = 20$ nm) are specifically studied for two conditions:

1. Varying pitch (center-center distance) but constant tension stress ~ 15 (MPa) shown in Figure 4.5a
2. Varying stress while keeping pitch = 80 (nm) constant as shown in Figure 4.5b

It is found that when pitch $< 100(nm)$[which is feasible as edge-edge separation < 50 nm is achievable with lithography] and stress > 8 MPa, there is not a single switching failure in 100,000 simulations of the switching trajectories at room temperature. Further, for the case of stress of 8(MPa) and pitch=80(nm), the number of simulation is increased to 10^6 times and still no error was observed. Therefore, the error probability in the latter case is less than 10^{-6}.

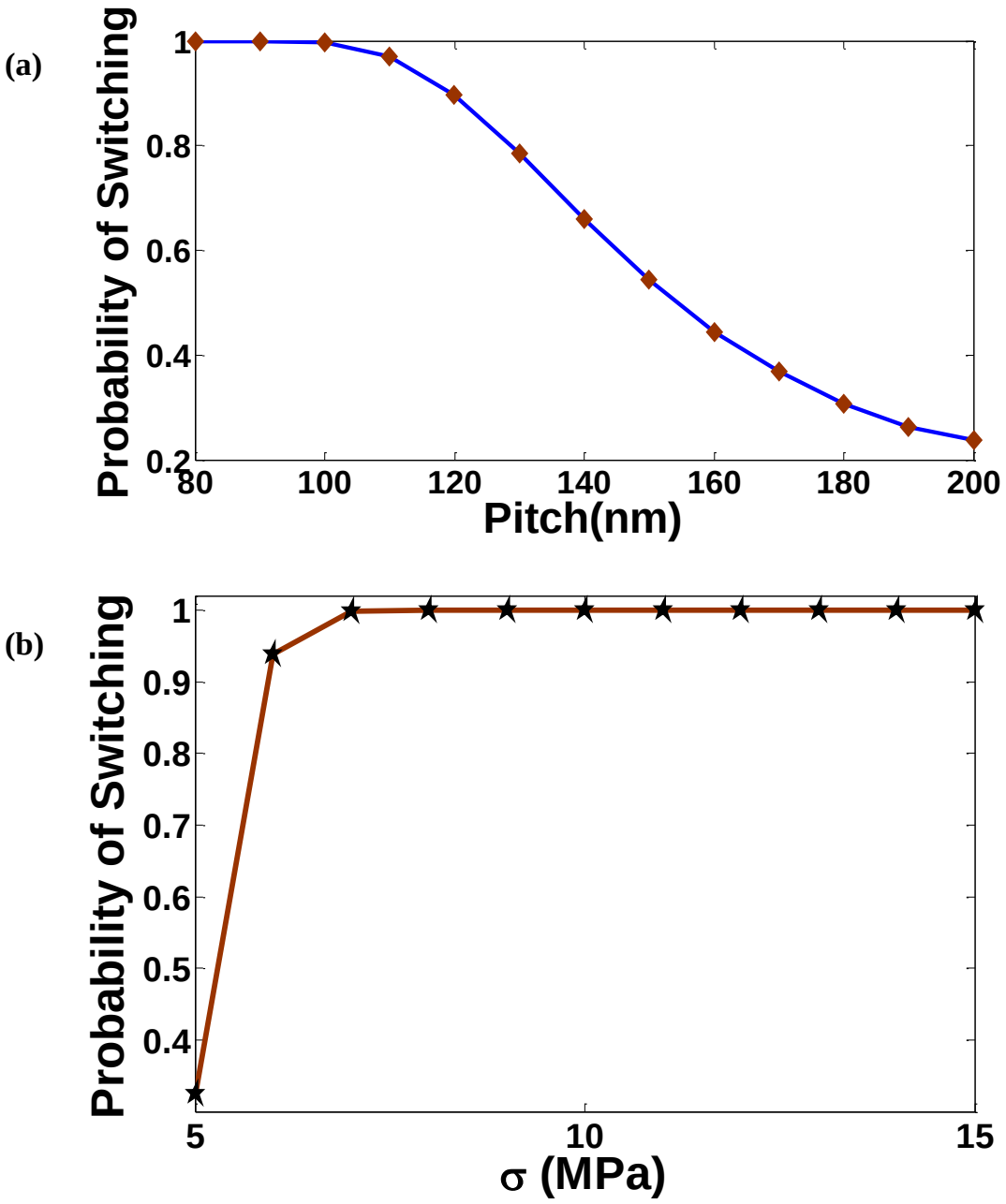

Figure 4.5: (a) Probability of switching in circular nanomagnets for different dipole coupling. (b) Analysis of switching error for different stress levels.

4.4 Experimental demonstration of clocking circular nanomagnets with strain

In this section, fabrication techniques and experimental data are presented to verify the analytical predictions for voltage control of nanomagnet dipole interactions. The experiment uses a piezoelectric substrate PMN-PT to modify the magnetic anisotropy in individual Ni nanostructures through the magnetoelastic effect. The voltage induced magnetic anisotropy changes the dipole-dipole interaction of adjacent Ni nanostructures and thus the potential to control the propagation of information. This experiment builds on the original work of Cowburn in 2002 whose focus was exclusively on magnetic dipole interactions in chains of nanomagnets [107] as contrasted with the focus of the present research on voltage manipulation of dipole interactions in chains of nanomagnets.

The tests relied on evaluating the response of two separate nanoscale pattern configurations to demonstrate voltage control of adjacent single domain structures, as illustrated in Figure 4.6. The first pattern configuration (top of Figure 4.6) consists of an elliptical disk adjacent to a circular disk. The second pattern configuration (bottom of Figure 4.6) consists of an elliptical disk adjacent to a chain of 3 circular disks. For all nanoscale elements the magnetoelastic material is 12 nm thick Ni. The elliptical disks have dimensions of 135 nm by 75 nm (long dimension along the y-direction), and all the circular disks are 100 nm in diameter. These particular dimensions for the elliptical and circular disks produce single domain nanoscale structures. The spacing between the ellipse and the circular disks or between adjacent circular disks is 50 nm. This spacing provides sufficient dipole-dipole interaction between the adjacent elements and also allows fabrication of the elements. As illustrated in Figure 4.6, each of the two pattern configurations is fabricated as an array of either configuration 1 or configuration 2. Within each

array, the pattern configurations are separated by either 0.5 μm in both x- and y-directions for configuration 1, or 1 μm in the x-direction and 0.5 μm in the y-direction for configuration 2 to prevent dipole-dipole interactions between adjacent pattern configurations. The arrays are required for measurement purposes, i.e. sufficient magnetic signal is required to collect magnetization data in detector.

The fabrication details for the two array nanostructures are as follows. An un-poled 1 cm^2 square 0.5 mm thick piece of single-crystal (011) $Pb(Mg_{1/3}Nb_{2/3})O_3]_{(1-x)}$-$[PbTiO_3]_x$ (x = 0.32, TRS Technologies, Inc., USA), or PMN-PT, is the substrate. The PMN-PT [100] in-plane crystallographic axis is aligned with the sample's y-direction while the [011] in-plane crystallographic axis is aligned with the x-direction (shown in Figure 4.6).

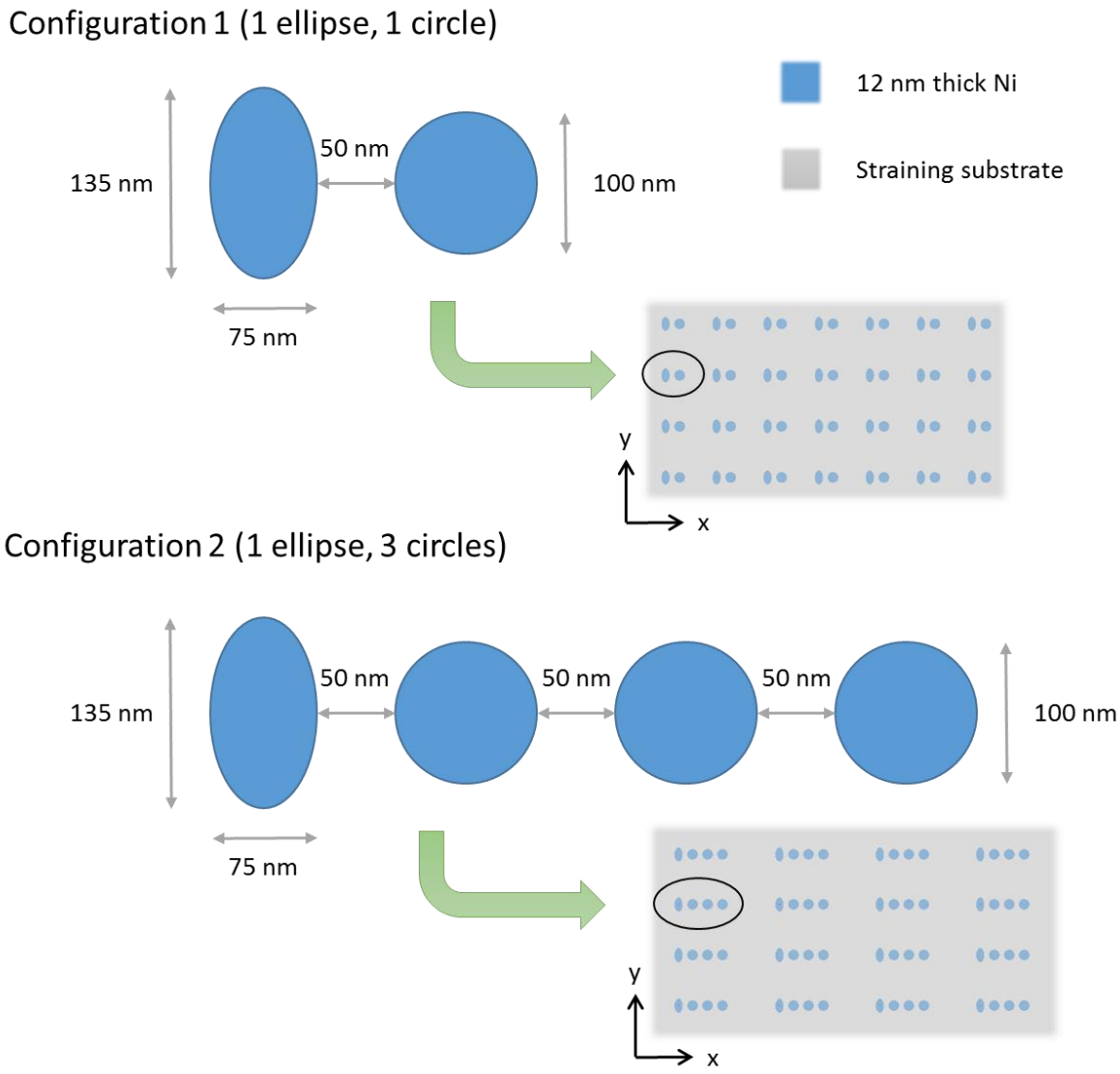

Figure 4.6: Diagrams of nanostructure patterns in configuration 1 (top pattern) and configuration 2 (bottom pattern). Each repeated pattern is copied 1 micron away from each other in a rectangular pattern (2 microns horizontally for the longer chains of configuration 2), to prevent any dipole-dipole interactions. Configuration 1 is vertically antiparallel due to dipole interaction and shape anisotropy, and configuration 2 still prefers x-axis ferromagnetic alignment. The straining substrate is 500 micron thick PMN-PT with a 50 nm Pt top electrode and a 50 nm Au bottom electrode. The x-direction lies along the PMN-PT's [011] crystallographic axis, and the y-direction lies along the [100] crystallographic axis.

Planar electrodes are deposited on the top and bottom surfaces of the PMN-PT substrate, i.e. 50 nm Pt and 50 nm Au films with 5 nm Ti adhesion layer. On the top PMN-PT surface, the two configuration arrays are patterned using a double layer of polymethylmethacrylate resist (PMMA 950K A2) and liftoff-assisting copolymer (EL6 MMA). Electron beam writing was performed using a charge dose of 700 C/cm2. The resist pattern was developed using a solution of 1:3 MIBK to IPA (methyl isobutyl ketone and isopropyl alcohol, respectively). Prior to depositing the Ni nanostructures, the PMN-PT was poled with a 0.8 MV/m electric field. After poling the substrate, 5 nm Ti followed by 12 nm Ni (adhesion and ferromagnetic layers) was deposited by e-beam evaporation. This was followed by 12 hours of room-temperature lift-off using n-methyl-2-pyrrolidone (NMP) solvent. Figure 4.7 shows SEM images of the 2 configurations on the pre-poled PMN-PT substrate.

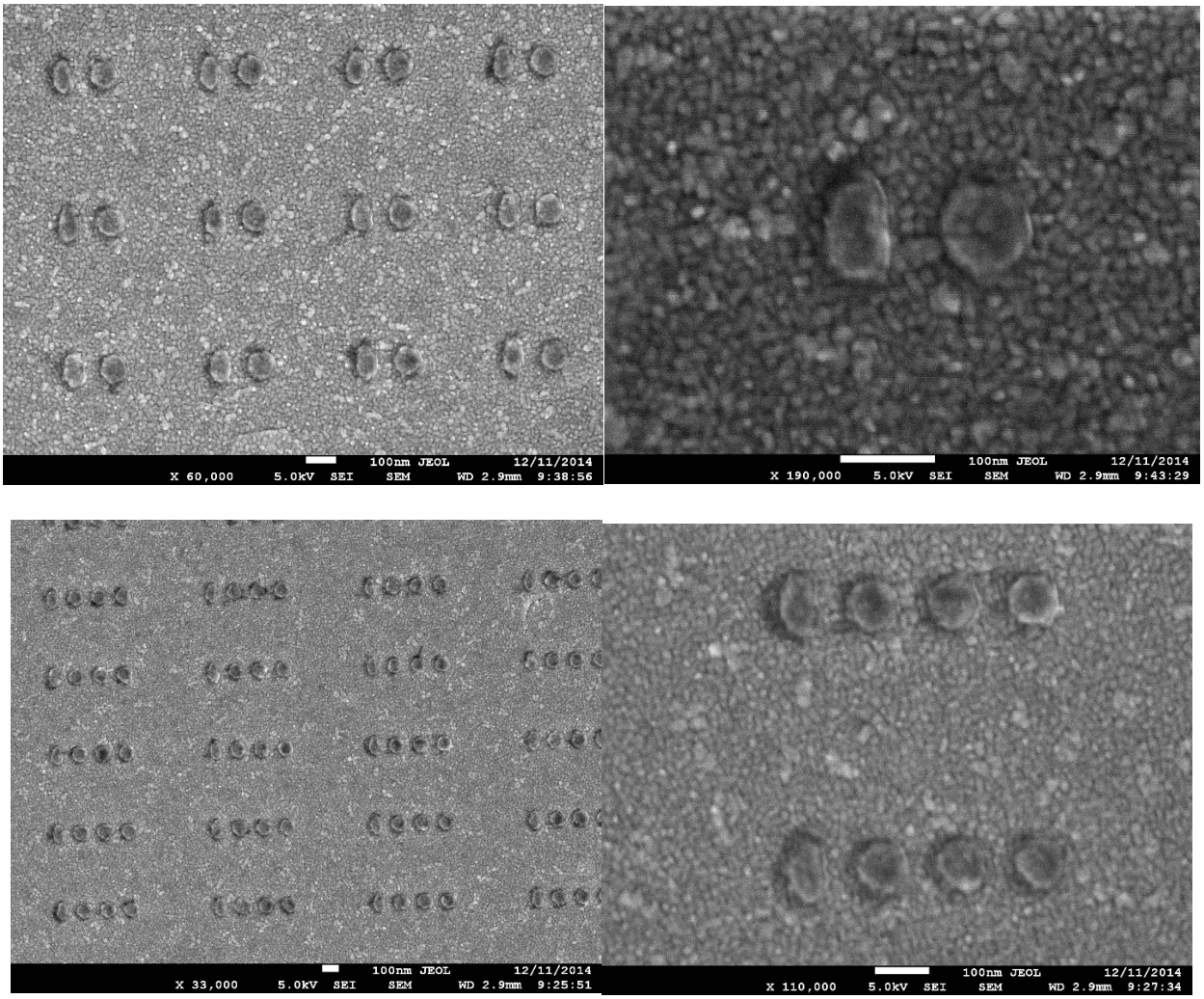

Figure 4.7: SEM micrographs of 12 nm thick nanomagnets, with 5 nm Ti adhesion layer, in configuration 1 (top) and configuration 2 (bottom). Both arrays were patterned on the same 50 nm Pt top electrode film on the PMN-PT substrate, with 50 nm backside Au electrode film. Both electrodes are bonded to the PMN-PT substrate with 5 nm of Ti.

Magnetization curves along the x-direction were measured using a magneto-optic Kerr effect (MOKE) magnetometer in the longitudinal mode (magnetization vector is parallel to both the reflection surface and the plane of incidence). The samples with either configuration 1 or configuration 2 were positioned in the test setup and M-H hysteresis curves were measured without an electric field applied. For each set of M-H hysteresis data, 50 individual runs were averaged where the magnetic field was swept from +500 Oe to -500 Oe, and then back to +500 Oe. Following this baseline measurement, the M-H hysteresis curves were repeated with a 0.8 MV/m electric field applied to the PMN-PT substrate. For this electric field, the PMN-PT produces a strain of -3000 με along the x axis and a strain of +1000 με along the y axis [22].

4.5 Experimental Results and Discussion

This section first discusses the experimental MOKE results for both configuration 1 and configuration 2 separately, while addressing the influence of electric field on each configuration's magnetic response. This is then followed by contrasting the results from the two configurations to demonstrate strong experimental support for the main modeling results in Fig 3. Throughout this analysis, it is important to note that Ni is negatively magnetostrictive, and the PMN-PT under electric field creates a compressive strain in the y-direction and a tensile strain in the x-direction (i.e. applied electric field creates y-direction magnetic anisotropy in the nanomagnets, particularly so in the circles).

We first begin by analyzing only Figure 4.8a, which shows the MOKE results for arrays of configuration 1's nanomagnet pattern (1 ellipse and 1 circle). For the zero electric field case (i.e.unstrained), the magnetic remanence is ~0.5 and the coercive field is ~35 Oe. For this measurement configuration, the expected remanance should approach zero for a perfect geometry at 0 Kelvin (top left of Figure 4.9). The remanence should be zero because the ellipse's magnetizations should point in the y-direction due to shape anisotropy and the circular disks magnetization should point in the opposite y-direction of the ellipse due to dipole interaction. However, the presence of thermal noise and geometric imperfections produces thermal fluxation as well as moderate pinning sites which yields a measured ~0.5 remanence shown in Figure 4.8a. With the application of a 0.8 MV/m electric field to the sample, the remanance is reduced to ~0.25, while the coercive field changes negligibly. This reduction of magnetic remanence with an electric field is expected because the added strain anisotropy (compressive along the y-direction and tensile along the x-direction) increases the preference of magnetization in the circles to lie along

the y-direction, which together with dipole interaction with the initial elliptical nanomagnet, produces antiparallel alignment. The negligible coercivity change suggests that the same non-ideal influences present in the unstrained case are still present in the strained case, so the remanance for the unstrained state is already at its minimum value, matching the ideal shown in Figure 4.9. This validating match is critical for the main conclusion of this work that comes from comparing both configurations together, which is clearly defined after the following exposition of configuration 2's MOKE data.

Next we analyze only Figure 4.8b, which shows the MOKE results for arrays of configuration 2's nanomagnet pattern (1 ellipse and 3 circles). For the zero electric field case (i.e. unstrained), magnetic remanence was at ~0.75, while the coercive field is slightly larger at ~40 Oe. The reason the magnetic remanance for configuration 2's pattern is larger than configuration 1's pattern is due to the preference of magnetization in a longer chain of circular nanomagnets to lie along the chain via dipole interactions. The application of a 0.8 MV/m electric field reduces the magnetic anisotropy to ~0.4, and coercive field falls to ~35 Oe. This change in remanence is expected because the added strain anisotropy allows the amplification of the initial ellipse's y-direction dipole influence. In other words, small magnetization deviations from the x-direction in the unstrained circles translate to highly preferred new magnetization directions that are nearly perpendicular to the x-direction. Therefore, for configuration 2 we see that the application of stress anisotropy changed the predominantly horizontal magnetic easy axis to an aniparallel state. Now equipped with an understanding of both configurations 1 and 2 in both strained and unstrained cases, we can fully analyze the differences in the results to show how they together support the modeled nanomagnet behavior in Figure 4.3.

(a)

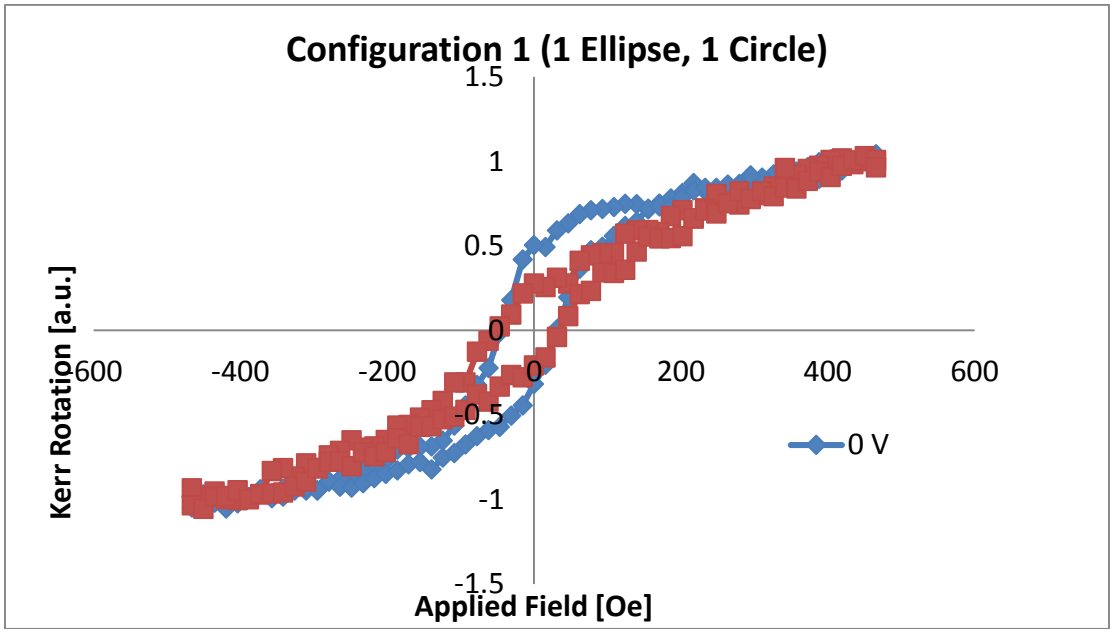

(b)

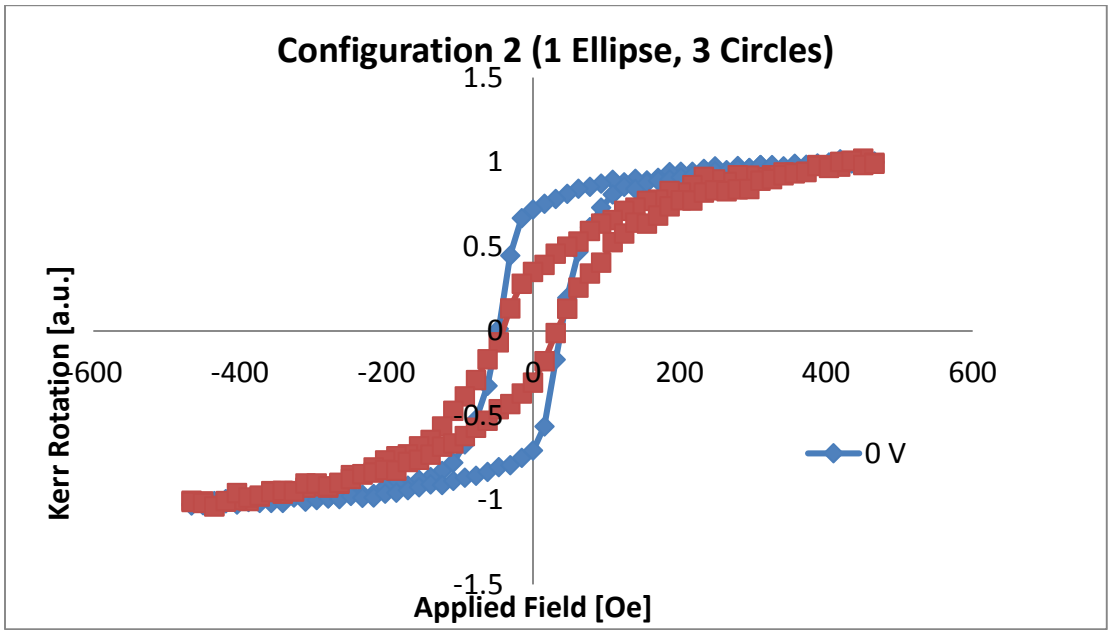

Figure 4.8: Longitudinal MOKE results for arrays of configuration 1 (top) and configuration 2 (bottom), in both unstrained (no electric field) and strained (0.8 MV/m electric field) states. The sweeping magnetic field is applied along the sample's x-direction shown in Fig 6 and Fig 7. Each loop shown is the representative average of 50 data sets.

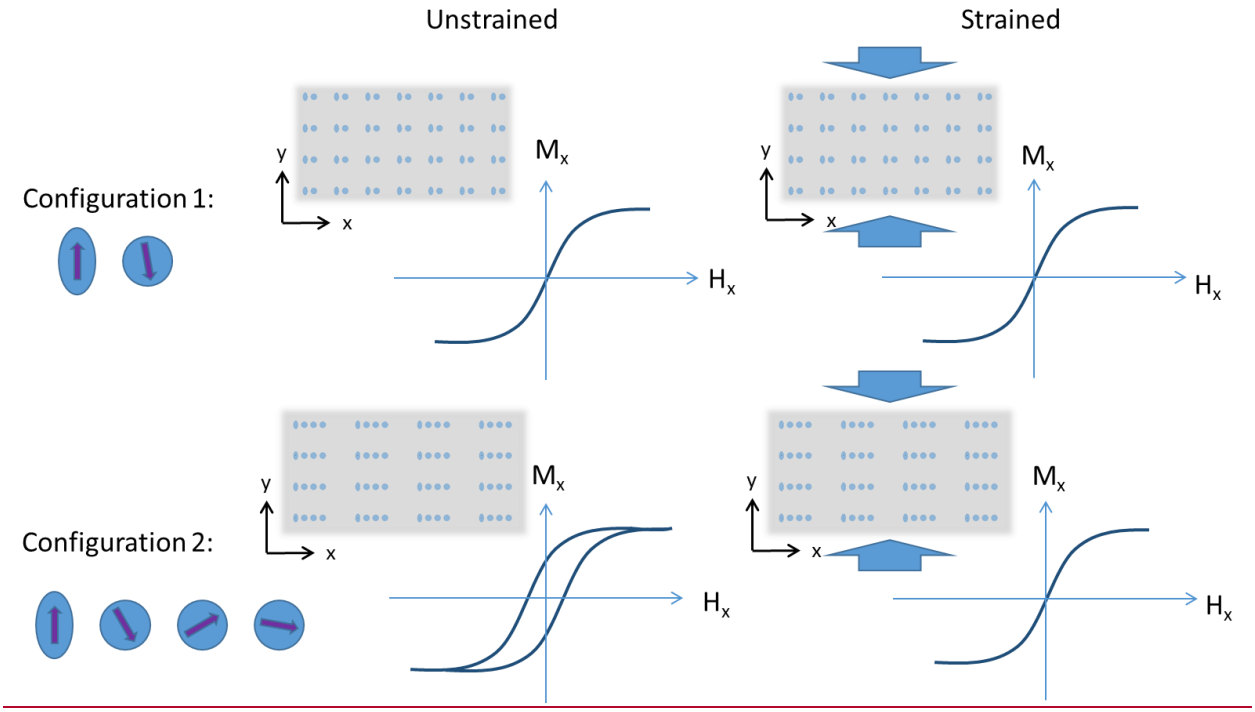

Figure 4.9: Diagrams of ideal strained negatively magnetostrictive Ni nanomagnet behavior (perfect geometry, no thermal noise) in configuration 1 (top pattern) and configuration 2 (bottom pattern). In the unstrained state, configuration 1 is vertically antiparallel due to dipole interaction and shape anisotropy, and configuration 2 still prefers x-axis ferromagnetic alignment. In the strained state, configuration 1 continues to be vertically antiparallel, and configuration 2 now also prefers vertically antiparallel due to the initial ellipse's propagating dipole influence and added strain anisotropy.

Comparing and contrasting the results of Figure 4.8a with that of Figure 4.8b, one finds the following features. There is a difference in remanence between configurations 1 and 2 in the unstrained state (~0.5 and ~0.75, respectively), indicating that dipole coupling induced antiparallel alignment between the elliptical magnet and the immediate circular magnet did indeed occur. However, as the chains length increases (i.e. from configuration 1 to configuration 2) the dipole-dipole interaction decreases, yielding a larger magnetic remanence. This makes intuitive sense because in configuration 1, the single circular disk is dipole coupled to its neighboring magnetically hard ellipse, while in configuration 2 the first circle is the only disk strongly dipole coupled to the magnetically hard ellipse while the second circle and remaining circles dipole coupling reduces as the number of circular disks increases. The experiment also shows the unstrained case of configuration 2 (remanence of ~0.75) has a much strong preference for x-direction magnetic alignment than unstrained configuration 1 (remanence of ~0.5). Furthermore, the MOKE data for strained configuration 2 is shown to be very similar to that of configuration 1; coercive field is also at ~35 Oe, and the remanence of ~0.4 is in fact lower than that of unstrained configuration 1 (~0.5). Therefore, this experimental data demonstrates strong support for the modeled nanomagnetic behavior, i.e. the application of strain anisotropy perpendicular to a nanomagnet chain with only one initial nanomagnet having fixed magnetization creates antiparallel magnetization alignment in all following nanomagnets.

4.6 Conclusion

To summarize, we have experimentally demonstrated that a chain of circular nanomagnets can be used to propagate binary information and employ simulations to show that the error can potentially be reduced less than 10^{-6} by sequentially clocking the nanomagnets with stress. More importantly, this paradigm uses circular nanomagnets in which anisotropy is induced with strain and is potentially scalable to dots ~20 nm that would become superparamagnetic; yet strain induced anisotropy could drive it to a ferromagnetic state in which its magnetization orientation is dependent on that of the neighboring magnet. Thus, this could provide a path to the ultimate scaling of nanomagnetic devices to implement Boolean operation and propagate logic at lateral dimensions of ~20 nm.

5. Strain-Mediated Control of Spontaneous Exchange Bias

Here we demonstrate electric-field modification of spontaneous exchange bias in a Ni-NiO thin film system coupled to a piezoelectric substrate, where exchange bias is induced with only an initial magnetic field. Magnetization measured during the application of an electric field revealed asymmetric shifting of the left and right coercive field values, along with shifting of the overall hysteresis loop. The novel behavior arising from the application of an electrically controlled strain can be explained through the canting states of unstable spins in the NiO AFM film at the AFM-FM interface. We believe this is the first example of a system where an electric field can be used to modify spontaneous exchange bias.

5.1 Introduction and Background

The control of nanoscale magnetic phenomena is an area of intense interest [1]. One phenomenon generating high research activity in recent years is exchange bias, which refers to magnetic anisotropy in coupled antiferromagnetic – ferromagnetic (AFM-FM) systems. This coupling originates from interactions of AFM and FM spins at the AFM-FM interface arising from magnetic exchange coupling. Traditionally, conventional exchange bias (CEB) systems are created by heating the AFM-FM system to above the AFM's critical Néel temperature and subsequently cooling the system in an applied magnetic field [108]. This process aligns the interfacial spins within the AFM material to those in the magnetically saturated FM material, producing an exchange bias. This exchange bias phenomenon is observed as an effective positive magnetic field contribution that manifests itself as a horizontal shift to the left in the FM material's magnetization hysteresis response to an applied magnetic field. This phenomenon was first reported by Meiklejohn and Bean in 1957, and was first observed in Co/CoO nanoparticles [6].

Since that original discovery, numerous exciting developments have been published on exchange bias. These include a variety of different AFM/FM material combinations and configurations (thin films, 'antidot' film hole arrays, etc.) to further investigate CEB [108][109]. Some reports are available indicating exchange bias systems with M-H loops shifting in the positive direction, which is opposite from established CEB materials – a phenomenon termed positive exchange bias [10]. The attenuation of exchange bias over successive hysteretic loop cycling has also been experimentally demonstrated and termed the exchange bias training effect [110]. Exchange bias has also been found to produce asymmetrical magnetization in certain

AFM-FM systems, which manifests itself as a vertical M-H loop shift [111]. Multiple physical exchange bias mechanisms have also been both theorized and identified, including the role of pinned interfacial spins, relative quantum exchange lengths, and relative material thicknesses [8][9]. Analytical and numerical models have been used to quantify and explain the exchange bias phenomenon (predominantly in the thin films configuration), with varying degrees of success [5][11][12][112]. However, it is important to note that despite these great strides, the mechanisms for exchange bias is still not yet fully understood, and the field remains rich with opportunities for discovery.

One of the most exciting discoveries in recent exchange bias research is of spontaneous exchange bias (SEB). SEB occurs in AFM/FM systems without heating the layered structure which is necessary for CEB [113]. This is typically achieved by either applying a large initial magnetic bias field at room temperature, or by controlling the fabrication parameters of the AFM or FM material. This has been demonstrated in a variety of materials; Maity et al. observed this in a $BiFeO_3$-$Bi_2Fe_4O_9$ composite [114]. More recently, Phuoc and Ong showed in 2014 that SEB can be tuned by varying the NiFeTa/IrMn sputter deposition angle, thus altering the film stress, fractional composition, and the effective exchange anisotropy [115].

The main application for exchange bias, specifically for micro-/nanoscale magnetic devices, is the contribution of passive magnetic anisotropy, i.e. without the need for energy-intensive external magnetic fields. For thermally-sensitive device fabrication processes, SEB offers a clear advantage over CEB, since CEB requires substantially elevated temperatures above the AFM material's critical Néel point. Furthermore, in applications that require reorienting the

exchange bias in-situ, reorientation of SEB, in contrast to CEB, can be readily accomplished without heating the device.

Control of exchange bias could also be achieved through a magnetoelectric approach using electrical fields to modify exchange bias. Several different magnetoelectric coupling approaches exist to achieve this objective [17]. One promising route uses strain-mediated multiferroics, which accomplishes magnetoelectric coupling using an electric field induced strain to modify the magnetic anisotropy in a magnetoelastic material [18].

Magnetoelectric control of conventional exchange bias (CEB), using both strain- and charge-mediated multiferroics, has been previously demonstrated. Wu et al. in 2010 demonstrated electrical control of exchange bias using a field-effect device with $BiFeO_3$ (ferroelectric/AFM) as the dielectric and ferromagnetic $La_{0.7}Sr_{0.3}MnO_3$ as the conducting channel, demonstrating controlled direct flipping of AFM spins in the single phase multiferroic $BiFeO_3$ [14]. Liu et al. in 2011 showed that the strength of the exchange bias (horizontal loop shift) can be modified through electrically controlling the applied strain [15]. More recently, Wu et al. in 2013 improved upon the 2010 work and reported bipolar electrical control of initiated CEB through direct flipping of the AFM spins in $BiFeO_3$. This later work demonstrated exchange bias reversibly switches between two 180-degree antiparallel stable states [16].

While there has been work on controlling CEB systems, electric-field control of SEB has not been previously studied to the authors' knowledge. Furthermore, while CEB is well documented for the Ni-NiO material system, SEB in evaporated Ni-NiO films has not previously been demonstrated [116][110][117][118]. Finally, the studies presently available for electrically

controlling reversible exchange bias accomplishes this specifically through modifying the AFM material's interfacial spins rather than through indirect coupling with the FM material [14][16].

Here we report experimental results demonstrating reversible modulations of SEB using a strain-mediated magnetoelectric heterostructure. The structure consists of electron beam evaporated Ni and NiO films deposited onto a PMN-PT ferroelectric substrate. The reversible SEB control is accomplished through modifying interfacial spins in the FM material, in contrast with existing studies that modify the interfacial spins in the AFM material [14][16].

5.2 Experimental Setup

Figure 5.1 shows a schematic of the strain-mediated multiferroic exchange bias sample used in this work. The substrate is an electrode-covered [011]-oriented [Pb(Mg1/3Nb2/3)O3](1−x)− [PbTiO3]x (PMN-PT, x ≈ 0.32) ferroelectric single crystal with in-plane dimensions of 0.5 cm by 1 cm and thickness of 0.5 mm. On the top electrode, 20 nm SiO_2 (electrical insulation), followed by 5 nm Ni (FM) and 40 nm NiO (AFM), was deposited by electron beam evaporation using a base pressure of ~10^{-6} torr. The 5 nm Ti films serve as adhesion layers for the system-substrate interface and the PMN-PT electrodes.

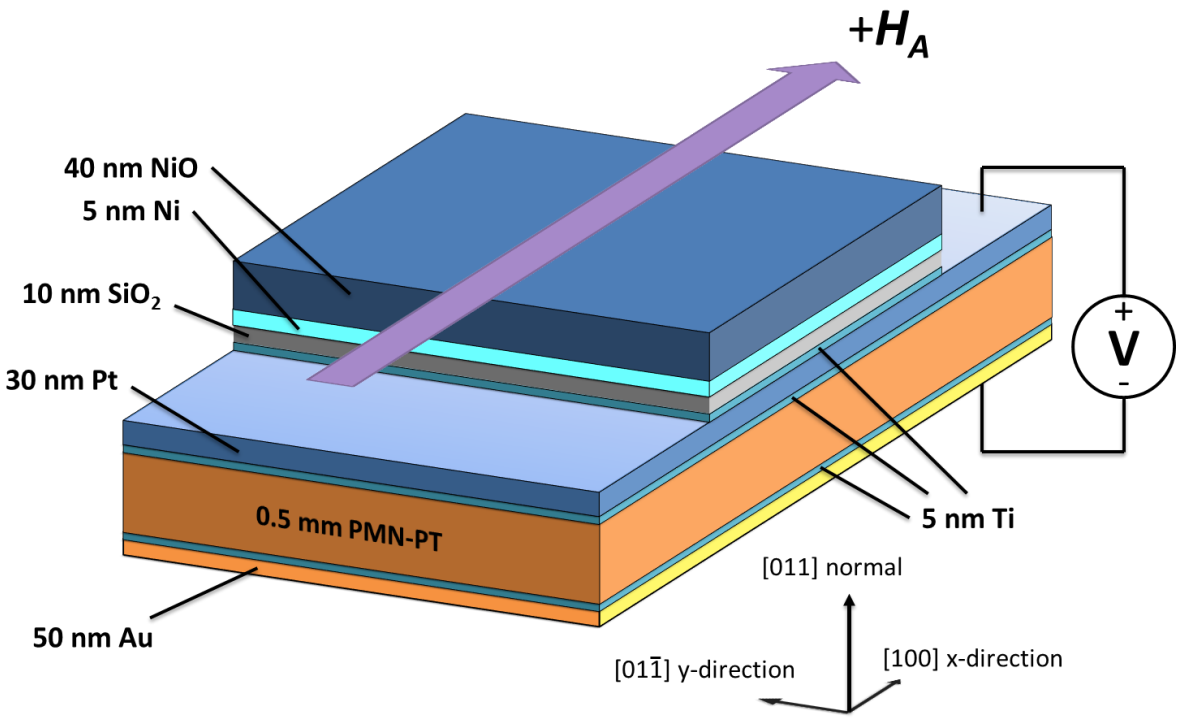

Figure 5.1: Schematic of the sample, depicting the film thicknesses, PMN-PT substrate's crystallographic directions, and applied voltage (electric field) polarity. H_a is the positive magnetic field direction for the initial 15000 Oe bias and the M-H SQUID data. As *E* is applied between the Pt and Au electrodes, the sample experiences a net tensile strain along H_a (PMN-PT [011] crystal axis), and a compressive strain in the perpendicular in-plane [100] direction.

X-ray photoelectron spectroscopy (XPS) verified that Ni_2O_3 and $Ni(OH)_2$ were absent from the NiO layer, which is known to arise for certain ranges of NiO electron beam deposition parameters [119]. The data in Figure 5.2 shows the Ni $2p^{3/2}$ peak. The Ni $2p^{1/2}$ is not shown because the fits are redundant. The two peaks (blue) located at 853.9 eV, 855.5 eV correspond to NiO and the peak (red) at 861.2 eV is the NiO satellite peak. Fitting of the peaks did not correspond to either $Ni(OH)_2$ or Ni_2O_3 phases, therefore, these are absent. XPS analysis was performed using a Kratos Axis Ultra DLD with a monochromatic Kα radiation source. The charge neutralizer filament was used to control charging of the sample. A 20 eV pass energy was used with a 0.05 eV step size. Scans were calibrated using the C 1s peak shifted to 284.8 eV.

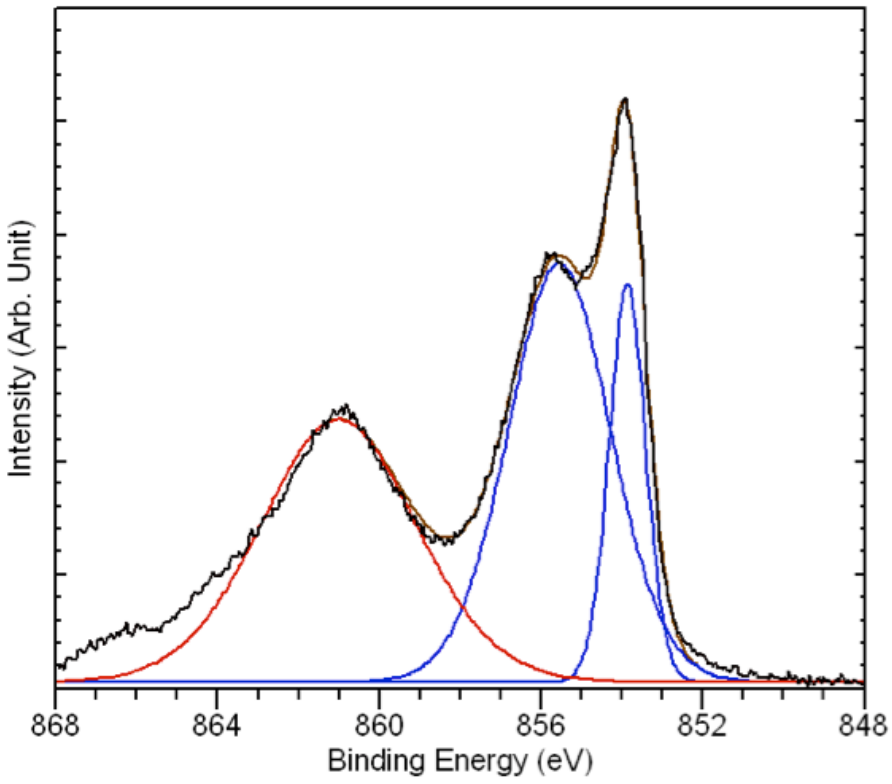

Figure 5.2: XPS composition analysis of the NiO film. Ni $2p^{3/2}$ peaks fit to NiO peaks (blue), and the NiO satellite peak (red) showing no evidence of $Ni(OH)_2$ or Ni_2O_3 phases.

The PMN-PT substrate was electrically poled through the thickness prior to deposition. The PMN-PT produced an anisotropic linear strain response to an applied electric field *E*. Figure 5.3 shows the PMN-PT strain response to an applied electric field. For higher electric fields, this particular PMN-PT composition showed a nonlinear strain response due to the presence of a phase transition to an antiferroelectric regime. For this study, the maximum electric field used was limited to below 0.4 MV/m to remain in the controllable linear response region. For this PMN-PT crystal cut, an applied electric field produces tensile strain along the x-direction ([01$\underline{1}$] crystal axis) and a compressive strain in the perpendicular in-plane [100] y-direction. It is important to note that the PMN-PT ferroelectric strain response is sensitive to composition and can vary between samples, and the strain reported here is specifically for the sample tested [22].

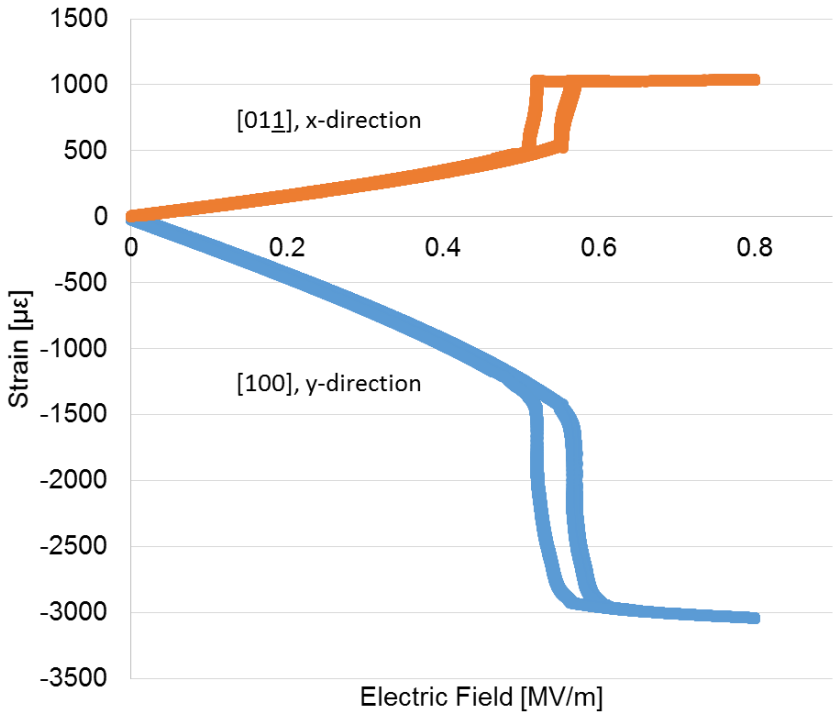

Figure 5.3: PMN-PT strain response to applied electric field. An antiferroelectric phase transformation is seen at higher electric fields for this PMN-PT composition. For this study,

to stay within the linear strain response region, electric field values did not exceed 0.4 MV/m.

Magnetic moment (*M*) measurements as a function of the applied magnetic field (*H*) along the x-direction (tensile axis) were measured in a SQUID magnetometer (measurement error below 2×10^{-7} emu). The SQUID has the capability to apply in-situ electric fields to the sample while magnetic measurements are being made. This was accomplished using a Quantum Design MPMS SQUID magnetometer with a custom hollow rod, with the sample's x-direction corresponding to the SQUID's vertical axis. Figure 5.4 depicts a schematic of the M-H measurement setup. The hollow rod allowed electrical access to the sample within the SQUID chamber via 600V-rated non-ferromagnetic wires while maintaining a barrier between atmosphere and the chamber environment (cured epoxy around the wires and within the rod form a plug that maintains pressure and prevents gas flow). Electric field was applied via voltage from a Trek Model 50/750 high-voltage amplifier (for the 0.5 mm thick PMN-PT substrate, 100 V corresponds to 0.2 MV/m) and a DC power source. The electrical lead wires were secured to the sample within the plastic sample holder using Kapton® polyimide tape. Additional trailing wires were also installed at the opposing end of the sample to maintain symmetry of all materials with respect to the SQUID coils. The SEB was created by applying an initial bias magnetic field H_a = 15000 Oe for approximately 5 min along the in-plane x-direction shown in Figure 5.1. Following the creation of SEB, the M-H data on the sample was obtained at room temperature for multiple electric field values between 0 and 0.4 MV/m. Following this set of tests, the same sample was rotated 90 degrees in the SQUID, and the M-H data was measured along the y-direction for multiple electric fields. For the measurements along the y-direction, the SEB was still present along the x-direction, as previously set in the sample. In some instances, these tests were performed over several days; thus, the SEB reported in this work is stable with respect to time.

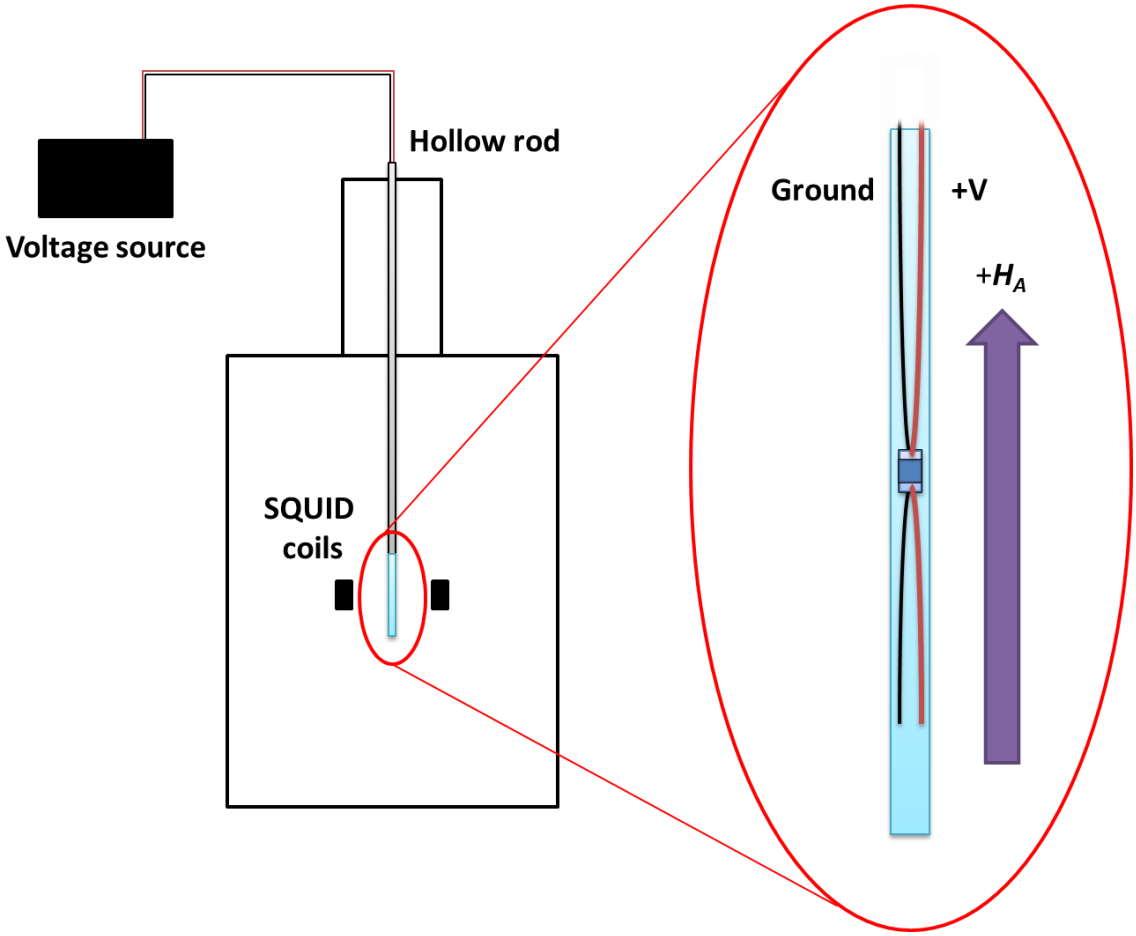

Figure 5.4: Schematic side view diagram of the SQUID magnetometer with the in-situ applied electric field setup, depicting the fully-installed sample (from Figure 1). The sample's x-direction corresponds to the SQUID's vertical axis.

5.3 Results and Discussion

Figure 5.5 summarizes the M-H results for measurements in the SEB direction (x-direction). The data shows that a positive SEB in the Ni-NiO system (loop shift to the right) is produced, and it varies with applied electric-field (i.e. strain modifies magnetic anisotropy). The A, B, C, and D labels on this figure refer to the blue data points (for 0.4 MV/m) in the top right, top left, bottom left, and bottom right plot quadrants, respectively; a later discussion will refer to these regions specifically. Figure 5.6 is a plot comparing H_x values of the left H_c, overall loop shift H_{EB} (calculated centroid of M-H loops), and right H_c for various applied electric field values. For all electric field values tested, the M-H curves clearly shows a SEB bias to the right. As the applied electric field is increased from zero up to a moderate 0.15 MV/m, the left coercive field magnitude shrinks by approximately 5.5 Oe (i.e. .from -8.9 Oe to -3.4 Oe) and the right coercive field magnitude shrinks approximately 6.2 Oe (i.e. from 33.7 Oe to 27.5 Oe). As the electric field is increased above this moderate value, i.e. from 0.15 MV/m to 0.4 MV/m, the left coercivity magnitude reverses trend and begins to increase to -16.5 Oe (i.e. from a value of -3.4 Oe at 0.15 MV/m). Meanwhile, the right coercive field continues the monotonic decrease observed in the moderate electric field regime. With regard to magnetic remanence presented in Figure 5.5, the test data shows a monotonically decreasing remanence due to increasing electric field values, from $M_r/M_s \sim 1$ to $M_r/M_s \sim 0.16$ as E increased from 0 to 0.4 MV/m.

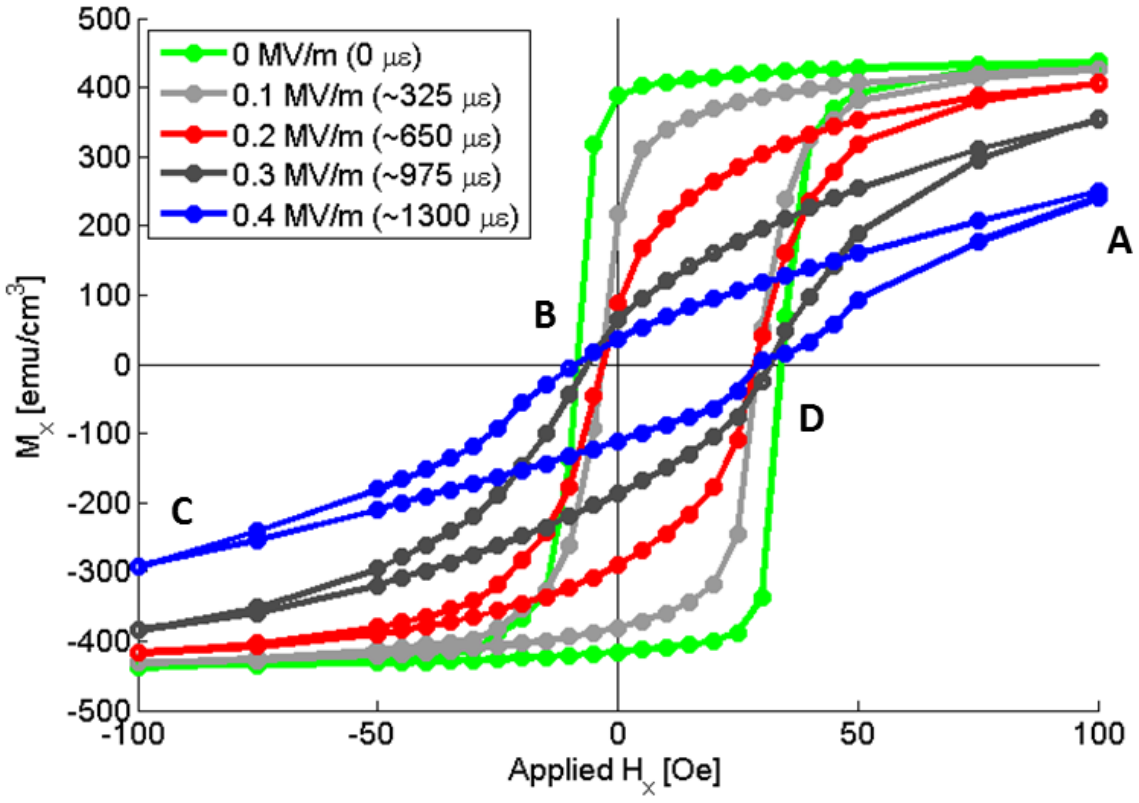

Figure 5.5: M-H SQUID data of the sample in the x-direction (along the exchange bias axis) for multiple in-situ E values. As E increases, the magnitude of the left coercive field value shrinks and then increases, while the right coercive field value predominantly decreases. A, B, C, and D refer to the blue data points (for 0.4 MV/m) in the top right, top left, bottom left, and bottom right plot quadrants, respectively.

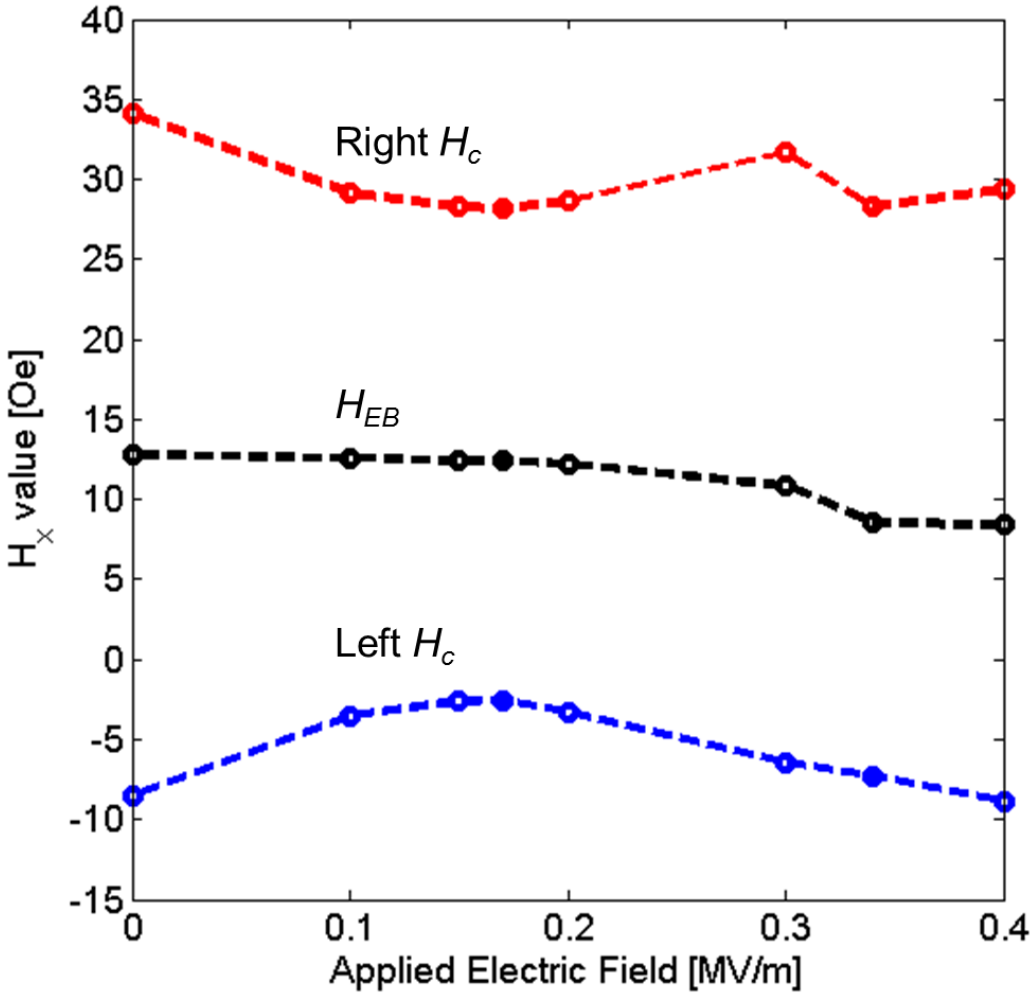

Figure 5.6: Plot comparing H_x values of the left coercive field, overall loop shift (centroid of M-H loops), and right coercive field for various applied electric field.

Figure 5.7 shows the M-H response in the y-direction. As addressed previously, all SEB field settings for this sample was in the positive x-direction, and results in Figure 5.7 show the influence of electric field on magnetic anisotropy perpendicular to the SEB in the x-direction. Figure 5.7 data shows negligible exchange bias shifts for all electric field states (<5 Oe). However, Figure 5.7 does show a considerable increase in coercive field values as the electric field induced strain increases, i.e. from 20 Oe to 41 Oe, as the electric field increases from 0.0 MV/m to 0.4 MV/m.

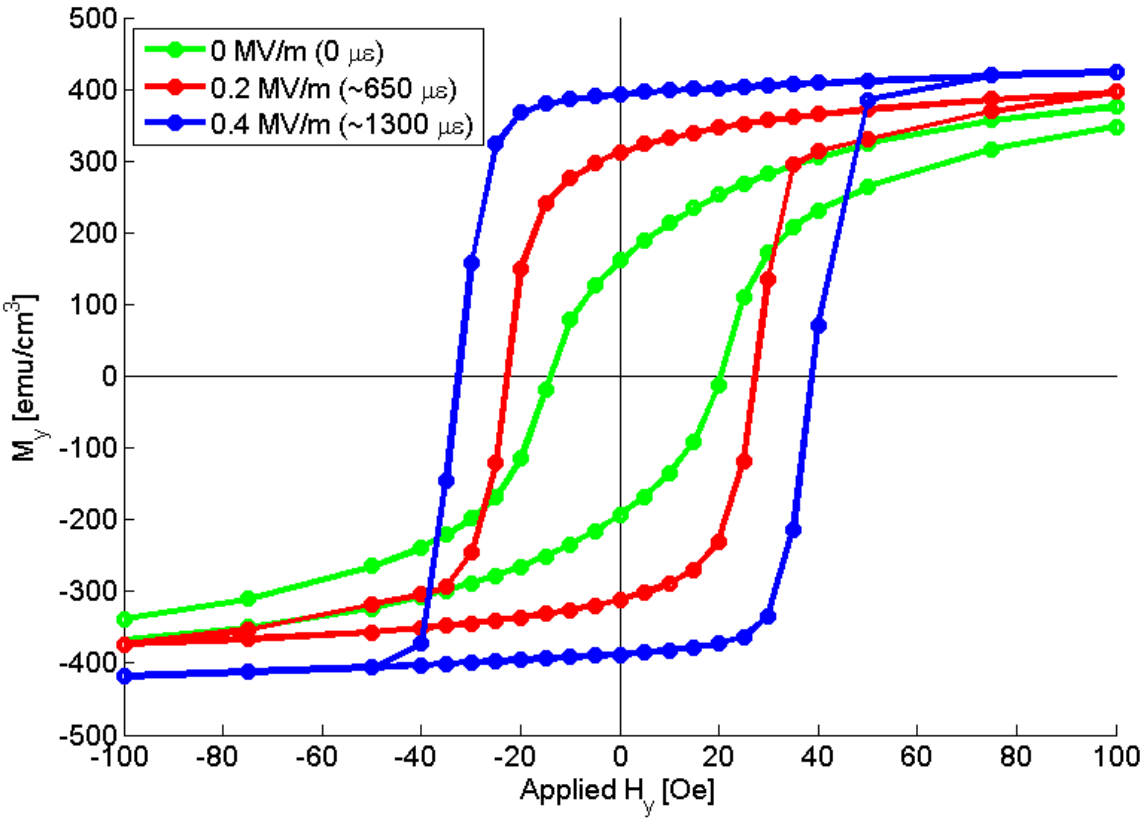

Figure 5.7: M-H SQUID data of the sample in the y-direction (perpendicular to the exchange bias axis, in-plane) for multiple in-situ *E* values. As *E* increases, the y-direction becomes increasingly magnetically easy, forming a wider and squarer hysteresis loop. Negligible horizontal shift is observed for all *E* values.

The data presented in Figure 5.5 and Figure 5.6 strongly suggests that the SEB AFM-FM coupling is present in the Ni-NiO system along the initial magnetic bias field direction (x-direction). Furthermore, this electric field induced exchange bias shift differs from that of previously reported electric field induced CEB systems. Specifically, CEB systems show either a consistently increasing or decreasing shift in both the left and right coercive field values as the electric field is increased/decreased [16][15]. However, as can be seen in Figure 5.5 and Figure 5.6, the left coercive field branch of the SEB display a decrease followed by an increase in the SEB, in marked contrast to CEB reported data.

The left coercive field branch trend reversal is attributed to the unique coupling present during the creation of the SEB in the sample. We believe that the initial large bias field treatment in SEB does not fully orient the AFM spins as completely/firmly as does the CEB approach, and this weaker spin orientation can be influenced by the direction of the local FM spins. Consequently, rather than the relatively organized pinned antiparallel layers typical of AFM spins arising from CEB, the AFM spins in SEB are less organized, resulting in more spin frustration sites at the AFM-FM interface and providing a degree of ductility in the arrangement of the local AFM spins. The modification of the easy axis in the soft magnetoelastic Ni layer with electric field induced strain produces a driving energy that can influence the more ductile AFM spins arising from these frustration sites. For electric fields below a critical value, the Ni spins prefer to lie along the x-direction due to both strain and AFM exchange anisotropy. However, as the electric field is increased the strain anisotropic energy is sufficient to cause the Ni spins to prefer the new perpendicular y-direction easy axis at near-zero magnetic fields. This subsequently causes reorganization of the AFM spins that are directly exchange coupled to these Ni spins in the neighborhood of the coercive fields. This influences the exchange bias

experienced in the FM Ni magnetoelastic material, resulting in the observed initial decreasing and subsequent increasing of the left coercivity.

Figure 5.8 provides a possible explanation for the observed electric field induced SEB modifications. The squares represent interfacial areas within a single domain of either Ni or NiO. The illustration is not meant to be a literal depiction of real spin behavior, but instead is meant to serve as a simplified conceptual aid; for instance, real exchange bias is understood to encompass the interaction of spin states in all 3 dimensions[8]. In Figure 5.8, the exchange bias effect is weakest when more unstable AFM interface spins (shown in red) are canted from the predominant bias direction (x-direction). The red arrows represent relatively unstable NiO interfacial spins capable of canting in response to the Ni interfacial spins. The depicted canting angles are exaggerated in this depiction for clarity; it has been proposed in the literature that very small modifications to AFM spin angle can drastically influence the exchange bias behavior[14]. Interactions between nearby unstable spins can locally reduce the canting for position A (see Figures 4 and 7), in sharp contrast to the electric field induced strain causing maximum canting for B and C. Therefore, transitions between increased and decreased exchange bias effects for occur positions B whenever the measured M-H response loop crosses the horizontal y-axis (H = 0). Referring again to Figure 5.5, this is precisely what is observed in the results, validating this explanation.

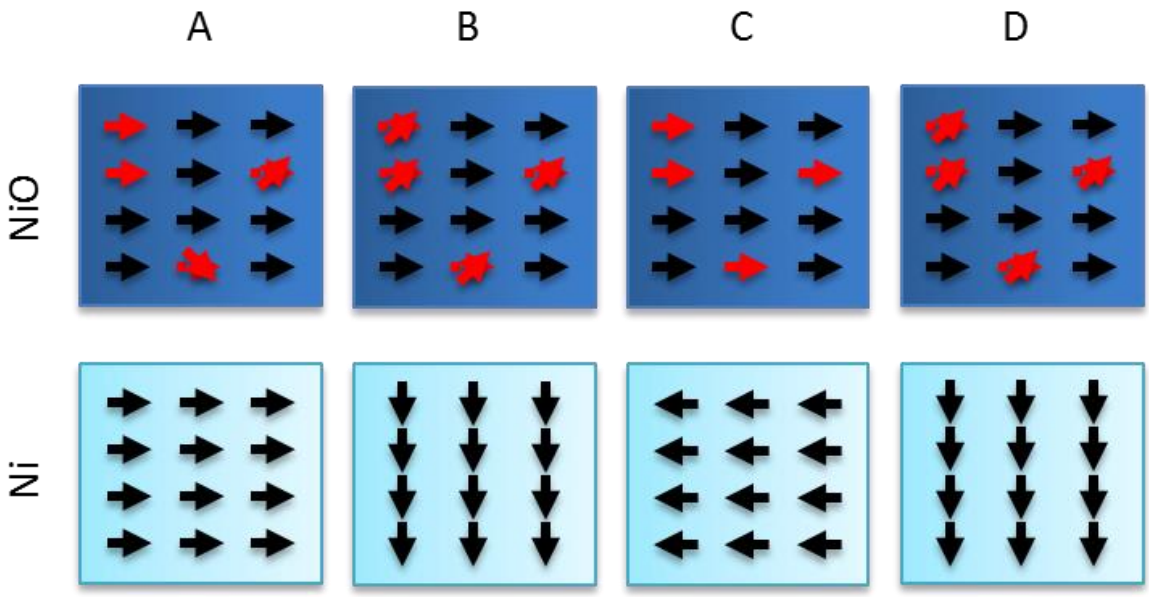

Figure 5.8: Illustrative cartoon of spin states explaining the behavior of a strained x-oriented SEB sample (electric field applied) at different applied magnetic fields. This is not meant to be a literal depiction, but a highly simplified conceptual aid. Each square represents a planar area of either Ni or NiO spins within a single magnetic domain. Letters correspond to the data points in the 4 quadrants of the blue curve in Figure 5.5. Red arrows represent unstable NiO interfacial spins that arise from SEB, which are capable of canting in response to the Ni interfacial spins (canting angles exaggerated in this depiction for clarity).

5.4 Conclusion

This work experimentally demonstrates reversible modulations of SEB behavior using a strain-mediated magnetoelectric layered structure consisting of electron beam evaporated Ni and NiO films on a straining PMN-PT ferroelectric substrate. This reversible control is accomplished through modifying interfacial spins in the FM material, in contrast with existing studies that modify the AFM material's interfacial spins. The demonstrated novel response to electrically induced strain can be explained by the inherent unorganized spin state of SEB in contrast to that of a CEB system and the corresponding effect of the Ni FM layer on the NiO AFM unstable interfacial spins. The ability to effectively shift SEB behavior with an electric field could produce new approaches for the design of next generation nano-/microscale magnetic devices without the temperature limitations of implementing more conventional exchange bias approaches.

6. Conclusion

This dissertation outlined how magnetoelastic composite systems exhibit coupling phenomena. The first chapter explained the necessary background in magnetic materials and magnetoelectric systems to fully appreciate the research contributions in the following chapters. The different classifications of magnetic material behavior (diamagnetism, paramagnetism, ferromagnetism, antiferromagnetism, and ferrimagnetism) were presented. This chapter then introduced the notion that exchange interactions between antiferromagnetic and ferromagnetic materials can produce novel nanoscale magnetic behavior. Next, magnetoelectric systems in the form of strain-mediated multiferroic composites was explained. To accomplish this, the chapter introduced both magnetoelastic and ferroelectric materials, which, when coupled together, forms an electrically controllable net magnetization.

The second chapter outlines a simulation paradigm that for the first time incorporates both mechanics and micromagnetics. Coupled equations from the LLG micromagnetic model and the mechanical equation of motion were formulated in their weak forms to be used in a COMSOL multiphysics simulator. This is capable of accurately simulating magnetization dynamics of magnetoelastic nanostructures of arbitrary geometry.

The third chapter applies this coupled model to designing a bistable voltage-controlled straining nanomagnet. The nanomagnet can be deterministically switched between two orthogonal magnetization states via the application of electric field to patterned electrodes. Furthermore, this is the first time that a simulation package has modeled a complete strain-mediated multiferroic system, including both fully coupled representations of strained magnetoelastic structures and a straining ferroelectric actuator. Not only does the model fully

model the composite device, but also the simulated device is essentially a repeatably writable binary bit, demonstrating that the model can indeed be used to design a computer memory device.

The fourth chapter presents an experimental study that demonstrates how strain can be used to control dipole coupling behavior in repeated arrays of closely-spaced nanomagnets. Specifically, the work shows that a chain of circular nanomagnets can be used to propagate binary information. Whereas the previous chapter shows the potential of strain-mediated multiferroics for memory applications, this chapter provides a path to using strain-mediated multiferroics for logic devices.

The fifth chapter experimentally demonstrates reversible modulations of SEB behavior using a strain-mediated magnetoelectric layered structure consisting AFM and FM films on a straining ferroelectric substrate. This reversible control is accomplished through modifying interfacial spins in the FM material, in contrast with existing studies that modify the AFM material's interfacial spins. The demonstrated novel response to electrically induced strain can be explained by the inherent unorganized spin state of SEB in contrast to that of a CEB system and the corresponding effect of the FM layer on the AFM unstable interfacial spins. The ability to effectively shift SEB behavior with an electric field could produce new approaches for the design of next generation nano-/microscale magnetic devices (both memory and logic) without the temperature limitations of implementing more conventional exchange bias approaches.

Looking ahead, the work presented in this dissertation can all contribute to the realization of advanced nanoscale magnetic computing devices. The fully coupled mechanical modeling techniques of the second and third chapters can be used to accurately design magnetoelastic geometries. The interacting anisotropies of strain with both the fourth chapter's dipole coupling

and the fifth chapter's spontaneous exchange bias can be used as engineering controls for constraining the magnetization states of interacting nanomagnets. These are critical for rapid deployment and manufacturing; materials development is largely completed in uncertain time scales, and all of the techniques outlined in this dissertation do not need additional novel materials. Altogether, the work in this dissertation can lead to both advanced understanding of nanoscale magnetic phenomena and novel engineered magnetic computing devices.

7. References

[1] F. J. Himpsel, J. E. Ortega, G. J. Mankey, and R. F. Willis, "Magnetic nanostructures," *Advances in Physics*, vol. 47, no. 4, pp. 511–597, Jul. 1998.

[2] M. T. Niemier, G. H. Bernstein, G. Csaba, a Dingler, X. S. Hu, S. Kurtz, S. Liu, J. Nahas, W. Porod, M. Siddiq, and E. Varga, "Nanomagnet logic: progress toward system-level integration.," *Journal of physics. Condensed matter : an Institute of Physics journal*, vol. 23, no. 49, p. 493202, Dec. 2011.

[3] B. Cullity and C. Graham, *Introduction to magnetic materials*, vol. 12, no. 3. 2009.

[4] R. C. O'Handley, *Modern Magnetic Materials: Principles and Applications*. 2000.

[5] P. Miltényi, M. Gierlings, J. Keller, B. Beschoten, G. Güntherodt, U. Nowak, and K. Usadel, "Diluted Antiferromagnets in Exchange Bias: Proof of the Domain State Model," *Physical Review Letters*, vol. 84, no. 18, pp. 4224–4227, May 2000.

[6] W. Meiklejohn and C. Bean, "New magnetic anisotropy," *Physical Review*, vol. 2, no. c, 1957.

[7] a. Punnoose, H. Magnone, M. Seehra, and J. Bonevich, "Bulk to nanoscale magnetism and exchange bias in CuO nanoparticles," *Physical Review B*, vol. 64, no. 17, p. 174420, Oct. 2001.

[8] R. L. Stamps, "Mechanisms for exchange bias," *Journal of Physics D: Applied Physics*, vol. 34. pp. 444–444, 2001.

[9] H. Ohldag, a. Scholl, F. Nolting, E. Arenholz, S. Maat, a. Young, M. Carey, and J. Stöhr, "Correlation between Exchange Bias and Pinned Interfacial Spins," *Physical Review Letters*, vol. 91, no. 1, p. 017203, Jul. 2003.

[10] X.-Y. Xu, Y.-J. Gao, Y.-L. Wang, and J.-G. Hu, "Thickness dependence of positive exchange bias in ferromagnetic/antiferromagnetic bilayers," *Solid State Communications*, vol. 151, no. 13, pp. 952–955, Jul. 2011.

[11] N. C. Koon, "Calculations of Exchange Bias in Thin Films with Ferromagnetic¯Antiferromagnetic Interfaces," pp. 4865–4868, 1997.

[12] M. Kiwi, "Exchange bias theory," *Journal of Magnetism and Magnetic Materials*, vol. 234, no. 3, pp. 584–595, Sep. 2001.

[13] V. Skumryev, S. Stoyanov, Y. Zhang, G. Hadjipanayis, D. Givord, and J. Nogues, "Beating the superparamagnetic limit with exchange bias," *Nature*, vol. 423, no. June, pp. 2–6, 2003.

[14] S. M. Wu, S. a Cybart, P. Yu, M. D. Rossell, J. X. Zhang, R. Ramesh, and R. C. Dynes, "Reversible electric control of exchange bias in a multiferroic field-effect device.," *Nature materials*, vol. 9, no. 9, pp. 756–61, Sep. 2010.

[15] M. Liu, J. Lou, S. Li, and N. X. Sun, "E-Field Control of Exchange Bias and Deterministic Magnetization Switching in AFM/FM/FE Multiferroic Heterostructures," *Advanced Functional Materials*, vol. 21, no. 13, pp. 2593–2598, Jul. 2011.

[16] S. Wu, S. Cybart, D. Yi, J. Parker, R. Ramesh, and R. Dynes, "Full Electric Control of Exchange Bias," *Physical Review Letters*, vol. 110, no. 6, p. 067202, Feb. 2013.

[17] M. Fiebig, "Revival of the magnetoelectric effect," *Journal of Physics D: Applied Physics*, vol. 38, no. 8, pp. R123–R152, Apr. 2005.

[18] W. Eerenstein, N. D. Mathur, and J. F. Scott, "Multiferroic and magnetoelectric materials.," *Nature*, vol. 442, no. 7104, pp. 759–65, Aug. 2006.

[19] C. Dtvtslon, N. Surface, W. Bethesda, and C. Associates, "Magnetostriction of Terfenol-D Heat Treated Under Compressive Stress," vol. 3, no. 5, pp. 3817–3819, 1999.

[20] J. Valasek, "Piezo-electric and allied phenomena in Rochelle salt," *Physical review*, no. 4, 1921.

[21] G. H. Haertling, "Ferroelectric Ceramics: History and Technology," *Journal of the American Ceramic Society*, vol. 82, no. 4, pp. 797–818, Apr. 1999.

[22] T. Wu, P. Zhao, M. Bao, A. Bur, J. L. Hockel, K. Wong, K. P. Mohanchandra, C. S. Lynch, and G. P. Carman, "Domain engineered switchable strain states in ferroelectric (011) [Pb(Mg1/3Nb2/3)O3](1−x)-[PbTiO3]x (PMN-PT, x≈0.32) single crystals," *Journal of Applied Physics*, vol. 109, no. 12, p. 124101, 2011.

[23] J. R. Yu, V. Alfredo, C. Arazo, K. U. Chino, and H. K. Im, "Magnetoelectric Properties in Piezoelectric and Magnetostrictive Laminate Composites," vol. 40, no. 8, pp. 4948–4951, 2001.

[24] N. a Spaldin and M. Fiebig, "Materials science. The renaissance of magnetoelectric multiferroics.," *Science (New York, N.Y.)*, vol. 309, no. 5733, pp. 391–2, Jul. 2005.

[25] T. Wu, A. Bur, K. Wong, P. Zhao, C. S. Lynch, P. K. Amiri, K. L. Wang, and G. P. Carman, "Electrical control of reversible and permanent magnetization reorientation for magnetoelectric memory devices," *Applied Physics Letters*, vol. 98, no. 26, p. 262504, 2011.

[26] J. L. Hockel, A. Bur, T. Wu, K. P. Wetzlar, and G. P. Carman, "Electric field induced magnetization rotation in patterned Ni ring/Pb(Mg1/3Nb2/3)O3](1−0.32)-[PbTiO3]0.32 heterostructures," *Applied Physics Letters*, vol. 100, no. 2, p. 022401, 2012.

[27] C.-J. Hsu, J. L. Hockel, and G. P. Carman, "Magnetoelectric manipulation of domain wall configuration in thin film Ni/[Pb(Mn1/3Nb2/3)O3]0.68-[PbTiO3]0.32 (001) heterostructure," *Applied Physics Letters*, vol. 100, no. 9, p. 092902, 2012.

[28] J. Atulasimha and S. Bandyopadhyay, "Bennett clocking of nanomagnetic logic using multiferroic single-domain nanomagnets," *Applied Physics Letters*, vol. 97, no. 17, p. 173105, 2010.

[29] K. Roy, S. Bandyopadhyay, and J. Atulasimha, "Switching dynamics of a magnetostrictive single-domain nanomagnet subjected to stress," *Physical Review B*, vol. 83, no. 22, p. 224412, Jun. 2011.

[30] E. Varga, G. Csaba, G. H. Bernstein, and W. Porod, "Domain-Wall Assisted Switching of Single-Domain Nanomagnets," *IEEE Transactions on Magnetics*, vol. 48, no. 11, pp. 3563–3566, Nov. 2012.

[31] H. K. D. Kim, L. T. Schelhas, S. Keller, J. L. Hockel, S. H. Tolbert, and G. P. Carman, "Magnetoelectric control of superparamagnetism.," *Nano letters*, vol. 13, no. 3, pp. 884–8, Mar. 2013.

[32] J. H. Chung, S. J. Chung, S. Lee, B. J. Kirby, J. a. Borchers, Y. J. Cho, X. Liu, and J. K. Furdyna, "Carrier-mediated antiferromagnetic interlayer exchange coupling in diluted magnetic semiconductor multilayers Ga1-xMnxAs/GaAs:Be," *Physical Review Letters*, vol. 101, no. 23, pp. 1–4, 2008.

[33] J. M. Rondinelli, M. Stengel, and N. a Spaldin, "Carrier-mediated magnetoelectricity in complex oxide heterostructures.," *Nature nanotechnology*, vol. 3, no. January, pp. 46–50, 2008.

[34] I. L. Castro, V. P. Nascimento, E. C. Passamani, a. Y. Takeuchi, C. Larica, M. Tafur, and F. Pelegrini, "The role of the (111) texture on the exchange bias and interlayer coupling effects observed in sputtered NiFe/IrMn/Co trilayers," *Journal of Applied Physics*, vol. 113, no. 20, 2013.

[35] M. Ziese, F. Bern, and I. Vrejoiu, "Exchange bias in manganite/SrRuO3 superlattices," *Journal of Applied Physics*, vol. 113, no. 6, pp. 0–6, 2013.

[36] Z. Li and S. Zhang, "Magnetization dynamics with a spin-transfer torque," no. May, pp. 1–10, 2003.

[37] M. D. Stiles and J. Miltat, "Spin-transfer torque and dynamics," *Topics in Applied Physics*, vol. 101, pp. 225–308, 2006.

[38] Z. Diao, Z. Li, S. Wang, Y. Ding, A. Panchula, E. Chen, L.-C. Wang, and Y. Huai, "Spin-transfer torque switching in magnetic tunnel junctions and spin-transfer torque random access memory," *Journal of Physics: Condensed Matter*, vol. 19, no. 16, p. 165209, 2007.

[39] S. Tehrani, J. M. Slaughter, E. Chen, M. Durlam, J. Shi, and M. Deherrera, "Progress and outlook for mram technology," *IEEE Transactions on Magnetics*, vol. 35, no. 5 PART 1, pp. 2814–2819, 1999.

[40] S. Tehrani, B. Engel, J. M. Slaughter, E. Chen, M. DeHerrera, M. Durlam, P. Naji, R. Whig, J. Janesky, and J. Calder, "Recent developments in magnetic tunnel junction MRAM," *IEEE Transactions on Magnetics*, vol. 36, no. 5, pp. 2752–2757, 2000.

[41] Y. Wang, J. Hu, Y. Lin, and C.-W. Nan, "Multiferroic magnetoelectric composite nanostructures," *NPG Asia Materials*, vol. 2, no. 2, pp. 61–68, 2010.

[42] C. W. Nan, M. I. Bichurin, S. Dong, D. Viehland, and G. Srinivasan, "Multiferroic magnetoelectric composites: Historical perspective, status, and future directions," *Journal of Applied Physics*, vol. 103, no. 3, 2008.

[43] J.-M. M. Hu, Z. Li, J. Wang, J. Ma, Y. H. Lin, and C. W. Nan, "A simple bilayered magnetoelectric random access memory cell based on electric-field controllable domain structure," *Journal of Applied Physics*, vol. 108, no. 4, p. 043909, 2010.

[44] B. Zhu, C. C. H. Lo, S. J. Lee, and D. C. Jiles, "Micromagnetic modeling of the effects of stress on magnetic properties," *Journal of Applied Physics*, vol. 89, no. 11 II, pp. 7009–7011, 2001.

[45] M. Weiler, a. Brandlmaier, S. Geprägs, M. Althammer, M. Opel, C. Bihler, H. Huebl, M. S. Brandt, R. Gross, and S. T. B. Goennenwein, "Voltage controlled inversion of magnetic anisotropy in a ferromagnetic thin film at room temperature," *New Journal of Physics*, vol. 11, 2009.

[46] Y. Chen, T. Fitchorov, C. Vittoria, and V. G. Harris, "Electrically controlled magnetization switching in a multiferroic heterostructure," *Applied Physics Letters*, vol. 97, no. 5, pp. 17–20, 2010.

[47] T. Brintlinger, S.-H. Lim, K. H. Baloch, P. Alexander, Y. Qi, J. Barry, J. Melngailis, L. Salamanca-Riba, I. Takeuchi, and J. Cumings, "In situ observation of reversible nanomagnetic switching induced by electric fields.," *Nano letters*, vol. 10, no. 4, pp. 1219–23, Apr. 2010.

[48] T. H. E. Lahtinen, K. J. a. Franke, and S. van Dijken, "Electric-field control of magnetic domain wall motion and local magnetization reversal," *Scientific Reports*, vol. 2, pp. 1–6, 2012.

[49] D. Z. Bai, "Micromagnetic simulation of effect of stress-induced anisotropy in soft magnetic thin films," *Journal of Applied Physics*, vol. 95, no. 11, p. 6864, 2004.

[50] G. Khanna, B. M. Clemens, H. Zhou, and H. N. Bertram, "Micromagnetic study of anisotropy sources in textured longitudinal media," *IEEE Transactions on Magnetics*, vol. 37, no. 4 I, pp. 1468–1470, 2001.

[51] J.-M. Hu, G. Sheng, J. X. Zhang, C. W. Nan, and L. Q. Chen, "Phase-field simulation of electric-field-induced in-plane magnetic domain switching in magnetic/ferroelectric layered heterostructures," *Journal of Applied Physics*, vol. 109, no. 12, p. 123917, 2011.

[52] A. Bur, T. Wu, J. Hockel, C.-J. J. Hsu, H. K. D. Kim, T.-K. K. Chung, K. Wong, K. L. Wang, and G. P. Carman, "Strain-induced magnetization change in patterned ferromagnetic nickel nanostructures," *Journal of Applied Physics*, vol. 109, no. 12, p. 123903, 2011.

[53] J. Dean, M. T. Bryan, G. Hrkac, a. Goncharov, C. L. Freeman, M. a. Bashir, T. Schrefl, and D. a. Allwood, "The incorporation of the Cauchy stress matrix tensor in micromagnetic simulations," *Journal of Applied Physics*, vol. 108, no. 7, 2010.

[54] L. Baňas, "Numerical Methods for the Landau-Lifshitz-Gilbert Equation," *Numerical Analysis and Its Applications*, pp. 158–165, 2005.

[55] F. ALOUGES and P. JAISSON, "Convergence of a finite element discretization for the Landau–Lifshitz equations in micromagnetism," *Mathematical Models and Methods in Applied Sciences*, vol. 16, no. 02. pp. 299–316, 2006.

[56] Y. C. Shu, M. P. Lin, and K. C. Wu, "Micromagnetic modeling of magnetostrictive materials under intrinsic stress," *Mechanics of Materials*, vol. 36, no. 10, pp. 975–997, Oct. 2004.

[57] J. X. X. Zhang and L. Q. Q. Chen, "Phase-field microelasticity theory and micromagnetic simulations of domain structures in giant magnetostrictive materials," *Acta Materialia*, vol. 53, no. 9, pp. 2845–2855, May 2005.

[58] A. Hubert and M. Rührig, "Micromagnetic analysis of thin-film elements (invited)," *Journal of Applied Physics*, vol. 69, no. 8, pp. 6072–6077, 1991.

[59] S. a. Cavill, D. E. Parkes, J. Miguel, S. S. Dhesi, K. W. Edmonds, R. P. Campion, and a. W. Rushforth, "Electrical control of magnetic reversal processes in magnetostrictive structures," *Applied Physics Letters*, vol. 102, no. 3, 2013.

[60] E. P. W. E. C. Stoner, "A Mechanism of Magnetic Hysteresis in Heterogenous Alloys," *Philosophical Transactions of the Royal Society of London*, vol. 240, no. 826, pp. 599–642, 1948.

[61] T. L. Gilbert, "A Phenomenological Theory of Damping in Ferromagnetic Materials," *IEEE Transactions on Magnetics*, vol. 40, no. 6, pp. 3443–3449, 2004.

[62] D. R. Fredkin and T. R. Koehler, "Hybrid method for computing demagnetizing fields," *IEEE Transactions on Magnetics*, vol. 26, no. 2, pp. 415–417, 1990.

[63] H. Szambolics, L. D. Buda-Prejbeanu, J. C. Toussaint, and O. Fruchart, "A constrained finite element formulation for the Landau-Lifshitz-Gilbert equations," *Computational Materials Science*, vol. 44, no. 2, pp. 253–258, 2008.

[64] R. Hu, A.-K. Soh, G.-P. Zheng, and Y. Ni, "Micromagnetic modeling studies on the effects of stress on magnetization reversal and dynamic hysteresis," *Journal of Magnetism and Magnetic Materials*, vol. 301, no. 2, pp. 458–468, Jun. 2006.

[65] A. Roy, R. Gupta, and A. Garg, "Multiferroic memories," *Advances in Condensed Matter Physics*, vol. 2012, 2012.

[66] W. Eerenstein, M. Wiora, J. L. Prieto, J. F. Scott, and N. D. Mathur, "Giant sharp and persistent converse magnetoelectric effects in multiferroic epitaxial heterostructures.," *Nature materials*, vol. 6, no. 5, pp. 348–351, 2007.

[67] N. a Pertsev and H. Kohlstedt, "Resistive switching via the converse magnetoelectric effect in ferromagnetic multilayers on ferroelectric substrates.," *Nanotechnology*, vol. 21, no. 47, p. 475202, Nov. 2010.

[68] J.-M. Hu, Z. Li, L.-Q. Chen, and C.-W. Nan, "High-density magnetoresistive random access memory operating at ultralow voltage at room temperature," *Nature Communications*, vol. 2, p. 553, 2011.

[69] N. Tiercelin, Y. Dusch, V. Preobrazhensky, and P. Pernod, "Magnetoelectric memory using orthogonal magnetization states and magnetoelastic switching," *Journal of Applied Physics*, vol. 109, no. 7, pp. 1–4, 2011.

[70] R. Ramesh and N. a Spaldin, "Multiferroics: progress and prospects in thin films," *Nature materials*, vol. 6, no. 1, pp. 21–29, 2007.

[71] T. K. Chung, S. Keller, and G. P. Carman, "Electric-field-induced reversible magnetic single-domain evolution in a magnetoelectric thin film," *Applied Physics Letters*, vol. 94, no. 13, pp. 92–95, 2009.

[72] T. K. Chung, K. Wong, S. Keller, K. L. Wang, and G. P. Carman, "Electrical control of magnetic remanent states in a magnetoelectric layered nanostructure," *Journal of Applied Physics*, vol. 106, no. 10, 2009.

[73] Z. Li, J. Wang, Y. Lin, and C. W. Nan, "A magnetoelectric memory cell with coercivity state as writing data bit," *Applied Physics Letters*, vol. 96, no. 16, p. 162505, 2010.

[74] G. Dai, Q. Zhan, H. Yang, Y. Liu, X. Zhang, Z. Zuo, B. Chen, and R.-W. Li, "Controllable strain-induced uniaxial anisotropy of Fe81Ga19 films deposited on flexible bowed-substrates," *Journal of Applied Physics*, vol. 114, no. 17, p. 173913, 2013.

[75] T. Wu, A. Bur, H. K. D. Kim, P. Zhao, and G. P. Carman, "Giant electrical control of magnetic anisotropy in magnetoelectric heterostructures using (011) PMN-PT single crystal," vol. 7978, no. 011, pp. 797818–797818–8, 2011.

[76] T. Wu, A. Bur, P. Zhao, K. P. Mohanchandra, K. Wong, K. L. Wang, C. S. Lynch, and G. P. Carman, "Giant electric-field-induced reversible and permanent magnetization reorientation on magnetoelectric Ni/(011) [Pb (Mg1/3 Nb 2/3) O3](1-x) - [PbTiO3] x heterostructure," *Applied Physics Letters*, vol. 98, no. 1, pp. 7–10, 2011.

[77] N. Moutis, D. Suarez-Sandoval, and D. Niarchos, "Voltage-induced modification in magnetic coercivity of patterned Co50Fe50 thin film on piezoelectric substrate," *Journal of Magnetism and Magnetic Materials*, vol. 320, no. 6, pp. 1050–1055, Mar. 2008.

[78] F. Zavaliche, H. Zheng, L. Mohaddes-Ardabili, S. Y. Yang, Q. Zhan, P. Shafer, E. Reilly, R. Chopdekar, Y. Jia, P. Wright, D. G. Schlom, Y. Suzuki, and R. Ramesh, "Electric field-induced magnetization switching in epitaxial columnar nanostructures," *Nano Letters*, vol. 5, no. 9, pp. 1793–1796, 2005.

[79] J. Cui, J. L. Hockel, P. K. Nordeen, D. M. Pisani, C. Y. Liang, G. P. Carman, and C. S. Lynch, "A method to control magnetism in individual strain-mediated magnetoelectric islands," *Applied Physics Letters*, vol. 103, no. 23, pp. 2011–2016, 2013.

[80] N. D'Souza, J. Atulasimha, and S. Bandyopadhyay, "Four-state nanomagnetic logic using multiferroics," *Journal of Physics D: Applied Physics*, vol. 265001, no. 26, p. 265001, Jul. 2011.

[81] V. Laukhin, V. Skumryev, X. Martí, D. Hrabovsky, F. Sánchez, M. García-Cuenca, C. Ferrater, M. Varela, U. Lüders, J. Bobo, and J. Fontcuberta, "Electric-Field Control of Exchange Bias in Multiferroic Epitaxial Heterostructures," *Physical Review Letters*, vol. 97, no. 22, p. 227201, Nov. 2006.

[82] K. Roy, S. Bandyopadhyay, and J. Atulasimha, "Energy dissipation and switching delay in stress-induced switching of multiferroic nanomagnets in the presence of thermal fluctuations," *Journal of Applied Physics*, vol. 112, no. 2, 2012.

[83] S. a Wolf, D. D. Awschalom, R. a Buhrman, J. M. Daughton, S. von Molnár, M. L. Roukes, a Y. Chtchelkanova, and D. M. Treger, "Spintronics: a spin-based electronics vision for the future.," *Science (New York, N.Y.)*, vol. 294, no. 5546, pp. 1488–1495, 2001.

[84] G. Csaba, A. Imre, G. H. Bernstein, W. Porod, and V. Metlushko, "Nanocomputing by field-coupled nanomagnets," *IEEE Transactions on Nanotechnology*, vol. 1, no. 4, pp. 209–213, 2002.

[85] R. P. Cowburn, “Room Temperature Magnetic Quantum Cellular Automata,” *Science*, vol. 287, no. 5457, pp. 1466–1468, 2000.

[86] D. B. Carlton, N. C. Emley, E. Tuchfeld, and J. Bokor, “Simulation studies of nanomagnet-based logic architecture.,” *Nano letters*, vol. 8, no. 12, pp. 4173–8, Dec. 2008.

[87] S. Bandyopadhyay and M. Cahay, “Electron spin for classical information processing: a brief survey of spin-based logic devices, gates and circuits.,” *Nanotechnology*, vol. 20, no. 41, p. 412001, 2009.

[88] S. Salahuddin and S. Datta, “Interacting systems for self-correcting low power switching,” *Applied Physics Letters*, vol. 90, no. 9, pp. 1–4, 2007.

[89] A. Imre, G. Csaba, L. Ji, A. Orlov, G. H. Bernstein, and W. Porod, “Majority logic gate for magnetic quantum-dot cellular automata.,” *Science (New York, N.Y.)*, vol. 311, no. 5758, pp. 205–208, 2006.

[90] D. C. Ralph and M. D. Stiles, “Spin transfer torques,” *Journal of Magnetism and Magnetic Materials*, vol. 320, no. 7, pp. 1190–1216, 2008.

[91] M. S. Fashami, K. Roy, J. Atulasimha, and S. Bandyopadhyay, “Magnetization dynamics, Bennett clocking and associated energy dissipation in multiferroic logic.,” *Nanotechnology*, vol. 22, no. 15, p. 155201, 2011.

[92] Y.-H. Chu, L. W. Martin, M. B. Holcomb, M. Gajek, S.-J. Han, Q. He, N. Balke, C.-H. Yang, D. Lee, W. Hu, Q. Zhan, P.-L. Yang, A. Fraile-Rodríguez, A. Scholl, S. X. Wang, and R. Ramesh, “Electric-field control of local ferromagnetism using a magnetoelectric multiferroic.,” *Nature materials*, vol. 7, no. 6, pp. 478–482, 2008.

[93] T. Wu, A. Bur, K. Wong, J. Leon Hockel, C. J. Hsu, H. K. D. Kim, K. L. Wang, and G. P. Carman, “Electric-poling-induced magnetic anisotropy and electric-field-induced magnetization reorientation in magnetoelectric Ni/(011) [Pb(Mg 1/3Nb2/3)O3](1-x)-[PbTiO 3]x heterostructure,” *Journal of Applied Physics*, vol. 109, no. 7, pp. 1–4, 2011.

[94] N. D. Souza, M. Salehi, and S. Bandyopadhyay, “Strain Induced Clocking of Nanomagnets for Ultra Low Power Boolean Logic,” pp. 1–40.

[95] D. Bhowmik, L. You, and S. Salahuddin, “Spin Hall effect clocking of nanomagnetic logic without a magnetic field.,” *Nature nanotechnology*, vol. 9, no. 1, pp. 59–63, 2014.

[96] G. Yu, P. Upadhyaya, Y. Fan, J. G. Alzate, W. Jiang, K. L. Wong, S. Takei, S. a Bender, L.-T. Chang, Y. Jiang, M. Lang, J. Tang, Y. Wang, Y. Tserkovnyak, P. K. Amiri, and K. L. Wang, “Switching of perpendicular magnetization by spin-orbit torques in the absence of external magnetic fields.,” *Nature nanotechnology*, vol. 9, no. 7, pp. 548–54, 2014.

[97] R. P. Cowburn, "Superparamagnetism and the future of magnetic random access memory," *Journal of Applied Physics*, vol. 93, no. 11, pp. 9310–9315, 2003.

[98] M. S. Fashami, K. Munira, S. Bandyopadhyay, A. W. Ghosh, and J. Atulasimha, "Switching of dipole coupled multiferroic nanomagnets in the presence of thermal noise: Reliability of nanomagnetic logic," *IEEE Transactions on Nanotechnology*, vol. 12, no. 6, pp. 1206–1212, 2013.

[99] M. Salehi Fashami, J. Atulasimha, and S. Bandyopadhyay, "Energy dissipation and error probability in fault-tolerant binary switching.," *Scientific reports*, vol. 3, p. 3204, 2013.

[100] I. D. Mayergoyz, G. Bertotti, and C. Serpico, *Nonlinear magnetization dynamics in nanosystems*. Elsevier, 2009.

[101] R. P. Cowburn, D. K. Koltsov, a. O. Adeyeye, and M. E. Welland, "Single-Domain Circular Nanomagnets," *Physical Review Letters*, vol. 83, no. 5, pp. 1042–1045, 1999.

[102] G. Brown, M. a. Novotny, and P. A. Rikvold, "Langevin Simulation of Thermally Activated Magnetization Reversal in Nanoscale Pillars," vol. 64, p. 19, 2001.

[103] D. E. Nikonov, G. I. Bourianoff, G. Rowlands, and I. N. Krivorotov, "Strategies and tolerances of spin transfer torque switching," *Journal of Applied Physics*, vol. 107, no. 11, 2010.

[104] D. X. Chen, J. a. Brug, and R. B. Goldfarb, "Demagnetizing factors for cylinders," *IEEE Transactions on Magnetics*, vol. 27, no. 4, pp. 3601–3619, 1991.

[105] A. K. Biswas, S. Bandyopadhyay, and J. Atulasimha, "Acoustically assisted spin-transfer-torque switching of nanomagnets: An energy-efficient hybrid writing scheme for non-volatile memory," *Applied Physics Letters*, vol. 103, no. 23, 2013.

[106] A. K. Biswas, S. Bandyopadhyay, and J. Atulasimha, "Complete magnetization reversal in a magnetostrictive nanomagnet with voltage-generated stress : A reliable energy-efficient non-volatile magneto-elastic memory," vol. 072408, no. 2014, 2014.

[107] R. Cowburn, "Probing antiferromagnetic coupling between nanomagnets," *Physical Review B*, vol. 65, no. 9, p. 092409, Feb. 2002.

[108] J. Nogués and I. K. Schuller, "Exchange bias," *Journal of Magnetism and Magnetic Materials*, vol. 192, no. 2, pp. 203–232, Feb. 1999.

[109] J. Nogués, J. Sort, V. Langlais, V. Skumryev, S. Suriñach, J. S. Muñoz, and M. D. Baró, "Exchange bias in nanostructures," *Physics Reports*, vol. 422, no. 3, pp. 65–117, Dec. 2005.

[110] S. Guo, W. Liu, H. Meng, X. H. Liu, W. J. Gong, Z. Han, and Z. D. Zhang, "Exchange bias and its training effect in Ni/NiO nanocomposites," *Journal of Alloys and Compounds*, vol. 497, no. 1–2, pp. 10–13, May 2010.

[111] a. Mumtaz, K. Maaz, B. Janjua, S. K. Hasanain, and M. F. Bertino, "Exchange bias and vertical shift in CoFe2O4 nanoparticles," *Journal of Magnetism and Magnetic Materials*, vol. 313, no. 2, pp. 266–272, Jun. 2007.

[112] D. Y. Qiu, K. Ashraf, and S. Salahuddin, "Nature of magnetic domains in an exchange coupled BiFeO3/CoFe heterostructure," *Applied Physics Letters*, vol. 102, no. 11, p. 112902, 2013.

[113] J. Saha and R. Victora, "Spontaneous exchange bias: Unidirectional anisotropy in an otherwise isotropic system," *Physical Review B*, vol. 76, no. 10, p. 100405, Sep. 2007.

[114] T. Maity, S. Goswami, D. Bhattacharya, and S. Roy, "Superspin Glass Mediated Giant Spontaneous Exchange Bias in a Nanocomposite of BiFeO3-Bi2Fe," *Physical Review Letters*, vol. 110, no. 10, p. 107201, Mar. 2013.

[115] N. N. Phuoc and C. K. Ong, "Strain-driven fractional spontaneous exchange bias in ferromagnetic/antiferromagnetic thin films with composition-graded ferromagnetic layer," *Journal of Applied Physics*, vol. 115, p. 143901, 2014.

[116] M. Thakur, M. Patra, S. Majumdar, and S. Giri, "Influence of cooling field on the magnetic properties of Ni/NiO nanostructure," *Journal of Alloys and Compounds*, vol. 480, no. 2, pp. 193–197, Jul. 2009.

[117] M. Fraune, U. Rüdiger, G. Güntherodt, S. Cardoso, and P. Freitas, "Size dependence of the exchange bias field in NiO/Ni nanostructures," *Applied Physics Letters*, vol. 77, no. 23, p. 3815, 2000.

[118] J. B. Yi, J. Ding, Z. L. Zhao, and B. H. Liu, "High coercivity and exchange coupling of Ni/NiO nanocomposite film," *Journal of Applied Physics*, vol. 97, no. 10, p. 10K306, 2005.

[119] A. Agrawal, H. R. Habibi, R. K. Agrawal, J. P. Cronin, D. M. Roberts, R. Caron-Popowich, and C. M. Lampert, "Effect of deposition pressure on the microstructure and electrochromic properties of electron-beam-evaporated nickel oxide films," *Thin Solid Films*, vol. 221, no. 1–2, pp. 239–253, Dec. 1992.